PRECIPITATION OF RADIATION BELT ELECTRONS BY OBLIQUELY-PROPAGATING LIGHTNING-GENERATED WHISTLER WAVES

A DISSERTATION
SUBMITTED TO THE DEPARTMENT OF ELECTRICAL ENGINEERING
AND THE COMMITTEE ON GRADUATE STUDIES
OF STANFORD UNIVERSITY
IN PARTIAL FULFILLMENT OF THE REQUIREMENTS
FOR THE DEGREE OF
DOCTOR OF PHILOSOPHY

By
David Scott Lauben
October 1998

I certify that I have read this dissertation and that in my opinion it is fully adequate, in scope and in quality, as a dissertation for the degree of Doctor of Philosophy.

Umran S. Inan
(Principal Advisor)

I certify that I have read this dissertation and that in my opinion it is fully adequate, in scope and in quality, as a dissertation for the degree of Doctor of Philosophy.

Timothy F. Bell

I certify that I have read this dissertation and that in my opinion it is fully adequate, in scope and in quality, as a dissertation for the degree of Doctor of Philosophy.

Brad G. Osgood

Approved for the University Committee on Graduate Studies:

Dedication

This thesis is dedicated to my Lord and Savior Jesus Christ,
by whom and for whom all things have been created,
including this present author.

Acknowledgements

I would foremost like to express my deep and sincere gratitude and appreciation to my principal advisor, Prof. Umran S. Inan, whose dedication to both his field and to his students is unsurpassed. He has gone far beyond the call of duty in providing support and encouragement to me, especially at critical junctures, and his patience and flexibility have been nothing short of remarkable in taming, at least in part, this horse who refused to be broken.

I would also like to thank my second advisor Timothy Bell, whose wealth of knowledge, insight and quickness to grasp the central issue of seemingly any problem provided me with the needed assurance at key stages during the formulation phase. So much of what is contained within these pages is an extension of his own ideas, presented over the years in his many excellent papers.

I would like to thank my third reader, Prof. Brad Osgood, for his immediate helpfulness and quick turnaround in reviewing the manuscript. Thank you Brad!

I would also like to thank Prof. Bob Helliwell for his contagious excitement, inspiring comments, and enthusiastic presentation of his "Waves in the Magnetosphere" course (I trust he will enjoy reading Chapter 2), and Prof. Martin Walt for his helpful questions and comments at various stages during the thesis development (much of Chapter 3 is written with him in mind), and his sensible and equally stimulating course on "Geomagnetically Trapped Radiation." I would also like to express my respect and admiration for Prof. Ron Bracewell, who beyond his excellent classes in Fourier Transforms, Antenna Theory, and "Introduction to Starlab," was the first to make me feel truly welcome at Stanford.

My personal thanks go to my friend and associate Scott Williams, who has helped in ways that only a few may ever know, and to Victor Aguero, whose regular reminders of what's "really important" have helped me to maintain perspective throughout this often difficult process.

I would like to thank my parents, Robert and Carolyn Lauben, for bringing me into this world, training me in the way I should go, and then actually "letting me go" to pursue my path through life. Their dedication and sacrifice on my behalf I cannot repay. May this son bring them joy, and may they not be ashamed when they contend with their enemies in the gate.

I would also like to thank Pastor Bob Feldman for confirming to me the life and freedom we have available by faith in the righteousness revealed by God in Christ Jesus, and Pastor Rich Carlson, whose own life has demonstrated and taught me the value of bearing up under the very $\theta\lambda\iota\psi\iota\zeta$ which produces in us a glory far beyond all comparison.

This page would not be complete without my deepest thankfulness towards and fondest memories of my friend and sister in Christ, Deborah Margaret Wohlfort, whose encouragement both in the Lord and in pursuing excellence in education has propelled me to where I am today. Debbie, may your joy in the presence of your Master be full indeed!

This research was supported by the National Aeronautics and Space Administration, under grants NAGW-5156 at Stanford and NAS5-30371 via subcontract from the University of Iowa.

This page intentionally left blank.

Abstract

This dissertation presents a formulation for calculating the transient precipitation of energetic radiation belt electrons which results from gyroresonance scattering induced by obliquely-propagating whistler-mode waves throughout broad regions of the magnetosphere, with application to VLF whistlers generated by individual atmospheric lightning discharges. The formulation is applied for representative lightning locations as a means to assess the loss of energetic electrons from the Earth's magnetosphere and associated energy deposition to the upper atmosphere which occurs in response to global lightning activity.

The method utilizes a comprehensive raytracing technique to first determine the spatially varying oblique whistler wave properties (wave normal angle, power density and propagation delay) throughout the magnetosphere over the broadband frequency range f=200 Hz to 10 kHz, for a set of assumed lightning source geomagnetic latitudes λ_s=20°, 30°, 40° and 50°, and subsequently employs a test particle formulation to calculate the energy-time signatures of the precipitating energetic (E=1 keV to 3 MeV) electron flux at ionospheric altitudes over L-shells ranging 1.8 to 4.0. These signatures are then extrapolated over longitude and interpolated over latitude to develop the full temporal and spatial precipitation footprints or "hotspots" which form over extensive geographic regions, subject to a selectable minimum precipitation energy threshold ($E > E_{\mathrm{th}}$), in order to explore the variation in hotspot location, size and duration as a function of particle energy range.

Results indicate a universal poleward displacement of the peak precipitation flux by $\sim 15°$ with respect to the latitude of the causative lightning source, owing to the general tendency of the oblique waves to propagate across magnetic field lines (initially from lower to higher L-shells) so that the most intense whistler waves which originate directly above the lightning discharge subsequently arrive near the magnetic equator (where the strongest scattering takes place) at L-shells which are higher than the L-shell passing through the source. It is also shown that the cross-L wave propagation paths give rise to systematic variations in the detailed precipitation energy-time signatures for different L-shells, depending on whether the maximum wave intensities are encountered relatively early or late along a given particle trajectory.

The overall precipitation hotspots appear at geographic latitudes initially as low as $\sim 25°$ (for projections over the Eastern United States) and as early as 50 ms after the lightning discharge, moving rapidly poleward to latitudes approaching $\sim$50° and higher over the course of $\sim$3 s. Detailed spatial flux contours are given at prescribed time increments for selected precipitation energy ranges $E > 0$, $E > 1$ keV and $E > 1$ MeV. In general, for particles over all energies ($E > 0$), the size of the e.g. 3 dB precipitation flux contour covers roughly $\sim 5°$ in latitude and initially $\sim 10°$ in longitude, while subsequently expanding in width to more than 30° longitude during the course of its poleward motion, such that the time-integrated precipitation (fluence) pattern typically forms a broad "V"-shape over the precipitation region. In constrast, the precipitation hotspots formed by

the highest energy particles ($E > 100$ keV, and especially $E > 1$ MeV) are more localized, having diameter $\leq\sim 6^\circ$ and remaining nearly stationary over time, and furthermore are shown to more or less systematically track the location of the lightning source.

As a quantitative example, for a representative strong lightning discharge giving peak electric field $E_{100} = 10$ V/m (at distance $R = 100$ km) located at $\sim 28^\circ$ geographic latitude (e.g. near the tip of Florida), the maximum induced precipitation occurs for $L \sim 2.8$, consisting of electrons at $E > 10$ keV carrying an energy flux $Q > 1$ milli-erg/cm^2/s lasting $\sim 3/4$ s (with peak $Q_{\rm pk} > 10$ milli-ergs/cm^2/s, comparable to weak auroral fluxes) deposited over a spatial region $\sim 5^\circ \times 10^\circ$ (latitude $\times$ longitude) in size, centered near $\sim 43^\circ$ (just south of the great lakes). By extension, since the precipitation flux is linear in E_{100}, an extremely strong discharge with e.g. $E_{100} = 100$ V/m would lead to a peak energy flux $Q > 100$ milli-ergs/cm^2/s having similar temporal and spatial characteristics.

Results are summarized in the form of longitude-integrated profiles giving precipitation energy flux vs. latitude and precipitated electron number flux vs. L-shell, both of which show a strong bias in effect towards higher latitudes and L-shells respectively, suggesting that precipitation induced by lightning-generated whistlers on a global-scale is a significant, previously overlooked energetic electron loss mechanism, particularly over the range $2.5 \leq L \leq 4$, furthermore leading to significant energy deposition at higher latitudes. This dissertation concludes with a brief discussion regarding related theoretical and experimental results, giving suggestions both for experimental validation and for future theoretical research.

Contents

List of Tables

List of Figures

Chapter 1

Introduction

"It is the glory of God to conceal a matter; to search out a matter is the glory of kings. [Prov 25:2]"

1.1 Scientific Background

Earth's Radiation Belts. Since the discovery of the Earth's radiation belts [*Van Allen*, 1959] much progress has been made in understanding the source and loss processes which control the fluxes of these highly energetic (100 eV to >100 MeV) particles (for an excellent overview the reader is referred to the recent articles by *Walt* [1997] and *McIlwain* [1997]). Regarding the present study, fresh populations of energetic electrons (and ions) ejected from the Sun and carried along in the form of the solar wind are regularly injected at the outer-most boundary of the Earth's magnetosphere [*Li et al.*, 1997; *Baker et al.*, 1997], becoming trapped in the magnetic mirror formed by the Earth's nominally dipolar field [*Walt*, 1994]. Under the action of a variety of drift and acceleration mechanisms these particles subsequently disperse in longitude around and diffuse radially inward towards the Earth to form the dynamic radiation belt structure [*Imhof and Reagan*, 1973; *Lyons and Williams*, 1975a; *Lyons and Williams*, 1975b; *Spjeldvik*, 1976]. Such fluxes can not build up indefinitely, and early attempts to understand the balance of mechanisms governing the equilibrium densities – particularly loss mechanisms – considered first the effect of Coulomb collisions with atmospheric constituents, both for those particles arriving at the Earth's upper atmosphere at the limit of their inward radial travel, and for those particles skimming the atmosphere during each reflection at the low altitude magnetic mirror points. It was quickly recognized, however, that such collisions alone could not account for the observed loss rates throughout most of the magnetosphere – clearly some additional mechanism was at work. In addition, detailed satellite surveys revealed that during sustained periods of relatively quiet magnetospheric conditions (and diminished particle injections), there appeared regularly over the course of only a few days, a density depletion or "slot" region at equatorial distances of several Earth radii, which would persist until the next injection event [*Lyons and Kennel*, 1972].

Wave/Particle Loss Mechanisms. These and other observations led *Dungey* [1963], *Cornwall* [1964] and others to suggest that a special form of discrete, coherent very-low-frequency (VLF) wave energy termed a *whistler*, arising regularly as the natural response of the magnetosphere to terrestrial lightning, would be particularly effective at scattering energetic electrons, possibly accounting for the high loss rates, especially given the continual lightning activity occurring on a global scale. Soon thereafter, *Kennel and Petschek* [1966], and successors [*Lyons and Thorne*, 1973] and others proposed an alternate mechanism wherein a form of turbulent incoherent wave energy termed *hiss* also would, through many successive random-walk particle scatterings, lead to enhanced diffusion and high loss rates, especially noting that hiss regularly occurs following disturbed magnetospheric conditions. (For a review of different types of radio wave energy commonly observed in planetary magnetospheres, see e.g.*Kurth and Gurnett* [1991].) As it turns out, both the coherent and incoherent mechanisms appeal to the general condition for wave/particle gyroresonance [*Brice*, 1964; *Dysthe*, 1971], and as such they share common properties, even while differing markedly in their development and application.

Lightning-Induced Electron Precipitation. In 1984, *Voss et al.* documented multiple one-to-one associations of strong ($\sim$100$\times$ background) transient ($\sim$1 s) enhancements in the precipitating energetic electron flux with individual lightning-generated whistlers, thus establishing *Lightning-Induced Electron Precipitation* (LEP) as being both detectable and appreciable. For instance, estimates based on these observations indicated that a single LEP burst could empty $\sim$0.001% of the radiation belt energetic electron population along the affected field line, depositing an energy fluence of $\sim 10^{-3}$ ergs/cm^2 to the upper atmosphere, in turn leading to at least one form of the so-called "Trimpi" effect seen frequently on manmade subionospheric VLF/LF signals [*Carpenter et al.*, 1984; *Inan et al.*, 1985; *Inan and Carpenter*, 1986; *Burgess and Inan*, 1993].

For further reference, the significance of wave/particle interactions in determining the loss rates for radiation-belt energetic electron population, and in particular burst precipitation events such as LEP's, has been discussed in detail by *Imhof et al.* [1983, 1986, 1989], *Chang and Inan* [1985], *Burgess and Inan* [1993], *Walt et al.* [1996], *Imhof et al.* [1997] and others, while the relative role played by short-duration coherent wave packets vs. sustained incoherent wave activity (e.g. VLF/ELF hiss) has been addressed by *Inan et al.* [1982], *Inan* [1987] and recently by *Abel and Thorne* [1998a]. Regarding the effects of electron precipitation bursts on the upper atmosphere and on subionospheric ELF/VLF waves, the reader is referred to *Inan et al.* [1985, 1988], *Carpenter and Inan* [1987], *Inan et al.* [1990], and references therein.

LEP Modeling Efforts. Efforts to model burst precitation events induced by discrete VLF wave pulses continued with *Inan et al.* [1978], *Chang et al.* [1983] and *Inan et al.* [1985], culminating with *Inan et al.* [1989] which calculated detailed energy-time precipitation spectra to match a single event taken from *Voss et al.* [1984]. In that case, by virtue of the whistler signal detected on the ground,

the responsible whistler wave energy was known to have propagated in the so-called *ducted* mode, parallel to the particular magnetic field line during its traverse through the magnetosphere, guided by occasionally-occuring, yet nonetheless enduring field-aligned density structures in the thermal plasma so as to exit the magnetosphere the in the hemisphere conjugate to that of the causative lightning discharge [*Helliwell*, 1965; *Carpenter et al.*, 1971]. While these efforts were successful, the inherent restriction to the particular case of ducted waves precludes treatment of the far greater portion of whistler wave energy entering vast volumes of the magnetosphere and propagating in the *oblique* mode, i.e. at non-zero wave normal and ray path angles with respect to the Earth's field lines. Hence the question of the total impact of all lightning-generated whistlers on the energetic particle populations remains open.

As the next logical step, this dissertation presents a newly-developed formulation to calculate the electron precipitation induced over an entire hemisphere by obliquely-propagating whistler waves generated by a given lightning discharge of specified strength and location. The resulting scattering and precipitation fluxes, when considered together with global lightning statistics, serve to assess the contribution of all lightning-generated whistlers to both the loss of energetic particles from the magnetosphere and the associated energy deposition to the upper atmosphere. These results presented herein suggest that lightning-generated oblique whistler induced precipitation is an important, previously overlooked mechanism regarding the loss of energetic radiation-belt electrons from the magnetosphere and the deposition of energy to the upper atmosphere.

1.2 Oblique-Whistler Precipitation

Figure 1.1 illustrates the basic Lightning-Induced Electron Precipitation event sequence and will aid the discussion of the major components of the model:

1. The discharge current from a lightning flash radiates impulsive electromagnetic wave energy in all directions,

2. This impulsive wave energy spreads throughout the earth-ionosphere waveguide while a portion couples into and propagates obliquely throughout the magnetosphere, suffering frequency-dependent spatial refraction and temporal dispersion to form the characteristic oblique whistler,

3. As this whistler travels throughout the magnetosphere, a fraction of otherwise trapped energetic electrons matching the doppler-shifted gyroresonance condition and having pitch-angles initially near the edge of the magnetic-mirror loss-cone (defined in the next section) are scattered into the loss-cone,

4. The lowered mirror height of those particles now in the loss-cone allows them to be precipitated into the relatively dense upper atmosphere.

As a result of the ubiquitous propagation of the oblique whistler throughout the magnetosphere, scattering will occur over a range of field lines leading to precipitation at ionospheric altitudes over a range of latitudes, in general northward and southward of the lightning source latitude, *and* over a range of longitudes to either side of the longitudinal meridian which contains the source. Thus, each lightning discharge leads to an associated transient precipitation event depositing flux over an extensive ionospheric region. Note from Fig. 1.1 in particular that the field line is illuminated by ray paths originating over a *range* of input latitudes above the lightning discharge; this aspect of the oblique-whistler case demands special attention throughout the formulation.

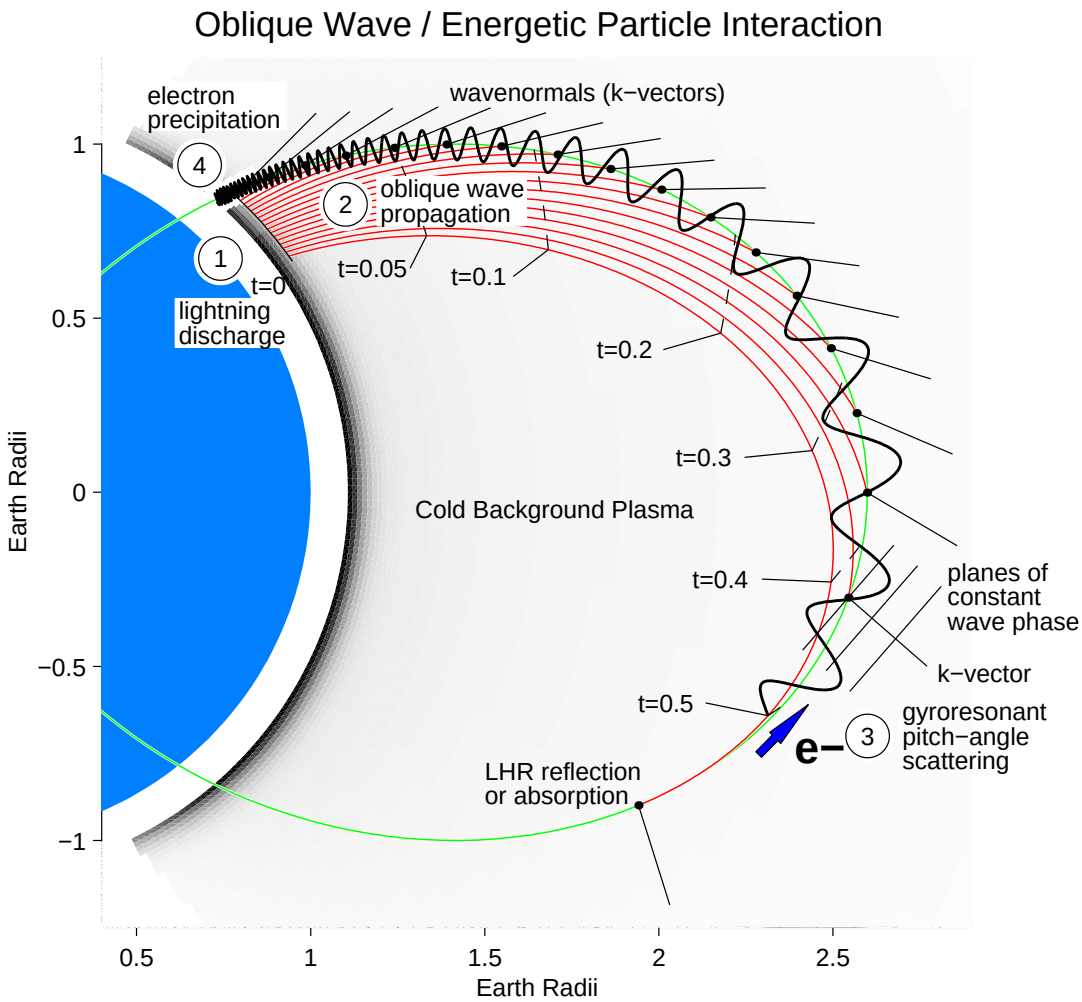

Figure 1.1: Lightning-induced electron precipitation (LEP) from oblique wave/energetic particle scattering along a particular magnetic field line. The lightning discharge leads to oblique mode propagation throughout the magnetosphere, so that particles along field lines both inside and beyond the field line shown are also affected. The event sequence 1-4 is discussed in the text.

1.3 Formulation Overview

Context and Motivation. It is desired to calculate the transient electron precipitation over the affected ionospheric region induced by an individual lightning discharge, assuming oblique whistler-mode propagation throughout the magnetosphere. To this end, the previous formulation of *Chang and Inan* [1985] which gives the precipitation at the foot of a single field line for parallel wave propagation (along the same field line) serves as the basic starting point. In extending this formulation, the oblique nature of the waves presents further challenge in two areas:

1. The first area regards the interaction between a test particle and a-priori specified *transient*, *oblique* wave fields at any point along a given electron trajectory. The basic equations of motion for oblique-mode gyroresonance (given below) were developed by *Bell* [1984] and implemented by *Jasna et al.* [1992] and *Jasna et al.* [1998], the later which treats the single pass interaction of an ensemble of energetic electrons through fixed-frequency steady-state oblique-mode wave fields. Here this treatement must be extended to the case of *transient* oblique waves in the manner of *Chang and Inan* [1985].

2. The second area regards the specification of these transient oblique wave fields over all time and at all points along the electron trajectories of interest. As no closed-form expression for the needed oblique-whistler wave properties (wave normal angle, wave power density and propagation delay) exists, a comprehensive VLF raytracing methodology motivated by new *in-situ* measurements of actual oblique whistlers is developed to establish these wave properties.

To summarize, the task at hand is to first specify the oblique whistler wave fields throughout the magnetosphere for a given lightning discharge, and then employ the newly generalized formulation, which must track the propagating oblique whistler wave fields seen by each counterstreaming test-particle as the interaction proceeds, to calculate the scattering induced over a wide range of particle energies, over a range of field lines and over a range of longitudes, to develop the resulting energetic electron precipitation footprint or "hotspot" at ionospheric altitudes.

Fundamental Formulation. The general relativistic equation of motion for a test particle with rest mass m and charge q in the combined Earth dipole $\mathbf{B_o}$ and oblique whistler-wave electromagnetic $\mathbf{E^w}, \mathbf{B^w}$ fields may be written

$$\ddot{\mathbf{r}} = \frac{q}{m\gamma}\left[\mathbf{E^w} + \dot{\mathbf{r}} \times (\mathbf{B_o} + \mathbf{B^w})\right] \qquad [1.1]$$

where $\gamma = 1/\sqrt{1 - v^2/c^2}$ for total particle velocity $v = |\dot{\mathbf{r}}|$, for $\mathbf{r}$ measured in the rest frame. In the absence of the wave fields ($\mathbf{E^w}$,$\mathbf{B^w}$=0) this equation specifies classic adiabatic magnetic mirroring for which the path traced by a particle consists of cyclotron motion about the static field line $\mathbf{B_o}$ plus linear translation along $\mathbf{B_o}$, which when superposed forms a helix conforming to the

field line as depicted in Fig. 1.2a. Such helix has local gyroradius $\rho = m\gamma v_\perp/qB$ and pitch angle $\alpha = \tan^{-1} v_\perp/v_\parallel$, where $v_\perp$ and $v_\parallel$ are the particle velocities transverse and parallel to $\mathbf{B_o}$, both of which vary with local field strength $B(\lambda) = |\mathbf{B_o}|$ according to [*Walt*, 1994]

$$v_\parallel = v\,\cos\alpha(\lambda), \quad v_\perp = v\,\sin\alpha(\lambda), \quad \sin^2\alpha(\lambda) = \frac{B(\lambda)}{B_{\rm eq}}\sin^2\alpha_{\rm eq} \qquad [1.2]$$

where $B_{\rm eq}$ and $\alpha_{\rm eq}$ denote equatorial values. For a given value of $\alpha_{\rm eq}$, mirroring occurs at that λ_m for which $\alpha(\lambda_m) \to 90°$ defined implicitly by $B(\lambda_m) = B_{\rm eq}/\sin^2\alpha_{\rm eq}$. The dipole geometry and field strength for a given field line are given respectively by

$$R(L,\lambda) = L\cos^2\lambda, \qquad B(L,\lambda) = B_\oplus\frac{1}{L^3}\frac{\sqrt{1+3\sin^2\lambda}}{\cos^6\lambda} \qquad [1.3]$$

where R is the radius to points at latitude λ along the field line, L is a convenient index equal to geocentric distance at which the field line intersects the magnetic equator (R and L in Earth radii), and $B_\oplus$ is the equatorial field strength at the Earth's surface, taken as $B_\oplus = 3.12\times10^{-5}$ T. Then given some effective ionopheric height h_p (e.g. in km) above which particles are assumed free to mirror but below which they are considered lost due to atmospheric collisions (that is, precipitated) the corresponding *equatorial loss-cone* pitch angle at the magnetic equator $\alpha^{\rm lc}_{\rm eq}$ is [*Inan*, 1977]

$$\sin\alpha^{lc}_{\rm eq} \quad = \quad (\epsilon_m^3/\sqrt{1+3(1-\epsilon_m)})^{1/2} \qquad [1.4]$$

where $\epsilon_m = (1/L)\ (R_e + h_m)/(R_e)$ and $Re = 6370$ km. Thus in this basic model, the quiescent equatorial energetic particle distribution is assumed non-zero for $\alpha_{\rm eq} \geq \alpha^{\rm lc}_{\rm eq}$ but void for $\alpha_{\rm eq} < \alpha^{\rm lc}_{\rm eq}$, whereupon the presence of the whistler wave fields causes a fraction of the electrons to be scattered to (equatorial) pitch angles $\alpha_{\rm eq} < \alpha^{\rm lc}_{\rm eq}$, giving rise to precipitation. As an example, for $L = 2$ and $h_p = 100$ km, the equatorial loss-cone pitch angle is $\alpha^{\rm lc}_{\rm eq} \sim 16.8°$, and for a particle initially at this pitch angle and subsequently scattered by $\sim 0.2°$ into the loss-cone, the mirror altitude is reduced to $h'_p = 60$ km, well within the relatively dense upper atmosphere.

Gyroaveraged Equations of Motion. To perform the scattering calculation at each point C=(L,λ) along the field line, a local cartesian coordinate system with $\hat{\mathbf{z}}\,||\,\mathbf{B_o}$ and $\hat{\mathbf{x}}$ pointing towards higher L is afixed which provides a local reference frame for the wave field components and electron helix as shown in Figs. 1.2a and b. Since the whistler wave mode under conderation is itself elliptically polarized it is natural to express the equations of motion using circular coordinates. Accordingly *Bell* [1984] gives the gyroperiod-averaged equations of motion in terms of the particle velocity $v_\parallel$, $v_\perp$ parallel and perpendicular to $\hat{\mathbf{z}}$ and the *average* phase angle η between the particle velocity vector, at Larmor phase φ, and the suitably decomposed right-hand circularly polarized component $\mathbf{B^w_R} = 1/2\,(B^w_x + B^w_y)$ of the wave total magnetic field vector $\mathbf{B^w}$, itself at generalized

wave phase $\Phi = \int \omega dt - \int \mathbf{k}\cdot\mathbf{dr}$ (c.f. [*Bell*, 1984; *Jasna et al.*, 1993] and Figs. 1.2b,c)

$$\dot{v}_{\parallel} = \frac{\omega_\tau^2}{m\gamma}\, k_z^{-1}\, \sin\eta - \frac{v_\perp^2}{2\omega_h}\frac{\partial\omega_h}{\partial z} \qquad [1.5]$$

$$\dot{v}_{\perp} = -\left[\omega_1(v_z{+}R_1)J_0(\beta) - \omega_2(v_z{-}R_2)J_2(\beta)\right]\, \sin\eta + \frac{v_z v_\perp}{2\omega_h}\frac{\partial\omega_h}{\partial z} \qquad [1.6]$$

$$\dot{\eta} = \frac{\omega_h}{\gamma} - \omega - k_z\, v_z \qquad [1.7]$$

where ω is the instananeous whistler wave frequency, $\omega_h/\gamma = qB^o/m\gamma$ is the local relativistic gyrogrequency of the energetic electron, and where

$$\begin{aligned}
\beta &= k_x v_\perp/\omega_h \\
k_z &= k\cos\theta_k = \frac{\omega}{c}\, n(\theta_k)\, \cos\theta_k, \quad k_x = k\sin\theta_k \\
\omega_\tau^2 &= \omega_{\tau o}^2\left[J_0(\beta) - \alpha_1 J_2(\beta) + \gamma\,\alpha_2 J_1(\beta)\right] \\
\omega_{\tau o}^2 &= \omega_1 k_z v_\perp \\
\omega_{1,2} &= (q/2m_e)(B_x^w \pm B_y^w) \\
\alpha_1 &= \omega_1/\omega_2 \\
\alpha_2 &= qE_z^w/(m\gamma\omega_1 v_\perp) \\
R_{1,2} &= (E_x^w \pm E_y^w)/(B_x^w \pm B_y^w)
\end{aligned}$$

where $n(\theta_k)$ is the refractive index (Chapter 2), and $J_{0,1,2}$ are Bessel functions of the first kind.

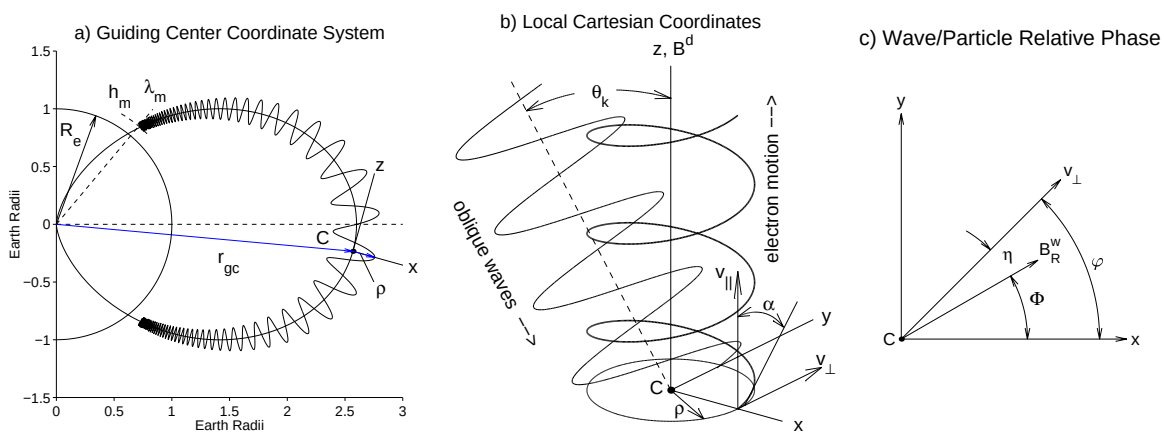

Figure 1.2: (a) Local cartesian coordinate system at each point $C{=}(L,\lambda)$ along the field line corresponding to guiding center $r_{\rm gc}$. (b) Energetic electron helix in local cartesian frame in which the elliptically polarized wave fields are applied. The wave normal angle θ_k lies in the x-z plane. (c) Gyroaveraged angle η between particle velocity vector (at Larmor phase φ) and the transverse right-hand circularly polarized wave magnetic field vector $\mathbf{B_R^w} = 1/2\,(B_x^w + B_y^w)$ at wave phase Φ.

Of particular importance is the projection of the wave **k**-vector parallel to $\mathbf{B_o}$ through wave normal angle θ_k (Fig. 1.2b) to give $k_z = \mathbf{k}\cos\theta_k$, and the participation of the two wave magnetic field components B_x^w, B_y^w and the full electric field vector $\mathbf{E^w}$ through $\omega_{1,2}$, α_2 and $R_{1,2}$, implicitly at all points C along the field line. Especially important is the value of k_z in the fundamental resonance condition found from setting equation [1.7] equal to zero (so that the time rate of change of the angle η is nominally zero, c.f. Fig. 1.2c)

$$\dot{\eta} = \omega_h/\gamma - w - k_z\, v_z = 0$$

When this condition is satisfied the Doppler-shifted frequency of the wave as seen by the energetic particle is matched to the particle's cyclotron frequency, so that the gyroaveraged electromagnetic wave fields appear temporarily stationary in the particle frame. When this match prevails for some appreciable distance (or equivalently, time), cumulative particle scattering can take place. Substituting $\gamma = (1 - v^2/c^2)^{-1/2}$ with $v^2 = v_z^2/\cos^2\alpha$ (where α is local particle pitch angle at any point along the field line) and solving the resulting quadratic equation for parallel velocity yields

$$v_{\rm res} \triangleq \frac{\pm\sqrt{\omega^2 k_z^2 + (\omega_h^2 - \omega^2)\left(k_z^2 + \frac{\omega_h^2}{c^2\cos^2\alpha}\right)} - \omega k_z}{k_z^2 + \frac{\omega_h^2}{c^2\cos^2\alpha}} \qquad [1.8]$$

where in general all quantities are understood to be functions of magnetic latitude λ along the particle L-shell to which the particle guiding center is bound. The value of $v_{\rm res}$ indicates the parallel velocity which a loss-cone particle must have in order to be in resonance with the wave. The $\pm$ sign on the radical indicates resonance for particles either approaching (+ root) or overtaking (− root) the wave; following previous formulations, the counter-streaming electrons (+ root), for which the resonant energies are generally lower thereby permitting more appreciable scattering for equivalent wave intensities, are treated herein. Note that equation [1.8] is parametric in the background static magnetic field strength through ω_h, instantaneous wave frequency ω and **k**-vector component k_z, and local particle pitch-angle α.

Resonant Energies. Curves giving resonant energy E_{res} for particles with v_z matching $v_{\rm res}$ and with pitch-angle at the edge of the loss-cone are shown vs. wave normal angle θ_k in Fig. 1.3, parametric in (constant) wave frequency f for three representative L-shells at $\lambda = 0$. These curves show that in general $E_{\rm res}$ is higher for lower L and increases with increasing θ_k, approaching 10 MeV(!) for $f < 1$ kHz at $L = 2$, and dropping to $E_{\rm res} < 1$ keV for $f > 5$ kHz at $L = 4$. Thus oblique waves will lead to the precipitation of particles having higher energies than will waves having $\theta_k = 0$ (i.e. ducted). Note that at each L, for some values of f as θ_k takes on higher values, (approaching the resonance cone angle θ_{res}), $E_{\rm res}$ plunges to suprathermal values; this regime has been studied in detail by *Jasna et al.* [1993]. Also note that for each L at a given fixed θ_k, $E_{\rm res}$ increases with

decreasing f; thus the specific Energy vs. time precipitation signatures will depend on the whistler f-t behavior seen by the counter-streaming particles.

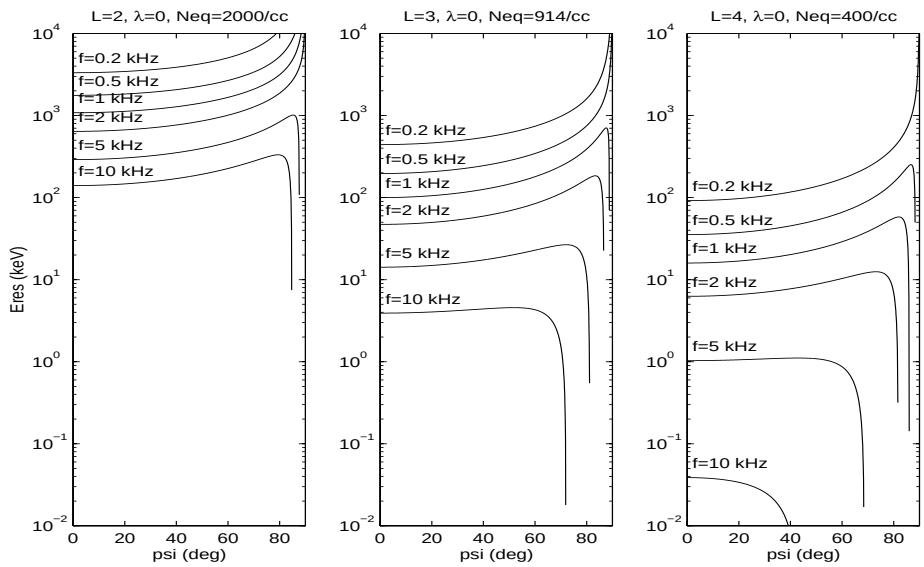

Figure 1.3: Loss-cone electron E_{res} vs. θ_k, parametric in fixed-frequency f for three L-shells at λ=0.

1.4 Thesis Organization

The remainder of this dissertation is organized as follows:

Chapter 2 presents the measurement and construction of the essential properties which define the obliquely-propagating lightning-generated whistler. The approach incorporates models for the source lightning discharge current, electromagnetic wave field radiation pattern, trans-ionospheric attenuation and magnetospheric propagation using a comprehensive raytracing methodology.

Chapter 3 presents the basic scattering and precipitation signatures induced by the oblique mode whistler waves calculated in Chapter 2 over the full-distribution of affected particles along selected L-shells. Simulated energy-time scattering and precipitation flux signatures as well as energy-integrated electron count and energy deposition rates are presented for several assumed lightning latitudes.

Chapter 4 builds on the results of Chapter 3 to calculate the geographic precipitation footprints at ionospheric altitudes. The resulting latitude-time signatures of the deposited energy flux takes the form of a dynamic "hotspot" moving rapidly from low to high latitudes over the course of several seconds following each lightning flash. Summary plots showing the variation of peak and time-integrated energy flux (fluence) with lightning source location are presented.

Chapter 5 summarizes the results of Chapters 2 through 4, compares and contrasts these results with those of related research, and concludes with comments regarding experimental validation and suggestions for future work.

1.5 Thesis Contributions

This dissertation covers the following contributions:

1. Measurement of in-situ magnetospheric whistlers showing a class whose wave normal angles exceed ∼50°, consistent with raytracing predictions,

2. Use of comprehensive raytracing methodology to construct the full-frequency oblique whistler wave properties throughout the magnetosphere,

3. General formulation to calculate the electron precipitation induced by highly-oblique, discrete, variable-frequency VLF waves throughout the magnetosphere,

4. Quantitative calculations of the transient electron number and energy precipitation fluxes resulting from typical individual strong lightning discharges over locations covering 20° to 50° magnetic latitude (∼10° to ∼40° geographic latitude for the eastern United States).

5. Identification of those L-shells and latitudes which are overall most strongly affected by lightning-generated oblique whistlers, seen to be largely independent of lightning location.

1.6 Preview of Typical Result

Fig. 1.4 previews a typical result. Here a lightning source at magnetic latitude λ_s=30° launches obliquely-propagating whistler waves having the spatial intensity pattern shown in Fig. 1.4a, with strong fields projecting to either side of $L=2.0$, depending on magnetic latitude. Fig. 1.4b shows the resulting precipitation energy flux signature at the foot of the L=2.2 field line, and Fig. 1.4c shows the resulting energy fluence deposited over a region half the size of the continental U.S, centered some ∼20° poleward of the lightning source.

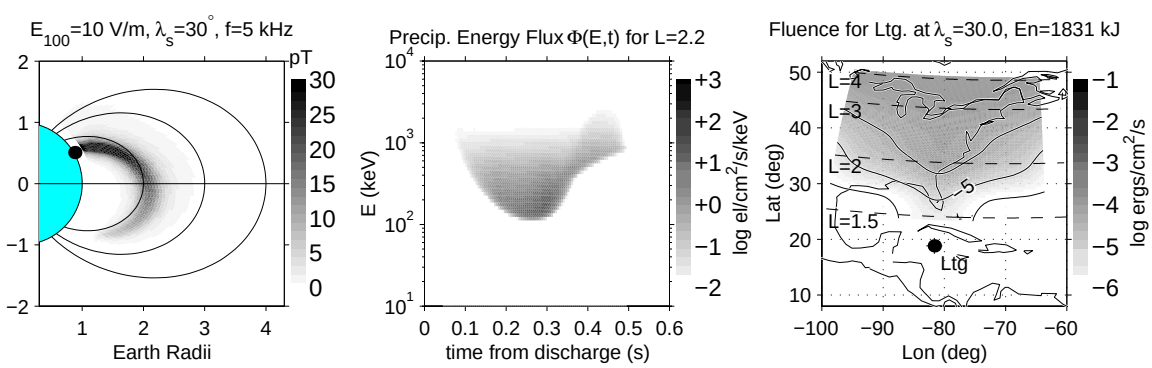

Figure 1.4: Example results taken from the forthcoming chapters. (a) Oblique whistler intensities projected throughout the magnetosphere from a lightning source at λ_s=30°. (b) Precipitation flux energy-time signature for L=2.2. (c) Fluence footprint projected over the Eastern United States.

Chapter 2

Oblique Whistlers

"What is the way to the place where the lightning is dispersed...? [Job 38:24]"

Section 1.3 of Chapter 1 indicated the importance of the wave normal angle θ_k which governs the particle resonance energy at any location through k_z $(= \mathbf{k}\cos\theta_k)$ in equation [1.8]. This chapter presents *in-situ* satellite measurement of whistler wave normal angle θ_k, intensity B_y^w and dispersion $t_g(f)$ at selected locations within the magnetosphere, and subsequently develops and employs a raytracing formulation to calculate the lightning-location-dependent oblique whistler wave fields throughout the magnetosphere which are needed to support the scattering calculations of Chapter 3.

2.1 Oblique Whistler *In-Situ* Measurement

This section reviews the theory and presents new measurements of obliquely-propagating whistlers.

2.1.1 Theory of VLF Waves in the Magnetosphere

Whistler E, B and θ_k. Following *Stix* [1962], for a magnetoplasma described by a suitably-defined anisotropic dielectric tensor $\overline{\mathbf{K}}$ for static field $\mathbf{B_o}$, the time-harmonic waves fields $\mathbf{E}$, $\mathbf{B}$ are given by the Maxwell equations

$$\begin{aligned} \nabla \times \mathbf{E} &= -j\omega\,\mathbf{B} \\ \nabla \times \mathbf{B} &= (j\omega/c^2)\,\overline{\mathbf{K}}\,\mathbf{E} \end{aligned}$$

the phasor solution of which leads to the electromagnetic field component ratios expressed in the coordinate system of in Fig. 1.2b in Section 1.3 (which takes $\hat{\mathbf{z}} \parallel \mathbf{B_o}$)

$$\frac{E_y}{E_x} = \frac{iD_s}{S_s - n^2},\ \frac{E_z}{E_x} = \frac{n_x n_z}{n_x^2 - P_s},\ \frac{B_x}{E_x} = \frac{-iD_s n_z}{c\,(S_s - n^2)},\ \frac{B_y}{E_x} = \frac{P_s n_z}{c\,(P_s - n_x^2)},\ \frac{B_z}{E_x} = \frac{iD_s n_x}{c\,(S_s - n^2)} \qquad [2.1]$$

with refractive index components n_x and n_z transverse and parallel to $\mathbf{B_o}$

$$n_x = n \sin\theta_k, \quad n_z = n \cos\theta_k, \qquad [2.2]$$

where, without loss of the generality, the angle θ_k of the **k**-vector (normal to planes of constant wave phase), measured with respect to $\mathbf{B_o}$, is taken to be in the x-z plane (Fig. 1.2b). The squared total refractive index is given by

$$n^2(\theta_k) = \frac{B \pm \sqrt{(R_s L_s - P_s S_s)^2 \sin^4\theta_k + 4\, P_s^2 D_s^2 \cos^2\theta_k}}{2A} \qquad [2.3]$$

with the sign on the radical chosen such that $n^2 > 0$, and with A and B given by

$$A = S_s + (P_s - S_s)\cos^2\theta_k, \quad B = P_s S_s + R_s L_s + (P_s S_s - R_s L_s)\cos^2\theta_k$$

where, for wave frequency $\omega = 2\pi f$ and for k thermal species of charge q_k, the Stix parameters are

$$S_s = (R_s + L_s)/2, \quad D_s = (R_s - L_s)/2,$$

$$R_s = 1 - \sum_k \frac{\omega_{pk}^2}{\omega^2}\left(\frac{\omega}{\omega + \omega_{hk}}\right), \quad L_s = 1 - \sum_k \frac{\omega_{pk}^2}{\omega^2}\left(\frac{\omega}{\omega - \omega_{hk}}\right), \quad P_s = 1 - \sum_k \frac{\omega_{pk}^2}{\omega^2}$$

where $\omega_{pk}^2 = N_k\, q_k^2/\epsilon_o\, m_k$, and $\omega_{hk} = q_k\, B^o/m_k$.

Reference field component. From the ratios in [2.1] the magnitude of the time-averaged Poynting flux $S^w = |\mathbf{S}^w|$, where $\mathbf{S}^w = (1/2)\ \mathrm{Re}\,\{\mathbf{E^w} \times \mathbf{B^w}/\mu\}$, may for convenience be related to the single reference component B_y^w via [*Bell*, 1984; *Jasna et al.*, 1993]

$$|B_y^w|^2 = \frac{2\mu_o}{c}\,|\mathbf{S}^w| X^2\, n\cos\theta_k \sqrt{(\tan\theta_k - \rho_1\rho_2)^2 + (1 + \rho_2^2\, X)^2} \qquad [2.4]$$

where $X = P_s/(P_s - n^2\sin^2\theta_k)$ and

$$\rho_1 = \frac{E_z^w}{E_y^w} = \frac{(n^2 - S_s)n^2 \sin\theta_k \cos\theta_k}{D_s\,(n^2\sin^2\theta_k - P_s)}, \qquad \rho_2 = \frac{E_x^w}{E_y^w} = \frac{n^2 - S_s}{D_s}$$

Wave normal and ray path. For obliquely propagating waves ($\theta_k \neq 0$) the path along which wave energy flows is in general *not* along $\mathbf{B_o}$ or **k** but at a some other angle denoted θ_r (the ray path angle) which, as it turns out, is everywhere normal to the refractive index surface $n(\theta_k)$ [*Helliwell*, 1965]. While general raytracing through inhomogeneous anisotropic media is a complex topic requiring careful attention to assumptions about the media [*Budden*, 1985], at present it is sufficient to note that the ray path through the magnetosphere is developed by applying Snell's law

to θ_k and n_x at each of a succession of small steps along the direction indicated by each respective value of ray path angle θ_r. Fig. 2.1a shows a typical ray path for a single frequency component of an otherwise broadband whistler which here enters the magnetosphere at magnetic latitude $\lambda_i \sim 50°$ and altitude $h_i = 1000$ km and subsequently arrives at the magnetic equator at $L = 2.6$. In general the ray will continue onward past this point; in Fig. 2.1 the ray is terminated at the equator for the purpose of comparison with measurements to follow. Fig. 2.1b shows the corresponding refractive index surface evaluated at this point (from [2.3]), with the wave normal θ_k and ray θ_r angles shown as indicated. Note the correspondence of both θ_k and θ_r in the two panels (i.e. "k" and "ray" labels), and the large value of $\theta_k \sim 60°$ at this location.

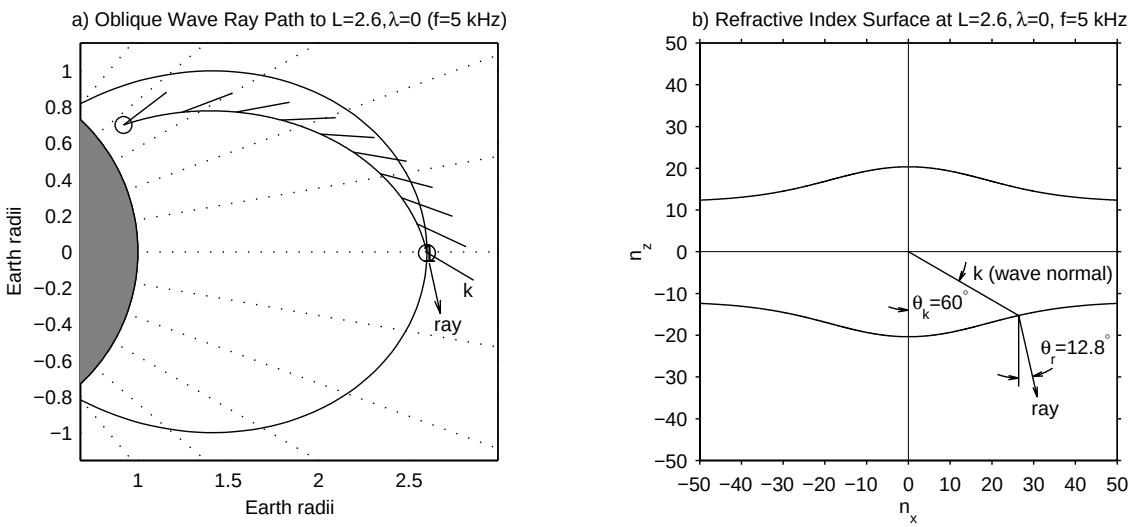

Figure 2.1: (a) Typical oblique ray path and (b) refractive index surface, both showing corresponding wave normal angles θ_k and ray path (energy flow) angle θ_r for the point at the magnetic equator.

2.1.2 Wave Normal Angle, Intensity and Dispersion

To confirm such large values for θ_k we analyze *in-situ* data obtained from the Plasma Wave Instrument (PWI) aboard the POLAR satellite. The PWI sensors include one spin-axis aligned (14 m) and two orthogonal spinning (100 m, 130 m) electric dipoles, and three orthogonal magnetic search-coils (70 μV/nT-Hz sensitivity) aboard the POLAR satellite (~18 hr period, ~2×9 R_e, ~90° inclination, North pole apogee orbit, 6 s cartwheel spin). The PWI electronics include a High-Frequency Waveform Receiver (HFWR) providing coincidently-sampled (14 μs sampling period) 6-component 0.45 s duration $\mathbf{E^w}$ and $\mathbf{B^w}$ wave field snapshots over the frequency range 0-26 kHz (spaced at 9.2 s intervals) [*Gurnett et al.*, 1995].

In the present application from the Maxwell equation $\nabla \cdot \mathbf{B} = 0$ it is evident that $\mathbf{k} \cdot \mathbf{B} = 0$, indicating that $\mathbf{k}$ is perpendicular to $\mathbf{B}$ at all times. This property motivates a number of analysis

techniques to determine $\mathbf{k}$ from two or more samples of $\mathbf{B^w}$ (and optionally, $\mathbf{E^w}$), most notably Mean's method [*Means*, 1972], which is applied here to the dynamic spectrum of $\mathbf{B^w}$ so as to resolve θ_k over both frequency and time.

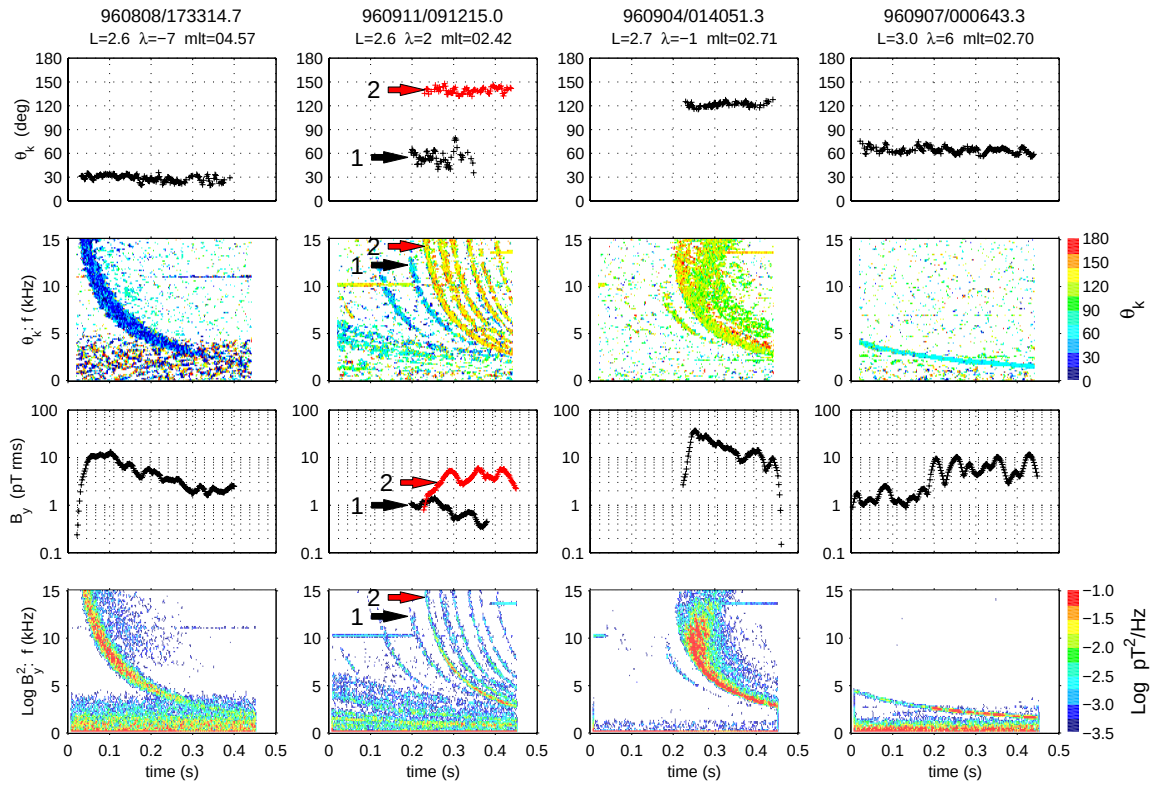

Figure 2.2: Oblique whistler intensity B_y^w and wave normal angle θ_k measurements.

Fig. 2.2 shows dynamic wave normal angle and wave intensity spectra for whistlers observed near the magnetic equator.[1] Considering first the wave intensities, the bottom row shows the log of the squared magnitude of the B_y^w component in dynamic f-t spectrogram format, while the row immediately above shows the intensity (in picoTeslas) for a ∼140 Hz bandwidth centered on the f-t trace. By virtue of the single-valued whistler f-t relationship for (i.e. for the lower branch, see [*Helliwell*, 1965]) this $B_y^w(t)$ is also $B_y^w(f)$; the significance of this point will become more clear in subsequent sections. Here the observed B_y^w intensities range ∼1 to 30 pT and exhibit a variety of $B_y^w(f)$ profiles. Then regarding wave normal angles, the row second from the top shows θ_k for each Δf-Δt cell associated with the intensity spectrograms,[2] while the top row shows corresponding $\theta_k(t)$ or equivalently $\theta_k(f)$ profiles along each whistler trace, measured with respect to the local static field $\mathbf{B_o}$ direction, where 0° indicates northward angles. Note that for comparison with theory the wave

[1] Near-equatorial measurements simplify interpretation by virtue of the symmetry of the magnetosphere– especially helpful when the latitude or even hemisphere of the lightning source is not immediately known, as in the present case.

[2] Only those Δf-Δt cells having well-defined reliable wave normals are shown in the color wave normal panels.

normal angle is taken as the most acute angle to either $\mathbf{B_o}$ or $-\mathbf{B_o}$ (i.e. the smaller of $\{\theta_k, 180-\theta_k\}$, c.f. Fig. 2.1). The snapshot for epoch 960911/091215.0 (second column) is of particular interest in that multiple whistlers are resolved into two distinct groups propagating in opposite directions with respect to $\mathbf{B_o}$; the "blue" group traveling south to north, and the "yellow" group north to south. In this case, one whistler from each cluster (arrows "1" and "2") has been selected for the respective $B_y^w(t)$ and $\theta(t)$ panels, both of which show very high wave normal angles on the order predicted by the raytracings. In particular, the whistler labeled "1" shows very high values in the range $\theta_k \sim 50-60°$. Note in addition the case for epoch 960904/014051.3 (third column), for which θ_k is also $\sim 60°$, while the intensity ranges $B_y^w \sim 10$ to 30 pT. These two cases in particular serve as archetypes for the oblique whistler simulations described in the next section.

2.2 Oblique Whistler Raytracing

2.2.1 General Raytracing Methodology

The required oblique whistler wave fields at any point are completely specified by the wave normal angle θ_k, wave power density S^w (giving B_y^w via [2.4]), and propagation delay or group time t_g (the variation of which gives the f-t dispersion). In general these parameters vary with frequency and location throughout the magnetosphere and as such may be written $\theta_k(f, L, \lambda)$, $S^w(f, L, \lambda)$ and $t_g(f, L, \lambda)$. As indicated in Section 1.3, in order to calculate the pitch angle scattering of the individual test particles, these quantities must be precisely specified along each L-shell of interest.

As no closed-form expression for these wave quantities exists, a comprehensive VLF raytracing methodology is developed based on the idea that since a whistler can be regarded as the impulse response of the magnetosphere to a broadband impulsive lightning discharge, the dispersing oblique whistler properties may thus be calculated in a manner analogous to Laplace transform inversion, whereby certain quantities evaluated over frequency for steady-state conditions are subsequently used to determine the corresponding impulse response. Here the actual procedure is complicated somewhat by the frequency-dependent refraction of the ray paths as the wave propagates in more than one spatial dimension as well as the f-t dispersion arising from the frequency-dependent propagation delay. As it turns out however, this generalized approach, while indeed requiring careful bookkeeping, nonetheless remains quite tractable.

As introduced in the previous section, raytracing is a common method used to determine the propagation paths and properties for fixed-frequency whistler-mode waves in the inhomogeneous magnetosphere, providing the wave normal angle θ_k and group time t_g along each ray path (c.f. Fig. 2.1a), while the wave power density S^w may be inferred from the ray path divergence and f-t dispersion. Using the Stanford raytracing program [*Inan and Bell*, 1977], the required wave properties over (f, L, λ) are determined by first tracing ensembles of ray paths for each f of a set of frequencies spanning the range 200 Hz to 10 KHz at a spacing of 200 Hz, noting the wave properties at

the ensuing ray/L-shell intersection points along each L-shell of interest, and subsequently combining these data in a manner which constructs, whether for a point which remains fixed in space or for the guiding-center trajectory of an electron moving along a specified L-shell, the effective f-t behavior and wave properties over all frequency. Note that in applying this technique, the magnetosphere is taken to be smoothly varying at all points such that the variation of the wave phase path integral $\Phi = \int \omega dt - \int \mathbf{k}\cdot\mathbf{r}$ with frequency, space and time is also everywhere smooth and continuous.

Raytracing model assumptions. The propagation of whistler-mode electromagnetic waves in the magnetosphere is largely determined by the static Earth magnetic field and cold plasma density gradients. Over the L-shells of interest (i.e $L <= 4$) the Earth field is relatively static and does not vary substantially on a day to day basis. Meanwhile for magnetospherically quiet (post-storm) night-time conditions considered herein the cold background plasma density is assumed to be in a state of diffusive equilibrium along any particular field line [*Angerami and Thomas*, 1964].

Fig. 2.3 shows the equatorial electron density profile assumed herein, set to match (approximately) the form $\log_{10} N_{eq}(L) = -0.3145\,L + 3.9043$ (dashed-line) offered by *Carpenter and Anderson* [1992] for these conditions, out to some sufficiently high L-value which defines the plasmapause "knee" [*Carpenter et al.*, 1971] to permit the ray paths to venture out to at least $L = 4$.

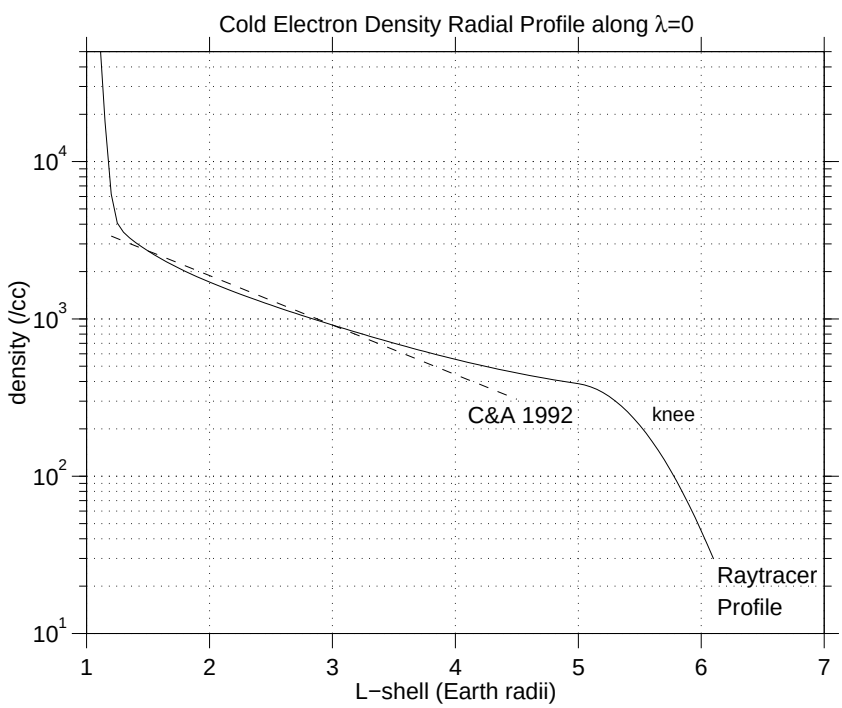

Figure 2.3: Assumed cold plasma equatorial density radial profile used for raytracing.

2.2.2 Simulated Oblique Whistlers

Example Ray Ensemble. Fig. 2.4 shows a representative ray ensemble for the midband frequency f=5 kHz. Rays are injected at altitude $h_i = 1000$ km over the latitude range $15° < \lambda_i < 62°$ at spacing $\Delta\lambda_i = 0.15°$, with initial wave normal angles at the injection points taken as locally vertical, representing the mean value for the cone of wave normal angles transmitted through the horizontally stratified ionosphere [*Helliwell*, 1965]. Rays are traced over the first traverse through the magnetosphere until at the southern-most latitudes the wave normal angles subsequently become highly oblique, leading to possible landau damping [*Thorne*, 1968; *Sazhin*, 1991] and/or total internal reflection within the magnetosphere (MR reflection) [*Draganov et al.*, 1992; *Jasna et al.*, 1998], depending on the particular prevailing hot plasma density (topics both beyond the present scope).

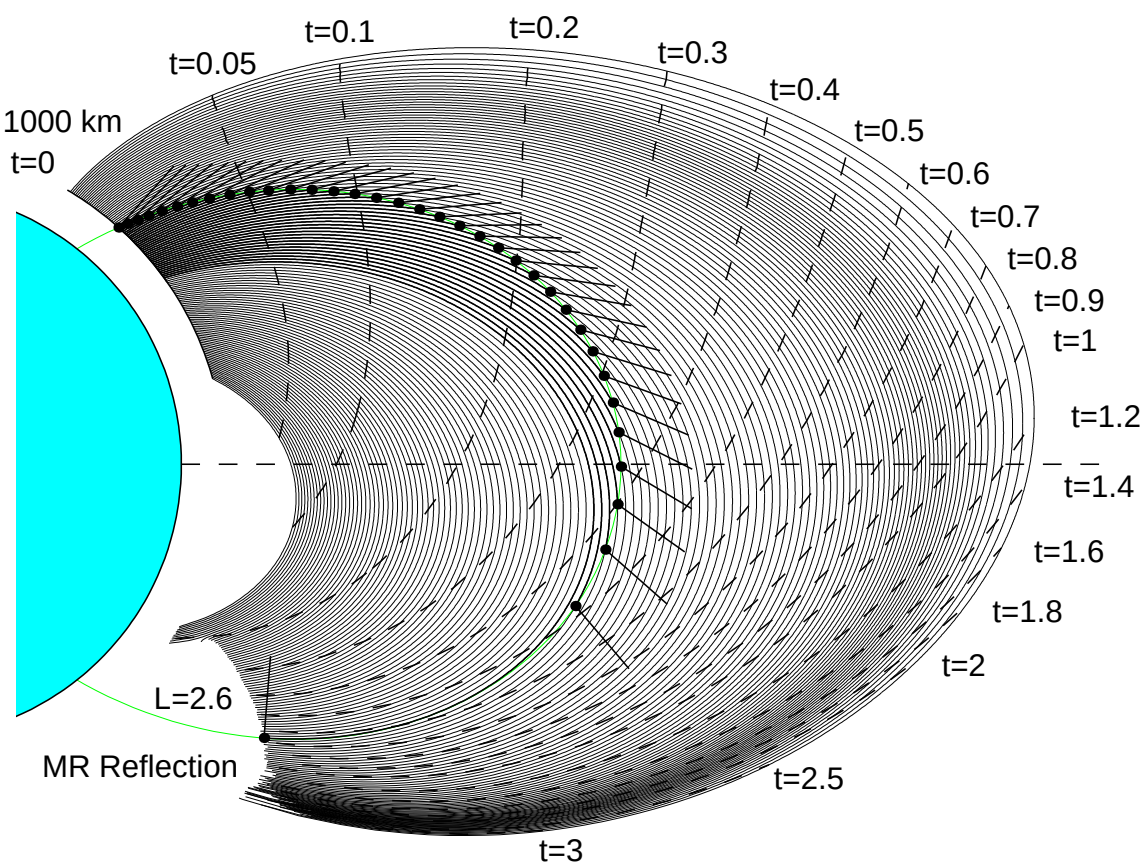

Figure 2.4: Representative oblique whistler-mode ray path ensemble for f=5 kHz. Dashed lines show wavefronts at the indicated group times; filled circles indicate ray/L-shell intersections for L=2.6.

In this figure the sequence of dashed lines which cut across the ray paths indicate representative wavefronts advancing at the ray group velocity (for this frequency), while the filled circles along $L = 2.6$ indicate a representative set of ray/L-shell intersections at which both the wave normals

(short line segments, see also Fig. 2.1) and group time values are available directly. Here the ray paths from the injection altitude $h_i = 1000$ km up to these intersection points are shown thicker for clarity. In these raytracings a rather fine injection latitude spacing and corresponding high spatial density of rays is necessary to ensure a sufficient number of ray/L-shell intersections, particularly in the southern-hemisphere where the rays become naturally field-aligned for considerable distance. In general, intersections are obtained along L-shells ranging $1.8 \leq L \leq 4.0$ at spacing $\Delta L = 0.2$.

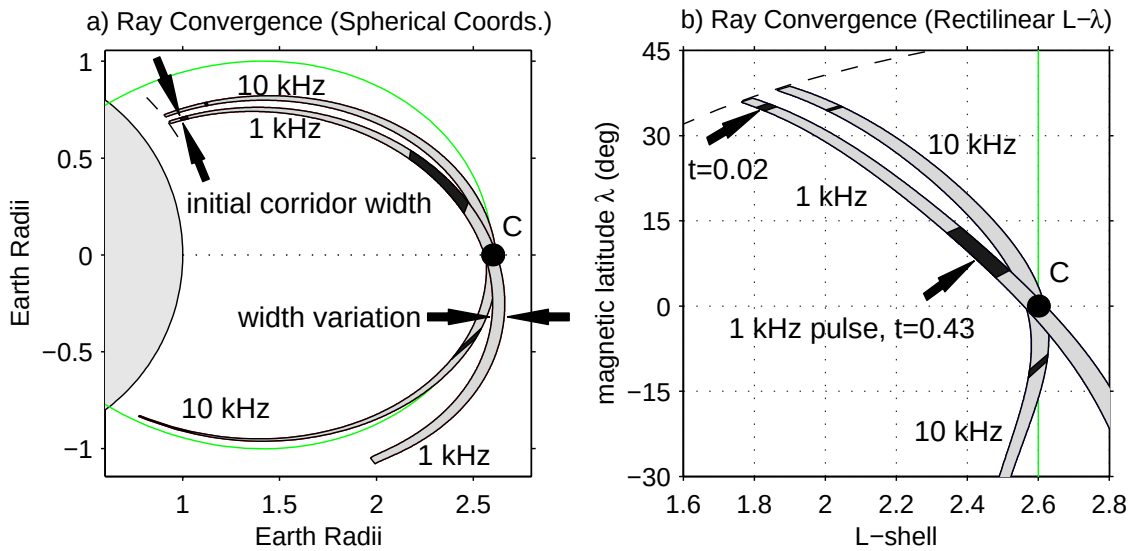

Figure 2.5: Ray convergence to a common point C from distinct injection latitudes for f=1 kHz and f=10 kHz rays, in (a) spherical and (b) rectilinear L-λ coordinates (for clarity). In general, rays at higher frequencies exhibit tighter radius of curvature as shown. The arrows in Fig. 2.5a indicate the variation in cross-sectional width of the f=1 kHz ray corridor, while the arrows in Fig. 2.5b indicate representative pulse stretching due to f-t dispersion for a 1 kHz bandwidth (exaggerated for clarity) at times t=0.02 s and 0.43 s; both of these factors are combined to determine the wave power density. The much shorter pulses along the f=10 kHz corridor (the second beyond C) in Fig. 2.5b are for the same two times.

Variation with frequency. Raytracings are repeated for frequencies 200 Hz $\leq$ f $\leq$ 10 kHz at 200 Hz spacing. In general as the frequency is changed the corresponding variation in refractive index alters both 1) the ray path curvature, and 2) the propagation delay or group time along each ray. These effects are illustrated in Fig. 2.5, which shows ray paths for two frequencies near the limits of the broadband whistler frequency range, namely $f = 1$ Khz and $f = 10$ kHz, plotted in two equivalent coordinate systems for clarity. Referring to Fig. 2.5a, rays at higher frequencies ($f = 10$ kHz) generally exhibit tighter radius of curvature than those at lower frequencies ($f = 1$ kHz), changing in a smooth manner between the indicated paths as f varies. Thus, for any two frequencies to reach the same point $C = (L, \lambda)$ they must originate at different injection latitudes, as illustrated most clearly in Fig. 2.5b. The variation in group time with f is more general and is considered in a forthcoming section.

Wave Power Density. There are two distinct and equally important factors which affect the wave power density, expressed here as $S^w = S_g^w\, S_d^w$ (given as W/m^2/Hz) for any frequency at any (L,λ) location, also illustrated in Fig. 2.5 as follows. The first factor S_g^w is associated with the change in the geometric cross-sectional area with increasing distance along the wave energy "corridor" defined by a) the pair of parallel ray paths emanating from adjacent injection points and b) the longitudinal wedge defined by an implied adjacent meridional plane containing an identical pair of ray paths (thus a full three-dimensional corridor is defined by four rays, two in each meridional plane). This S_g^w factor gives the change in steady-state wave power density which results as the area transverse to the direction of power flow (i.e. the m^2) varies along the length of the corridor. This area is calculated as the product of the corridor width transverse to the ray paths (explicitly tracked along every ray path pair, see i.e. Fig. 2.5a, just below point C), and the longitudinal arc length separating the two implied meridional planes, which increases linearly with overall distance from the center of the Earth. Then S_g^w is defined as the ratio of the cross-sectional area at each ray/L-shell intersection point to the area at the respective injection point.

The second factor S_d^w is associated with f-t dispersion and can be understood in terms of the ever-increasing time interval required for any two closely-spaced frequencies, traveling at their respective unequal propagation velocities, to pass by each of a series of points distributed over ever-increasing distance along a given wave corridor (illustrated for an exaggerated bandwidth of 1 kHz in Fig. 2.5b), *combined with* a requirement for energy conservation, applied together as follows. First, in general, over any finite bandwidth the incremental energy passing through the aperture of any particular wave corridor must be conserved, regardless of how or where it may subsequently propagate. Then by the smoothly varying magnetosphere assumption, for infinitesimal δf about any center frequency f, the change in ray path curvature for any ray is negligible, so that the infinitesimal wave pulse corresponding to such δf remains to first order within the same corridor, yet with the infinitesimal duration δt increasing with distance along that corridor. Under such conditions the argument of e.g. *Chang* [1983], Appendix B applies over such δf to each infinitesimal pulse, which here dictates that the quantity $S_d^w\ \delta t/\delta f$ hold constant along each corridor at each frequency. In the limit $\delta f \rightarrow 0$ this leads to the relation $S_d^w = S_o^w\ \partial f/\partial t_g$, where S_o^w is the reference input spectrum. In the present simulation $\partial t/\partial f$ is estimated numerically from the simulated $t_g(f)$.

Broadband Oblique Whistler Wave Packet. After all ray ensembles for all frequencies have been combined the resulting broadband whistler wave packet and wave properties behave as shown in Fig. 2.6. Here Fig. 2.6a shows wave packet snapshots at selected times, color-contoured at 1 kHz intervals. Note the substantial increase in arrival time to the magnetic equator (and beyond) for higher L-shells as compared with lower L-shells. Note also that in general the spatial extent of the packet grows both as the ray paths diverge and as dispersion causes the lower frequencies to lag behind the packet leading edge with increasing time. Also note that for later times (e.g. t=1.5 s) at high L-shells (e.g. L=4) the leading edge is no longer defined by f=10 kHz, consistent with

the development of a whistler "nose" (i.e. the frequency of minimum delay, see Fig. 2.6b for L=4, λ=0), where here this term, originally applied to ducted whistlers received on the ground [*Helliwell*, 1965], is extended to the oblique case. Fig. 2.6b (upper right) shows the resulting whistler f-t traces

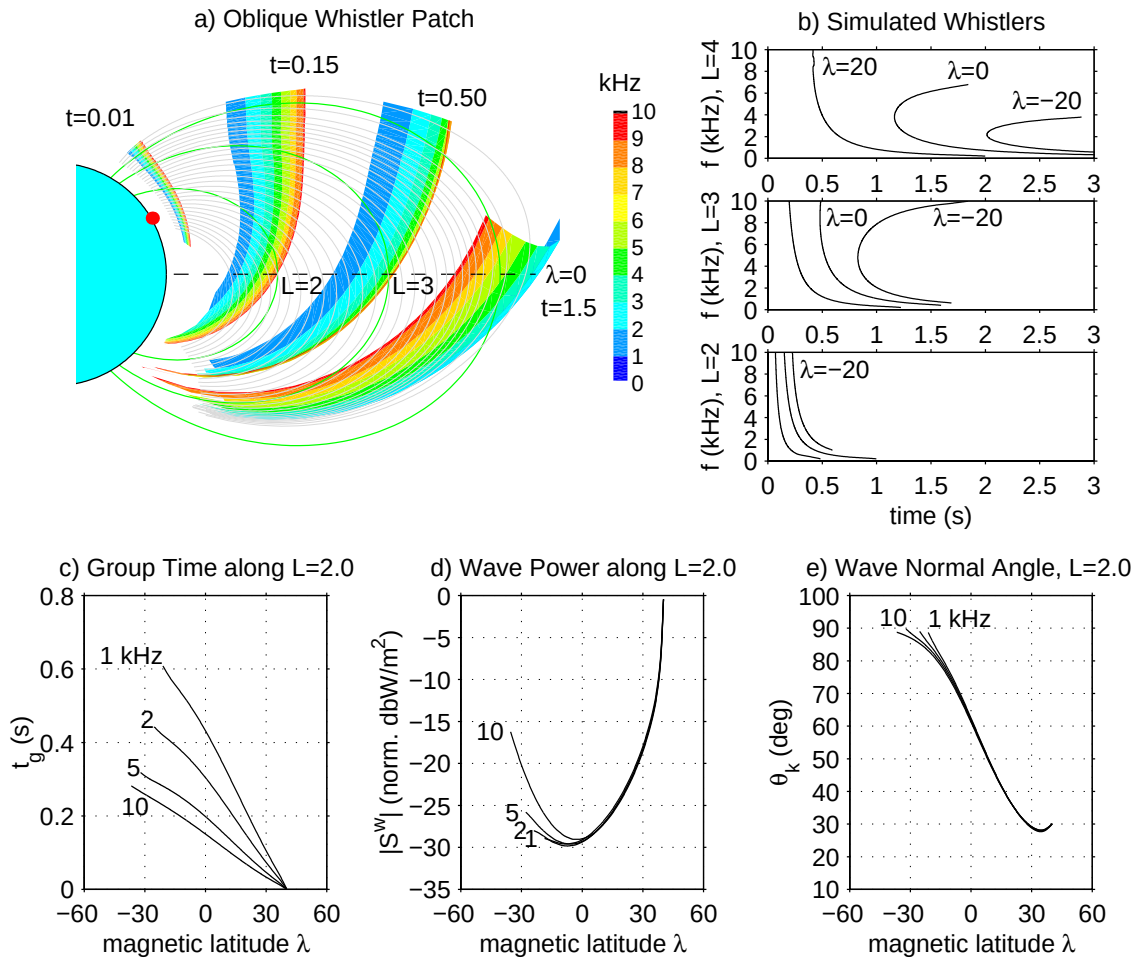

Figure 2.6: (a) Advancing broadband oblique wave packet at four successive locations, b) Simulated whistler f-t dispersion for $L = 2, 3, 4$ at $\lambda = -20, 0, 20°$, and representative wave field properties (c) group time t_g, (d) normalized wave power S^w and (e) wave normal angle θ_k along $L = 2$.

which are "observed" from the simulation at the indicated $L = 2$, 3 and 4 at magnetic latitudes $\lambda = -20°$, 0° and 20° as the wave packet passes. Note once again the large difference in arrival times over the range of L-values, and the development of the whistler nose at frequencies $f < 10$ kHz at higher latitudes for higher L-shells. In the present work, only frequencies at and below the leading frequency are considered, since observationally these frequencies tend to exhibit the greatest intensities (c.f. Fig. 2.2) and are resonant with relatively higher energy particles (c.f. Fig. 1.3), presumably leading to the dominant precipitation-related effects at the ionosphere.

Representative Wave Field Properties. Figs. 2.6c, d and e show representative wave field properties along $L=2.0$, where these final quantities have been interpolated over a uniformly-spaced latitude grid. Fig. 2.6c shows the group time t_g over latitude λ, parametric in frequency f, which by comparison with the lower panel of Fig. 2.6b for L=2 is seen to reproduce the indicated f-t traces. In like manner, Fig. 2.6d shows the variation in effective wave power, normalized to 1 W/m^2/Hz at the injection point (here at $\lambda_i \sim 40°$, corresponding to $h = 1000$ km at $L = 2$), which when multiplied by the specific input wave power spectral density (discussed in the next section) gives B_y^w via equation [2.4]. Here the wave power is seen to decrease by ~ 30 dB near the magnetic equator, owing to the combined geometric and dispersion factors, increasing somewhat at locations south of the equator (more so at higher frequencies) from the re-converging ray paths (see Fig. 2.4). This form and magnitude of wave power variation is typical for most frequencies along most L-shells. Finally, Fig. 2.6e shows the variation in wave normal angle, seen to vary nearly linearly with latitude and essentially identically for all frequencies except at the southern-most latitudes; this behavior is typical for all L-shells (although the specific $\theta_k(\lambda)$ profiles differ somewhat for each L-shell).

Anticipating the test particle calculations of Chapter 3, a particle trajectory expressed in the form $\lambda(t)$ may be overlayed onto Fig. 2.6c to determine the f-t variation specific to that particle, while the resulting (λ, f) pairs in turn select the wave power and wave normal angle from Figs. 2.6d and e. Note that by the assumed smooth variation of the phase path integral with frequency, space and time, phase coherence is maintained throughout the wave packet.

2.3 Lightning Magnetospheric Illumination Model

In the previous section a normalized input wave power density at the raytracing injection altitude was assumed, which in particular was taken to be uniform over ray injection latitude. In order to accurately determine the latitude/longitude extent of the magnetospheric region over which significant scattering and precipitation occurs it is necessary to take into account the strong spatial dependence of the electromagnetic wave intensity radiated by a lightning source at a specified location.

2.3.1 Radiation and Transionospheric Propagation

Fig. 2.7 illustrates the approach and assumptions used to determine the radiated wave spectral power density at magnetospheric altitude $h_i = 1000$ km where raytracing begins. Fig. 2.7a shows the location within the Earth-ionosphere waveguide of the assumed lightning discharge (where $R_\ell = 0$ corresponds to a given geomagnetic latitude λ_s) having specified peak radiated electric field intensity E_{100} (at reference distance $R_\ell = 100$ km measured along the ground), and also shows the association between a representative point given by coordinates (R_ℓ, ξ) at which wave energy enters the ionosphere and the location at which the wave input power is specified (in general, everywhere along

$h_i = 1000$ km). Then for a vertical cloud-to-ground lightning discharge, from the definition of current $I = dQ/dt$ and lightning dipole moment $M = 2h_eQ$ where h_e is the height of the initial $+Q$ charge above ground, the electric field at the distant point (R_ℓ, ξ) is given by *Uman* [1984] (p. 61)

$$E = \mu_o \frac{\sin\xi}{4\pi R_\ell}\left[\frac{d^2M}{dt^2}\right] = \mu_o \frac{\sin\xi}{4\pi R_\ell}\,(2\,h_e)\left[\frac{dI}{dt}\right] \qquad [2.5]$$

where R_ℓ is the distance from lightning source to observation point, ξ is measured with respect to the local vertical and where the brackets $[*]$ denote evaluation with time delay $t_o = R_\ell/c$. Radiation at VLF frequencies can be modeled by the discharge current profile (after [*Cummer and Inan*, 1997])

$$I(t) = I_o(\,e^{-bt} - e^{-at}\,) \qquad [2.6]$$

giving radiated far-field time-domain electric field E and power spectral density $S(\omega)$

$$E = \mu_o \frac{\sin\xi}{4\pi R_\ell}\,(2\,h_e\,I_o)\left[a\,e^{-at} - b\,e^{-bt}\right] \qquad [2.7]$$

$$S(\omega) = \frac{1}{Z_o}\left(\frac{\mu_o h_e I_o}{2\pi}\right)^2\left(\frac{\sin\xi}{R_\ell}\right)^2 \frac{\omega^2\,(a-b)^2}{(\omega^2+a^2)\,(\omega^2+b^2)} \qquad [2.8]$$

where $Z_o = 377\ \Omega$ is the impedance of free space, and a and b are spectrum model parameters.

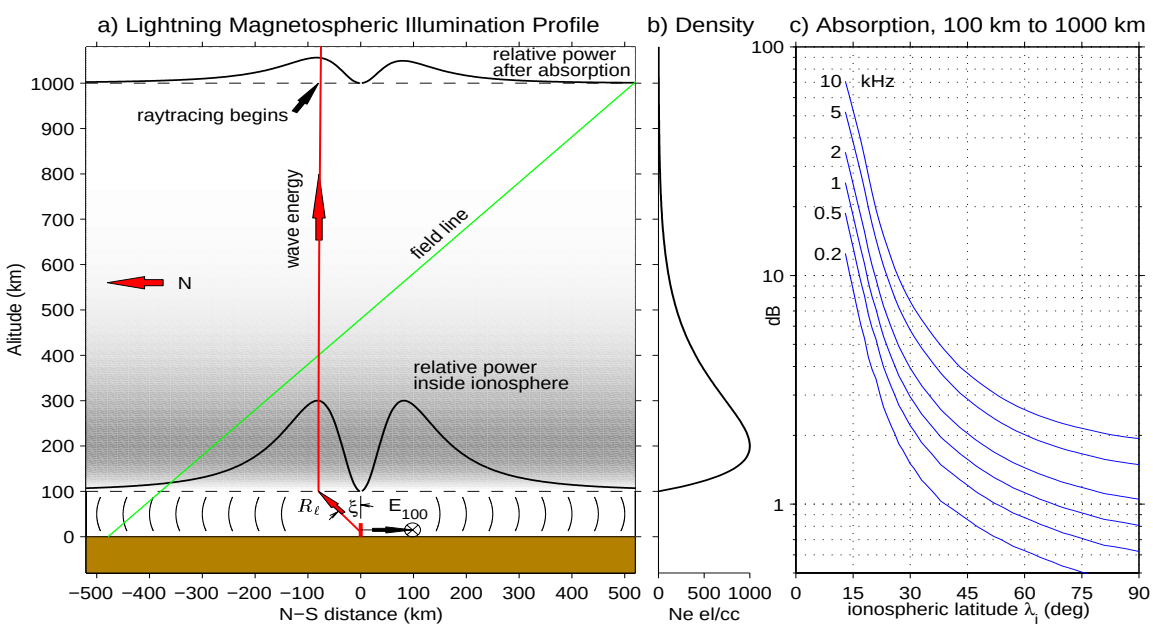

Figure 2.7: Magnetospheric illumination model: a) Lightning source and wave illumination profiles along the ionosphere lower boundary (100 km) and reaching the magnetosphere (∼1000 km) where raytracing begins; b) Assumed ionospheric electron density profile; c) Nighttime wave power absorption through the ionosphere.

In general, the impulsive could-to-ground lightning discharge radiates electromagnetic wave energy in all directions within the Earth-ionosphere waveguide (Fig. 2.7a) according to equation [2.8]. However since [2.8] assumes unbounded radiation, the classic $1/{R_\ell}^2$ factor must be modified for subionospheric propagation as follows. First, for distances $R < 100$ km the radiating wavefront indeed expands spherically (in the upper-half hemisphere) with wave power falling off as $1/{R_\ell}^2$. Then for $R_\ell > 100$ km the wave energy eventually spreads out in a more circular pattern (i.e. looking down from above), contained within the parallel boundaries of the Earth-ionosphere waveguide, so that in principle the power falloff factor approaches $1/R_\ell$ in the limit as $R_\ell \to \infty$. In reality the wave suffers additional attenuation owing to absorption by the non-perfectly conducting ground plane below and collisional losses in the ionosphere above, and furthermore exhibits a distance-dependent mode interference pattern, all of which in general requires sophisticated treatment [*Crary*, 1961; *Poulsen et al.*, 1993].

However for the present work it is sufficient to adopt the approach of *Inan et al.* [1984] which notes from the work of *Crary* [1961] that to first order the radiated (peak) power falls as $1/{R_\ell}^2$ for 100 km $< R_\ell \leq$ 1500 km and 2 dB/1000 km thereafter for $R_\ell >$ 1500 km, for points measured along the ground. Accordingly the wave power density for points along the base of the ionosphere is taken to be that given by equation [2.8] but with the $1/{R_\ell}^2$ factor modified as indicated. Then since only a fraction of this power is directed vertically upwards (especially at large R_ℓ), an additional factor[3] $\cos\xi$ is applied to estimate the available power flowing vertically upward across the free-space/ionosphere boundary ($h = 100$ km). A typical resulting (relative) pattern is shown in Fig. 2.7a as the double-peaked profile situated at $h = 100$ km altitude. Then after accounting for coupling and polarization loss (3 dB) the wave energy is taken to continue to propagate vertically from $h = 100$ km to $h_i = 1000$ km where raytracing begins, suffering significant absorption along the way, owing to collisional losses occurring primarily in the denser regions of the ionosphere $100 \leq h \leq 700$ km (c.f. Fig. 2.7b), according to the frequency- and latitude-dependent loss profiles taken from *Helliwell*, [1965] and reproduced for reference in Fig. 2.7c. A representative resulting diminished power profile is shown in Fig. 2.7a situated at $h_i = 1000$ km (on the same relative scale as the profile at $h = 100$ km).

2.3.2 Lightning Discharge Current and Spectrum

Model parameters $a = 5 \times 10^3$, $b = 1 \times 10^5$ are selected to give a typical spectrum which is broadly-peaked between $f = 2$ and $f = 6$ kHz. Then for a typical assumed lightning stroke height $h_e = 5$ km and reference current $I_o = -10.53$ kA sufficient to give $E_{100} = 10$ V/m, the corresponding current profile, radiated free-space electric field E and wave power spectral density $S(\omega)$ at reference distance $R_\ell = 100$ km (measured along the ground) are as shown in Fig. 2.8. For reference, the total VLF wave energy released into the upper half-sphere by this discharge is 52.9 kiloJoules.

[3] It turns out that inclusion of this somewhat ad-hoc $\cos\xi$ factor for vertical power flow actually gives excellent agreement with the multiple-mode results of *Crary* [1961] regarding wave field intensities just inside the ionosphere.

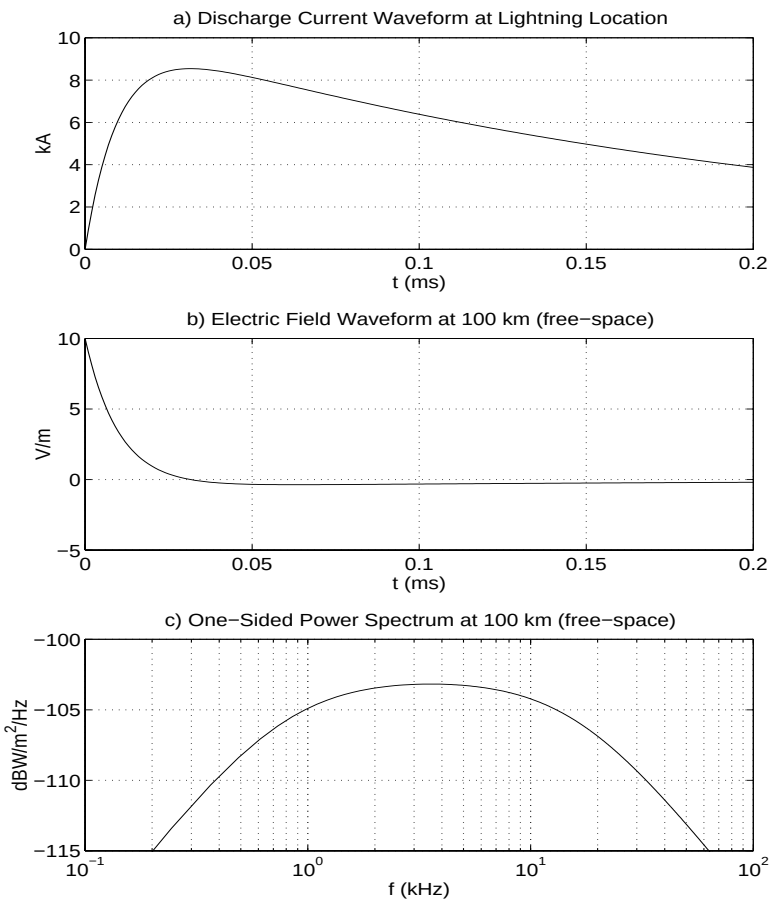

Figure 2.8: Lightning discharge waveform and spectrum: (a) current $I(t)$ at the source, (b) radiated free-space electric field $E(t)$ and (c) power spectral density $S(\omega)$, both at R_ℓ=100 km. The absolute peak current is near 8.5 kA, the peak electric field $E_{100} = 10$ V/m, and the spectral density is nearly flat over f=2 to f=6 kHz at $S \sim -103$ dBW/m^2/Hz at the E_{100} point.

2.4 Complete Oblique Whistler Model

2.4.1 Magnetospheric Whistler Intensities

Lightning Source Latitude Dependence Here the results of Sections 2.2 and 2.3 are combined to give specific assumed values for the whistler wave intensities throughout the magnetosphere. Fig. 2.9 shows lightning magnetospheric illumination contours at the injection altitude $h_i = 1000$ km from overhead (left column), intensity profiles vs. latitude (center column) for the central and an off-center longitudinal meridians (thus avoiding the pattern null), and the projected of whistler B_y^w wave field intensity (right column) in the off-center meridional plane throughout the magnetosphere, at a representative midband frequency f=5 kHz, for a lightning source of strength sufficient to give E_{100}=10 V/m at locations $\lambda_s = 20°$, 30°, 40° and 50° magnetic latitude.

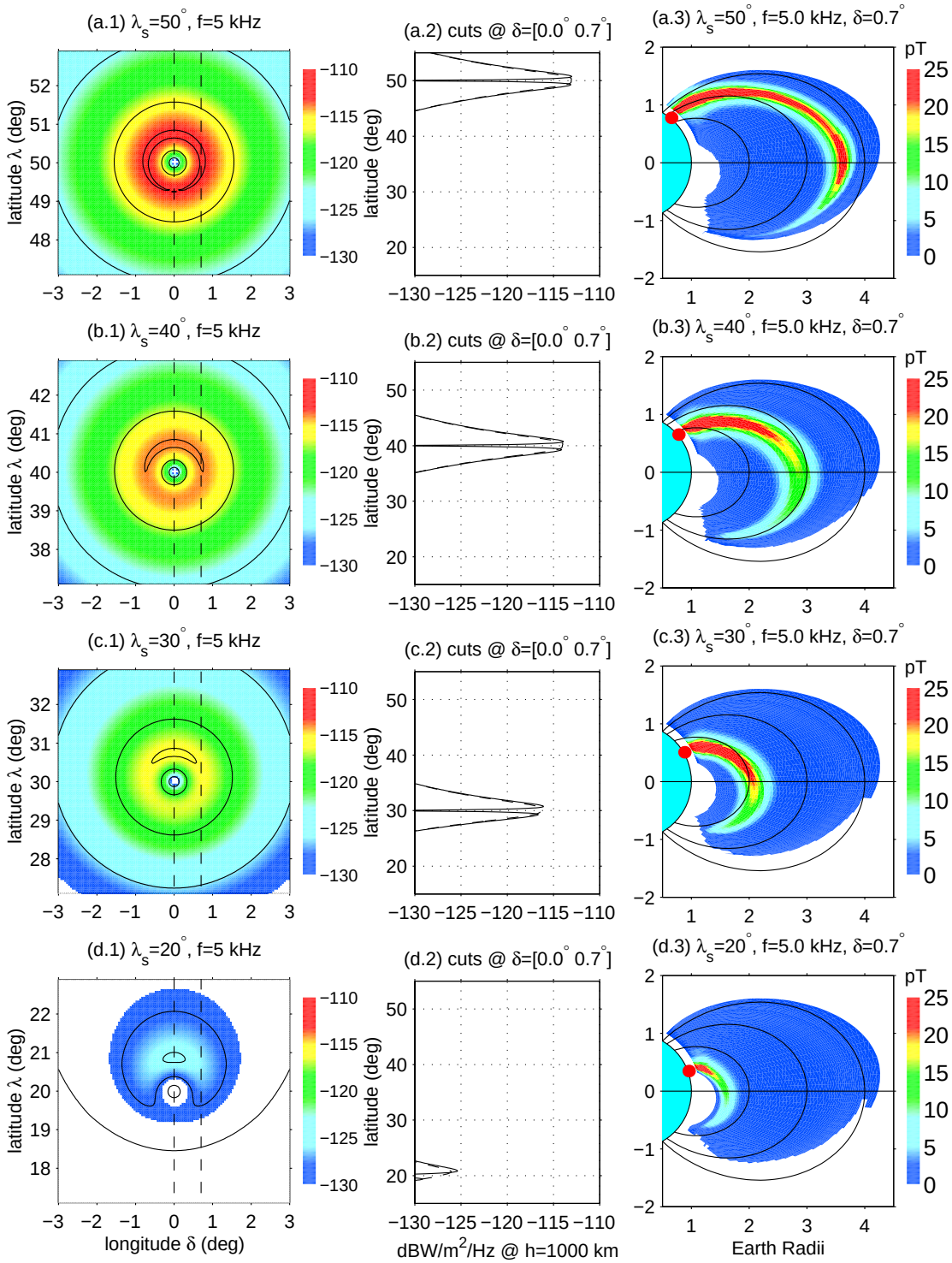

Figure 2.9: Left-column: Lightning energy incident at $h_i = 1000$ km where raytracing starts, after accounting for coupling loss and ionospheric absorption, for a lightning source giving E_{100}=10 V/m (for model parameters given in the text) and located at latitudes λ_s = 20°, 30°, 40° and 50°. Center-column: Wave power spectral density profiles vs. latitude for the indicated slices along constant longitude. Right-column: Whistler B_y^w component intensities for f=5 kHz throughout the magnetosphere, after accounting for ray defocusing and f-t dispersion as determined by raytracing.

2.4.2 Oblique Whistler Equatorial Intensities

For reference and to facilitate later comparisons, Fig. 2.10 shows equatorial wave magnetic field intensities over L-shell at $f = 1$ and $f = 5$ kHz for lightning locations $\lambda_s = 30°$, $40°$ and $50°$, each of which leads to an intensity peak at some L-value within the range of interest $1.8 \leq L \leq 4.0$. Here for $E_{100} = 10$ V/m the peak B_y^w values for f=1 kHz range $\sim$6 to 7 pT at roughly $L = 2.2$, 3.0 and 3.8 for $\lambda_s = 30°$, $40°$, and $50°$ respectively, while those for $f = 5$ kHz are several times greater (from the generally reduced dispersion which maintains higher wave energy density) at somewhat lower L-values (from the tighter ray path curvature) as expected for higher frequencies. The peaks for $f = 5$ kHz which occur at $L = 3.6$ (primary, for $\lambda_s = 50°$, and secondary, for $\lambda_s = 30°$, $40°$) are particularly strong owing to the near-zero values of $\partial t_f / \partial f$ (leading to higher effective wave power, c.f. Section 2.2) for the oblique whistler nose which just happens to develop near 5 Khz for $L \sim 3.6$.

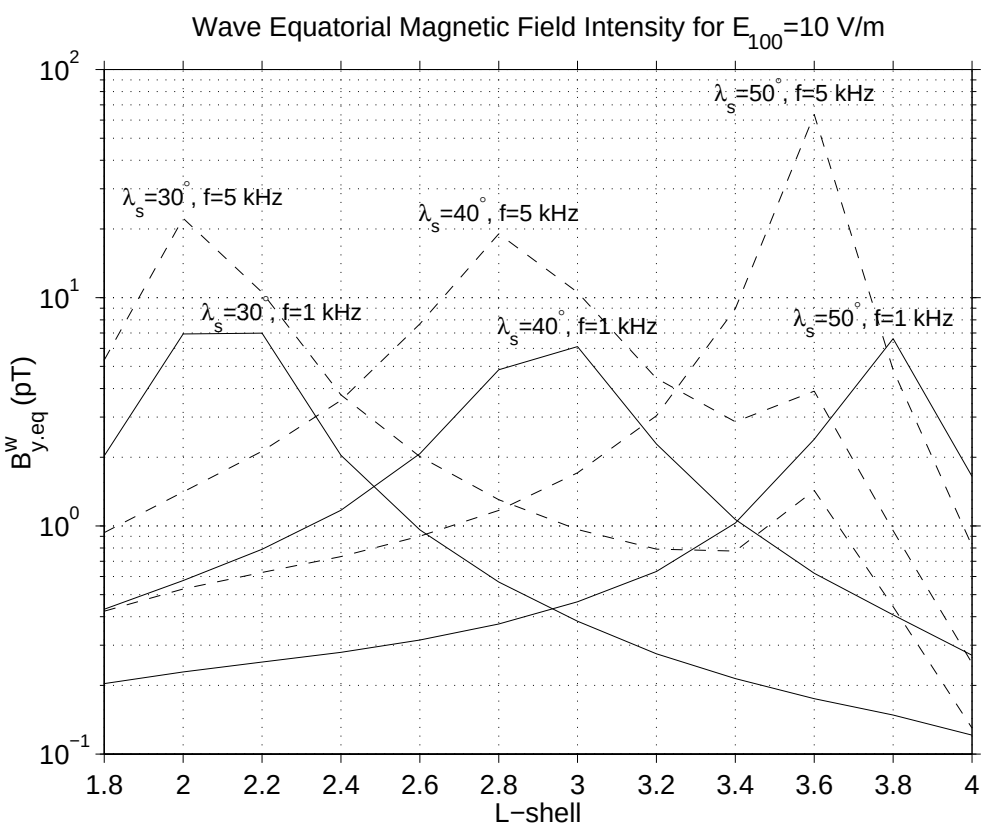

Figure 2.10: Wave equatorial magnetic field intensities for f=1 and f=5 kHz for E_{100}=10 V/m.

With the wave properties now completely specified at all points within the magnetospheric regions of interest, the pitch angle scattering and precipitation of the trapped energetic radiation belt electrons can now be determined, as detailed next in Chapter 3.

Chapter 3

Precipitation Signatures

"Flash forth lightning and scatter them! [Psalm 144:6]"

This Chapter applies the oblique whistler wave fields developed in Chapter 2 to the equations of motion given in Chapter 1 to calculate the resulting pitch-angle scattering, precipitation energy flux signatures and integral energy flux-time profiles at the foot of selected L-shells. Results are presented in a manner which shows the variation of these signatures with proximity of a given L-shell to the spatial regions of maximum whistler wave intensity for several assumed lightning source latitudes.

3.1 Formulation Overview

As indicated in Section 1.3 the formulation employed here is similar to that used in previous work for transient wave packets [*Inan et al.*, 1982; *Chang et al.*, 1983; *Chang and Inan*, 1985], where in the present work the equations of motion are those for oblique wave resonance [*Bell*, 1984; *Jasna et al.*, 1993] given in Chapter 1, and the applied space- and time-varying oblique waves fields are those developed in Chapter 2. Since many of the details of the simulation are identical to or straightforward extensions of those detailed in the indicated references, a brief summary will suffice.

Referring to Fig. 3.1a, as the wave propagates from northern to southern latitudes, at each of a succession of wavefront encounter latitudes $\lambda_{\rm wf}$ along any given L-shell of interest, a distribution of northward streaming energetic electrons (1 keV up to 3 MeV in general, but tailored to each $\lambda_{\rm wf}$), all having pitch-angles initially at the edge of the loss-cone, enters the advancing wave packet. The test particles comprising each distribution subsequently undergo gyroresonance scattering at some location $\lambda_{\rm res} \geq \lambda_{\rm wf}$ for which the resonance condition (equation [1.8]) is satisfied specific to each particle's parallel velocity $v_{\|}$. The wave fields which prevail along each test particle trajectory are determined by first noting the time of the initial wavefront encounter $t_{\rm wf}$ (determined by the time required for the leading frequency of the whistler wave packet to reach $\lambda_{\rm wf}$ in a fixed laboratory reference frame) and subsequently adding the accumulated particle transit time $t_p(\lambda)$ associated with the advance of the particle along the field line from $\lambda_{\rm wf}$ to higher latitudes, to continually track, at each integration step, the overall laboratory time $t_{\rm lab}(\lambda) = t_{\rm wf} + t_p(\lambda)$ and the wave frequency f for which $t_g(\lambda, f) = t_{\rm lab}(\lambda)$ is satisfied (for this L-shell), which in turn selects the corresponding

wave power S^w and wave normal angle θ_k for the given (f, λ) pair so determined (see Section 2.2 and Fig. 2.6). For very high velocities (particle energies $\sim$1 MeV), the wave packet appears nearly stationary as the particle passes through, while for low velocities (1 keV, at higher L), the packet may advance substantially with each particle step; in all cases the formulation fully accounts for the relative motion between the particle and the wave packet.

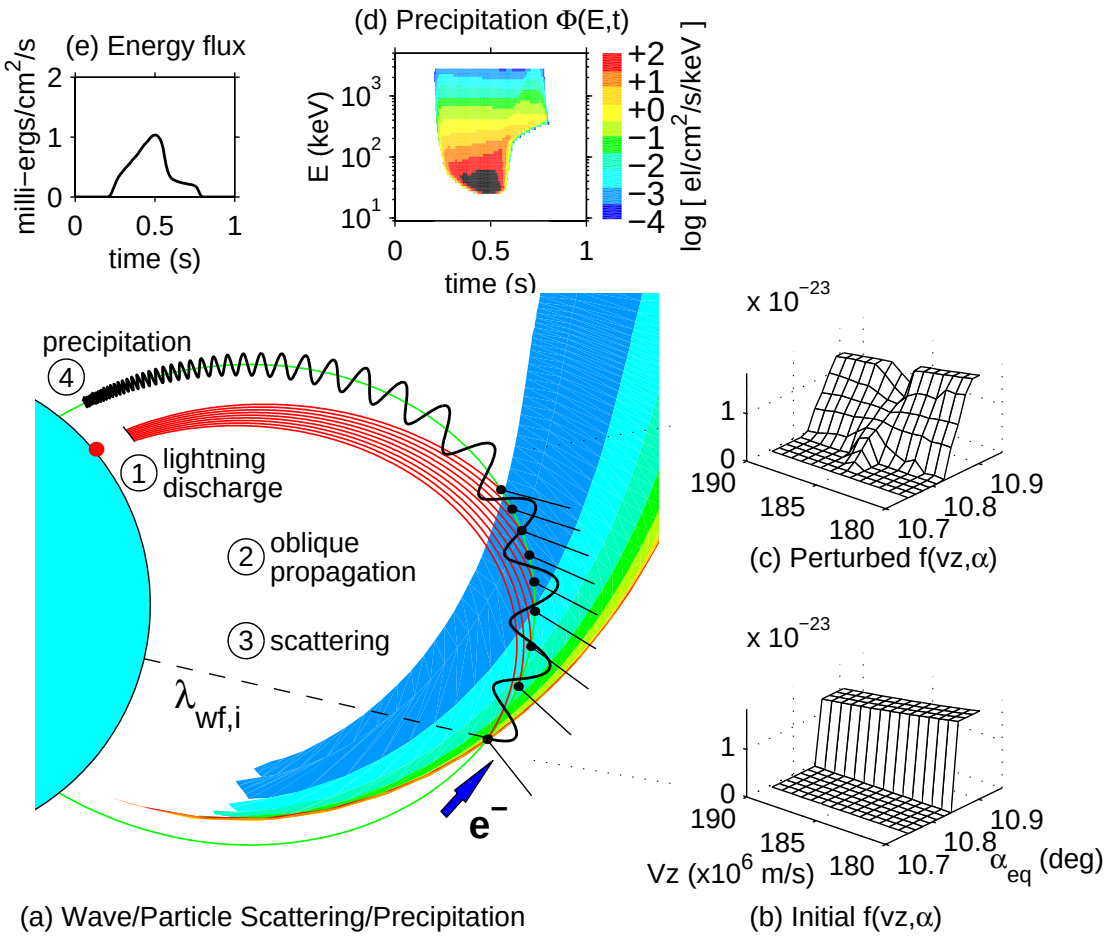

Figure 3.1: Formulation for each L-shell. Counter-clockwise from lower-left: (a) Basic event sequence: (1) lightning discharge, (2) oblique whistler propagation, (3) gyroresonance scattering, (4) precipitation. (b) Initial energetic electron flux distribution entering the wave packet for this $\lambda_{\rm wf}$, having initially void loss-cone, (c) Perturbed flux distribution after gyroresonance interactions with the wave showing scattering into the loss-cone, (d) Precipitation flux signature $\Phi(E,t)$ for loss-cone particles from all $\lambda_{\rm wf}$ along this L, (e) Precipitation energy flux pulse $Q(t)$ deposited to the atmosphere determined by integrating the quantity $E\,\Phi(E,t)\,dE$ over energy.

In calculating the scattering, each $v_\parallel$ value is applied to a constellation of 12 test particles all having initial loss-cone pitch angle $\alpha^i_{\rm eq} = \alpha^{\rm lc}_{\rm eq}$ (equation [1.4]) and distributed uniformly over initial relative wave/particle gyrophase η_o between the particle velocity and wave $\mathbf{B^w_R}$ vectors (Fig. 1.2c and equation [1.7]), as this phase ultimately determines whether a given particle is scattered to greater or lesser pitch angle. As the equations of motion are integrated each particle takes on a unique trajectory $v_\parallel(\lambda, \eta_o)$, $v_\perp(\lambda, \eta_o)$ and $\eta(\lambda, \eta_o)$, while afterwards the resulting local pitch angles $\alpha = \tan^{-1} v_\perp / v_\parallel$ are subsequently referred to their corresponding adiabatically-mapped equatorial values and subtracted from the assumed initial $\alpha^{\rm lc}_{\rm eq}$ value to obtain, for λ sufficiently beyond the resonance region, the set of final pitch angle *deviations* $\Delta\alpha_{\rm eq}(v_\parallel, \eta_o)$ over $v_\parallel$ and η_o. Thus the final scattered pitch angles are given by $\alpha^f_{\rm eq}(v_\parallel, \eta_o) = \alpha^i_{\rm eq} + \Delta\alpha_{\rm eq}(v_\parallel, \eta_o)$.

In general, roughly half the particles are scattered to larger pitch angles ($\Delta\alpha_{\rm eq} > 0$) and half to smaller pitch-angles ($\Delta\alpha_{\rm eq} < 0$), the later with correspondingly lower mirror altitudes (Section 1.3). Also, as it turns out, the $\Delta\alpha_{\rm eq}(v_\parallel, \eta_o)$ values remain essentially unchanged as the initial pitch-angle $\alpha^i_{\rm eq}$ is varied up to several degrees to either side of the loss-cone; this behavior permits one $\Delta\alpha_{\rm eq}(v_\parallel, \eta_o)$ set calculated for $\alpha^i_{\rm eq} = \alpha^{\rm lc}_{\rm eq}$ to be applied at values $\alpha^i_{\rm eq} > \alpha^{\rm lc}_{\rm eq}$ in order to account for particles not initially at the loss-cone edge which are nonetheless scattered to some $\alpha^f_{\rm eq} < \alpha^{\rm lc}_{\rm eq}$.

Each $\Delta\alpha_{\rm eq}(v_\parallel, \eta_o)$ set is thus replicated over the range $\alpha^{\rm lc}_{\rm eq} \le \alpha^i_{\rm eq} \le \alpha^{\rm lc}_{\rm eq} + \max|\Delta\alpha_{\rm eq}|$, and applied to the initial energetic particle phase space density[1] $f^i_v(v_\parallel, \alpha_{\rm eq})$ – taken as initially void for $\alpha_{\rm eq} < \alpha^{\rm lc}_{\rm eq}$ (Fig. 3.1b) – to obtain the perturbed density $f^p_v(v_\parallel, \alpha_{\rm eq})$ – generally non-void for $\alpha_{\rm eq} < \alpha^{\rm lc}_{\rm eq}$ (Fig. 3.1c) – in the manner prescribed by *Inan et al.*, [1982]. This perturbed density f^p_v is then converted to an equivalent flux distribution function $j(E, \alpha_{\rm eq})$ [*Chang and Inan*, 1985], where the mapping $(v_\parallel, \alpha_{\rm eq}) \rightarrow (E, \alpha_{\rm eq})$ is performed as in *Jasna et al.*, [1993].

This procedure is repeated for wavefront latitudes $\lambda_{\rm wf}$ over the range $-36.5° \le \lambda_{\rm wf} \le 32.5°$ at spacing $\Delta\lambda_{\rm wf} = 1°$, and the resulting set of flux distribution functions $j_{\rm wf}(E, \alpha_{\rm eq})$ are subsequently integrated over the loss-cone ($0 \le \alpha_{\rm eq} \le \alpha^{\rm lc}_{\rm eq}$) and combined to give the precipitation flux $\Phi(E, t)$ at the foot of each L-shell (see Fig. 3.1d), adjusting for solid angle and magnetic flux tube convergence at the (L-shell dependent) precipitation latitude λ_p (given by $\cos^2\lambda_p = (R_e + h_p)/(L\,R_e)$ where h_p is the assumed precipitation altitude) according to

$$\Phi(E,t) = 2\pi \frac{\sqrt{1 + 3\sin^2\lambda_p}}{\cos^6\lambda_p} \sum_{\lambda_{\rm wf}} \int j_{\rm wf}(E,\alpha)\ \cos\alpha\ \sin\alpha\, d\alpha \qquad [3.1]$$

where the summation $\sum$ indicates the superposition of the consecutive precipitation energy-time (E-t) profiles which result as each $j_{\rm wf}(E, \alpha)$ is adjusted for the energy-dependent particle transit time required to reach λ_p from each respective wavefront encounter latitude $\lambda_{\rm wf}$, as described in

[1] $f^i_v(v_\parallel, \alpha_{\rm eq})$ is taken as void for $\alpha_{\rm eq} < \alpha^{\rm lc}_{\rm eq}$ and uniform for $\alpha_{\rm eq} \ge \alpha^{\rm lc}_{\rm eq}$, with velocity dependence $f_v \sim 1/{\rm v}^6$ and scaled to give flux $j_o = 1 \times 10^8$ el/cm^2/s/keV at E=1 keV [*Schield and Frank*, 1970] after *Inan et al.*, [1985].

[*Inan et al.*, 1982]. Finally, the number of precipitating electrons $N(t)$ and the associated energy flux $Q(t)$ which they represent are found by integrating $\Phi(E,t)$ over energy as

$$N(t) = \int_{E>E_{\rm th}} \Phi(E,t)\,dE, \qquad Q(t) = \int_{E>E_{\rm th}} E\;\Phi(E,t)\,dE \qquad [3.2]$$

respectively, where a lower integration limit $E_{\rm th}$ is introduced (where possibly $E_{\rm th} = 0$) in order to explore the energy dependence of these results, as well as facilitate comparison with particle detector measurements made for energies above some sensitivity threshold.

3.2 Resonance and Scattering Details

3.2.1 Dynamic Resonance Condition

The scattering calculations are carried out for each test particle at precisely those locations along the field line where the particle experiences resonance with some portion of the wave packet, given by $v_\parallel \sim v_{\rm res}$, or equivalently, by near-zero values of the resonance parameter $\epsilon = |(v_\parallel - v_{\rm res})/v_{\rm res}|$, where $v_\parallel$ is the particle's nominal adiabatic parallel velocity and $v_{\rm res}$ is given by equation [1.8]. Strong resonance is indicated wherever $\epsilon < \sim 1\%$, with the highest scattering rates occurring for $\epsilon < \sim 0.2\%$. Since $v_\parallel$ and $v_{\rm res}$ both vary with latitude, and since in addition $v_{\rm res}$ is parametric in wave *f-t* behavior, this *dynamic* resonance condition is best presented in the form of curves for $v_{\rm res}$ and corresponding $E_{\rm res}$ (see Section 1.3) evaluated for a representative particle having specified equatorial parallel velocity $v_{||,eq}$ over a range of consecutive wavefront encounter latitudes $\lambda_{\rm wf}$ in the manner of *Chang and Inan* [1985]. Such curves will also guide the interpretation of certain key features in the resulting scattering and precipitation signatures $\Delta\alpha_{\rm eq}(E,t)$ and $\Phi(E,t)$.

Fig. 3.2a (bottom panel) shows resonance curves $v_{\rm res}(\lambda)$ parametric in $\lambda_{\rm wf}$ (solid lines) for a particle having $v^*_{||,eq} = 2.316 \times 10^8$ m/s traveling along $L = 2.2$. The value specified by any $v_{\rm res}$ curve indicates the parallel velocity which a loss-cone particle must have in order to be in resonance with the wave. For this representative particle, such velocity match is evident wherever the adiabatically-mapped particle parallel velocity $v^*_{||,eq} \rightarrow v_\parallel(\lambda)$ curve (dashed lined) intersects any $v_{\rm res}$ curve. Fig. 3.2b (above) shows corresponding curves for resonant particle total energy $E_{\rm res}(\lambda)$, where $v^*_{||,eq}$ maps to $E_{\rm tot} = 335.4$ keV (for loss-cone pitch angle $\alpha^{\rm lc}_{\rm eq} = 14.28°$). Here although the calculated $v_{\rm res}$ and $E_{\rm res}$ curves are specific to this particular $v^*_{||,eq}$, it turns out that their variation over $v_{||,eq}$ is sufficiently slow and smooth so that they may be taken to apply in an approximate sense over the range of particle velocities and energies indicated by the respective vertical axes. For reference, also shown (above) in Figs. 3.2c, d and e are, respectively, the frequency f, wave normal angle θ_k and wave power S^w (for a lightning source with $E_{100} = 10$ V/m located at $\lambda_s = 30°$) seen by a particle having this value of $v^*_{||,eq}$.

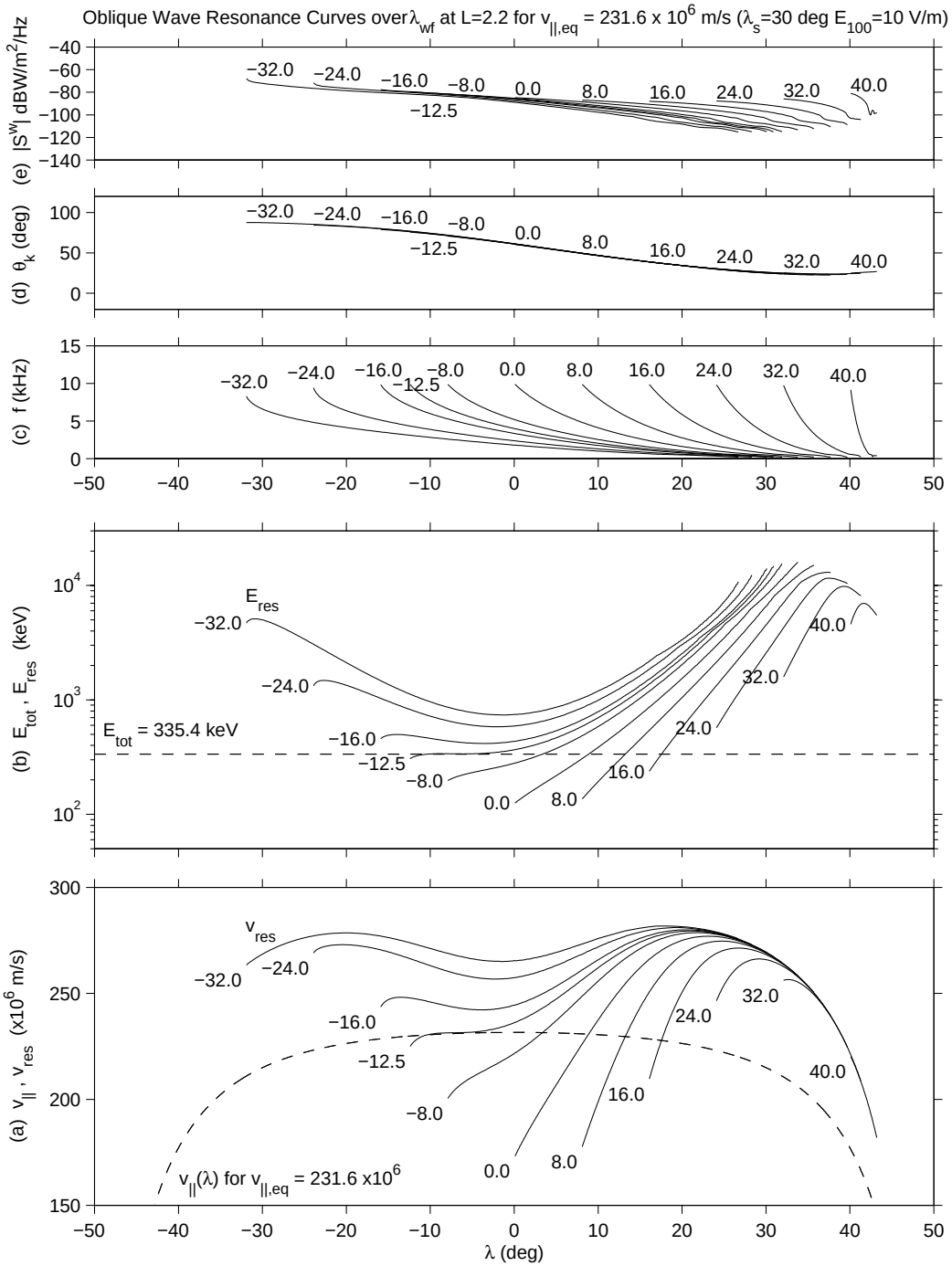

Figure 3.2: Dynamic Resonance Curves (bottom-to-top). Curves of (a) $v_{\rm res}(\lambda_{\rm wf}, \lambda)$ and corresponding total (b) $E_{\rm res}(\lambda_{\rm wf}, \lambda)$ for loss-cone electrons along $L = 2.2$ entering the oblique whistler wave packet at $\lambda_{\rm wf} = -12.5°$. The dashed lines show $v_{\|}(\lambda)$ and $E_{\rm tot}$, respectively, for a particle with $v^*_{\|,eq} = 231.6 \times 10^6$ m/s, which happens to be *the particle* which experiences maximal scattering due to the extended interaction length for $\lambda_{\rm wf} = -12.5°$. Also shown above (third panel and upwards) are the (c) wave frequency f, (d) wave normal angle θ_k and (e) wave power density S^w (for a lightning source at $\lambda_s = 30°$) seen by this particle.

Referring to Fig. 3.2b, since a particle's $E_{\rm tot}$ remains constant[2] over latitude, segments of any $E_{\rm res}$ curve exhibiting zero slope indicate regions of extended wave/particle resonance regions (or interaction lengths) over which, other things being equal, the cumulative scattering will be greater (larger $\Delta\alpha_{\rm eq}$) than for adjacent locations or at neighboring energies. Here an especially long resonance region, or interaction length, occurs over latitude $-11^\circ \leq \lambda_{\rm res} \leq -2^\circ$ for $\lambda^*_{\rm wf} = -12.5^\circ$ as shown by the merged dashed and solid lines (in both the $v_{\rm res}$ and $E_{\rm res}$ plots). This interaction length ($\sim 9^\circ$) happens to be the maximum value attained over all combinations of $v_{||,eq}$ and $\lambda_{\rm wf}$ anywhere along this L-shell, hence the "star" designations for $v^*_{||,eq}$ and $\lambda^*_{\rm wf}$. It turns out that along every L-shell considered there is always some L-dependent wavefront latitude ${\lambda^*_{\rm wf}}'$, almost universally in the range $\sim -16 < {\lambda^*_{\rm wf}}' < -10^\circ$, for which some particular L-dependent ${v^*_{||,eq}}'$ value gives a similar maximal interaction length on the order of 5° to 10°.

The $v_{\rm res}$ and $E_{\rm res}$ curves in Fig. 3.2 also show a variety of minor extended (i.e. zero slope) resonance regions, noted here as (a) the concave-down leading edges for wavefront latitudes $\lambda_{\rm wf} < 12^\circ$, (b) the similar concave-down trailing edges for $\lambda_{\rm wf} > 8^\circ$ (evident only in the $E_{\rm res}$ curves), and (c) the broad concave up regions for $\lambda_{\rm wf} < -12.5^\circ$, where this third type is essentially the same as occurs for strictly parallel propagation. Note that here the broad concave up regions blend with the leading edge concave-down region for the $\lambda^*_{\rm wf} = -12.5^\circ$ curve (for this L-shell) thereby giving the maximal interaction length for this particular wavefront latitude. In general this overall variety of extended resonances occurs in similar manner for all L-shells considered, although the precise value of $\lambda^*_{\rm wf}$ varies somewhat, as mentioned above.

The systematic behavior of these various minor and maximal extended resonance regions in turn gives rise to particular features in the energy-time scattering $\Delta\alpha_{\rm eq}(E,t)$ and precipitation $\Phi(E,t)$ signatures to be discussed further in forthcoming sections. The concave-down leading edges are of particular interest as these arise specifically from the non-zero values for the wave normal angles (Fig. 2.6e) and lead to associated features in the E-t signatures which are thus unique to the case of oblique wave propagation as compared to the case of strictly parallel propagation ($\theta_k = 0$).

3.2.2 Scattering Trajectories $\Delta\alpha_{\rm eq}(\lambda)$

Fig. 3.3 shows the detailed resonance condition and resulting scattering trajectories for a representative case where the 12 test particles distributed uniformly over initial wave/particle relative gyrophase η_o, all have $v^*_{||,eq} = 2.316 \times 10^8$ m/s and traveling northward along $L = 2.2$ and entering the whistler wave packet at $\lambda^*_{\rm wf} = -12.5^\circ$ (the values previously shown to give the maximum interaction length). Fig. 3.3a (top panel) shows, on a common axis, the frequency (solid line) and wave magnetic field B^w_y component intensity (dashed line) seen by these particles. Here the wave intensity ranges $\sim$16 to 8 pT as the frequency falls from f=10 kHz to 300 Hz (and lower for $\lambda > 5^\circ$).

[2] $E_{\rm tot}$ remains essentially constant, even during scattering, for the range of wave intensities considered herein.

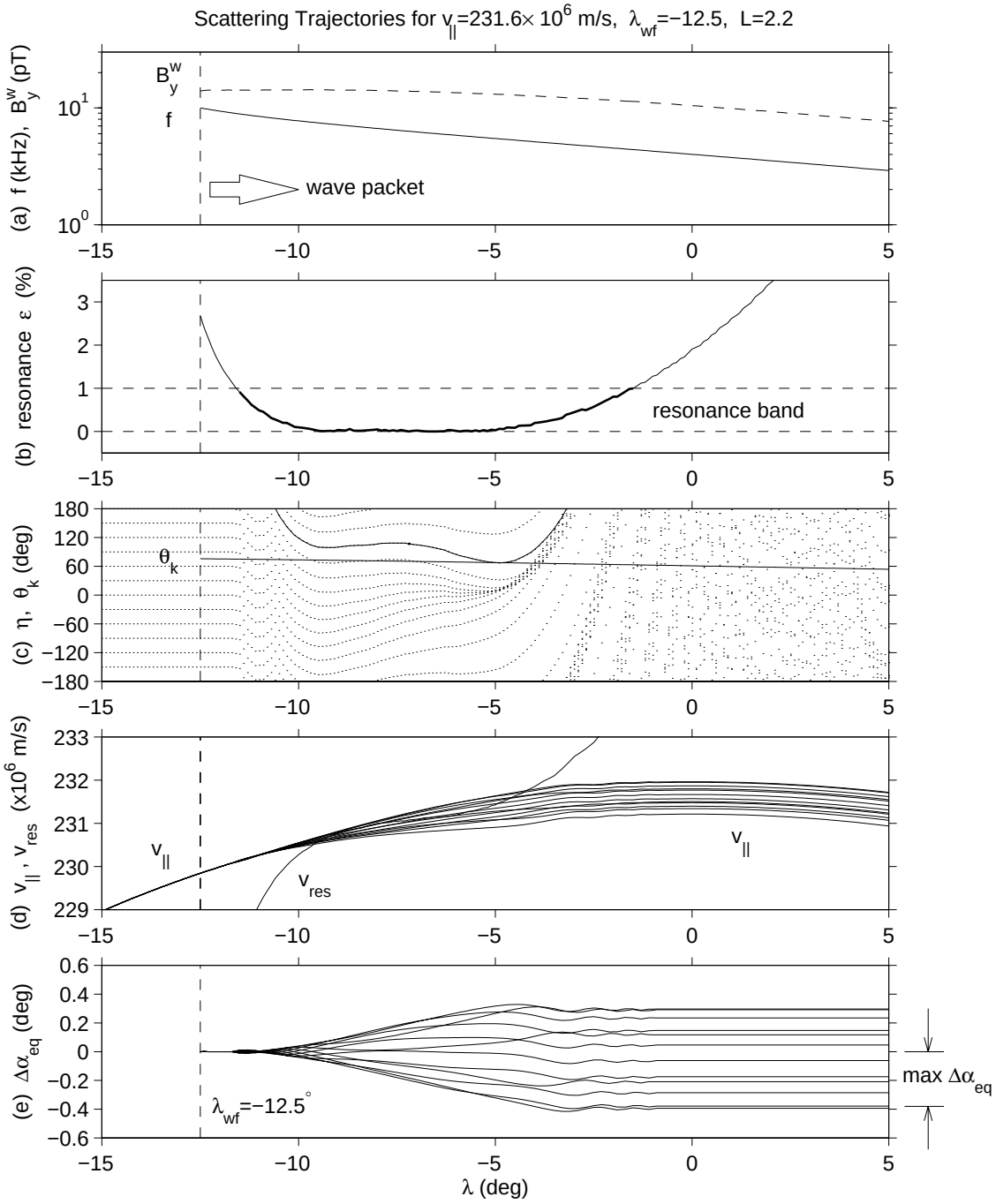

Figure 3.3: Typical oblique resonance and scattering trajectories (top down): (a) frequency f (kHz) and wave intensity B_y^w (pT) (on common log scale) seen by a particle moving along $L = 2.2$ with initial equatorial velocity $v_{||,eq} = 231.6 \times 10^6$ m/s and entering the wave packet at $\lambda_{\rm wf} = -12.5°$, (b) resonance parameter $\epsilon = (v_{\|} - v_{\rm res})/v_{\rm res}$ with 1% resonance band, (c) wave/particle relative gyrophase η (dotted, with one trajectory shown solid over the latitude range of strongest interaction) for twelve test particles sharing $v_{||,eq}$, distributed uniformly over initial phase η_o, also, wave normal angle θ_k (solid), (d) resonance velocity $v_{\rm res}$ and scattered parallel particle velocity $v_{\|}(\lambda, \eta_o)$ for these twelve particles, (e) resulting $\Delta\alpha_{\rm eq}(\lambda, \eta_o)$ scattering trajectories; $\max|\Delta\alpha_{\rm eq}|$ over η_o is indicated.

Fig. 3.3b (below) shows the value of the resonance parameter $\epsilon = |(v_{\|} - v_{\rm res})/v_{\rm res}|$ with the 1% resonance band indicated (appropriate for this velocity). Fig. 3.3b (middle panel) shows, on a common axis, the wave normal angle $\theta_k \sim 60°$ (solid) and the twelve gyrophase η trajectories (dotted), initially uniformly over $\pm 180°$ and subsequently altered during resonance, with one trajectory shown solid over the range of latitudes for which the interaction is strongest. Shown below in Fig. 3.3d are the twelve parallel particle velocity trajectories $v_{\|}(\lambda, \eta_o)$, perturbed from their otherwise adiabatic values during resonance, as well as the $v_{\rm res}$ resonance curve for $\lambda_{\rm wf} = -12.5°$ (close up of the same curve as in Fig. 3.2a). Lastly, Fig. 3.3e (bottom) shows the resulting pitch angle deviations $\Delta\alpha_{\rm eq}(\lambda, \eta_o)$ from the otherwise constant loss-cone value ($\alpha_{\rm eq}^{\rm lc} = 14.28°$, for $L = 2.2$). The maximum absolute deviation $\max|\Delta\alpha_{\rm eq}|$ (over η_o) is indicated at the right-side end of this panel, where for the present case, those particles most scattered have been deflected by $\max|\Delta\alpha_{\rm eq}| \simeq 0.4°$. In general, peak scattering for other $v_{||,eq}$ and $\lambda_{\rm wf}$ will be less from the generally reduced interaction lengths.

A number of detailed comments are in order. First, up to this point the interaction length has been identified with the 1% resonance band. Here it is seen that the most significant scattering occurs over $-11° \leq \lambda_{\rm res} \leq -3°$, so that this 1% resonance band tolerance is sufficiently large (for these velocities) to permit the deviations to settle to their final values (e.g. for $\lambda > -2°$). In general, a velocity-dependent resonance band defined by $\epsilon < (c/v)\%$, where c is the speed of light and v is the total particle velocity, is found to work well. Nonetheless in previous formulations the interaction length has been defined more precisely as the number of degrees of latitude (or alternatively, kilometers along the field line) required for the relative wave/particle phase, here denoted η, to change by π radians over the course of the interaction. While this definition is meaningful whenever η exhibits more or less overall monotonic behavior, proceeding from e.g. $-\pi/2$ to $\pi/2$ (i.e. "/"-shaped), here the oblique wave normal angles often lead to η trajectories which are "U"-shaped or even "W"-shaped (see the solid line η trajectory in Fig. 3.3c), which thus never actually traverse a full π radians. This suggests a more general definition whereby the interaction length is defined as that distance for which η remains within $\pm\pi/2$ of the central value it takes where $\epsilon = 0$. The maximum interaction length over η so defined in this case is 7.7°, and holds for the trajectory shown as the solid η trajectory in Fig. 3.3c. Note that this segment of $\eta(\lambda)$ so indicated corresponds well to the range of λ over which the scattering rate (i.e. $\partial\Delta\alpha/\partial\lambda$) is maximum, as seen in Fig. 3.3e.

Second, note that appreciable phase bunching occurs by $\lambda_{\rm res} \sim -5°$ just prior to the exit from the resonance region. Such bunching calls for comparison with the threshold for oblique-wave particle trapping [*Bell*, 1986], and consideration of possible significant re-radiated fields which, through positive wave/particle feedback, can lead to *in-situ* wave growth, pushing the interaction into non-linear regimes [*Helliwell and Inan*, 1982; *Carlson et al.*, 1990]; however these topics are well beyond the present scope. Nonetheless since the interaction lengths for other $v_{\|}, \lambda_{\rm wf}$ are generally much less than this maximum case, the phase bunching for the vast majority of particles is also much less, so that the neglect of wave/particle feedback is probably well justified at these input wave intensities.

3.2.3 Scattering Velocity Sensitivity and Linearity

Fig. 3.4 demonstrates two important scattering characteristics, namely 1) the rather sharp sensitivity of pitch angle deviation $\Delta\alpha_{\rm eq}$ (represented by $\max|\Delta\alpha_{\rm eq}|$) to particle velocity, and 2) the scattering linearity with whistler wave intensity, and by extension, the underlying lightning source strength.

Peak scattering velocity bandwidth. The example scattering trajectories given in the last section were run for a single ($v^*_{||,eq}$, $\lambda^*_{\rm wf}$) pair which gave maximal interaction length and maximal scattering (peak over η) over all ($v_{||,eq}$, $\lambda_{\rm wf}$) combinations. As $v_{||,eq}$ is varied while $\lambda_{\rm wf}$ is held constant, the quantity $\max|\Delta\alpha_{\rm eq}|$ vs. $v_{||,eq}$ exhibits a sharp peak about $v^*_{||,eq}$, as illustrated in the profiles shown in the series of stacked panels in Fig. 3.4a (left-column). In particular, in the top-most profile the arrows show the bandwidth in velocity for which the scattering is 10% of the peak value; here $v_{||,eq}$ varies by 4.9% about $v^*_{||,eq} = 231.6 \times 10^6$ m/s, emphasizing the need for precision in the simulation to accurately calculate the scattered pitch angle distribution. Note that these profiles represent the envelope of peak scattering; in general at each $v_{||,eq}$ the twelve particles are scattered within the envelope defined by a profile and its associated negative image (c.f. Fig. 3.3e).

Scattering linearity with lightning intensity. Fig. 3.4 demonstrates the linearity of $\Delta\alpha_{\rm eq}$ with lightning intensity E_{100} (through whistler wave intensity B^w_y), as indicated by the sequence of $\max|\Delta\alpha_{\rm eq}|$ vs. $v_{||,eq}$ profiles (stacked panels, left column) for different values of E_{100}, over the range of $1 \leq E_{100} \leq 50$ V/m (for $\lambda^*_{\rm wf}$=-12.5° along L=2.2). Note that for $E_{100} = 50$ V/m, for which the whistler intensity at $f = 5$ kHz is $B^w_y = 50$ pT, the peak scattering exceeds 2°.

The values of each peak "spike" from each panel (which correspond to $\max|\Delta\alpha_{\rm eq}|$ for this same value $v^*_{||,eq} = 231.6 \times 10^6$ m/s as before) are plotted as open circles in the right panel along with a linear regression fit. Although this linear relationship is not altogether unexpected, it is important to confirm since the flux scaling procedure of Chapter 4 requires that this property hold.

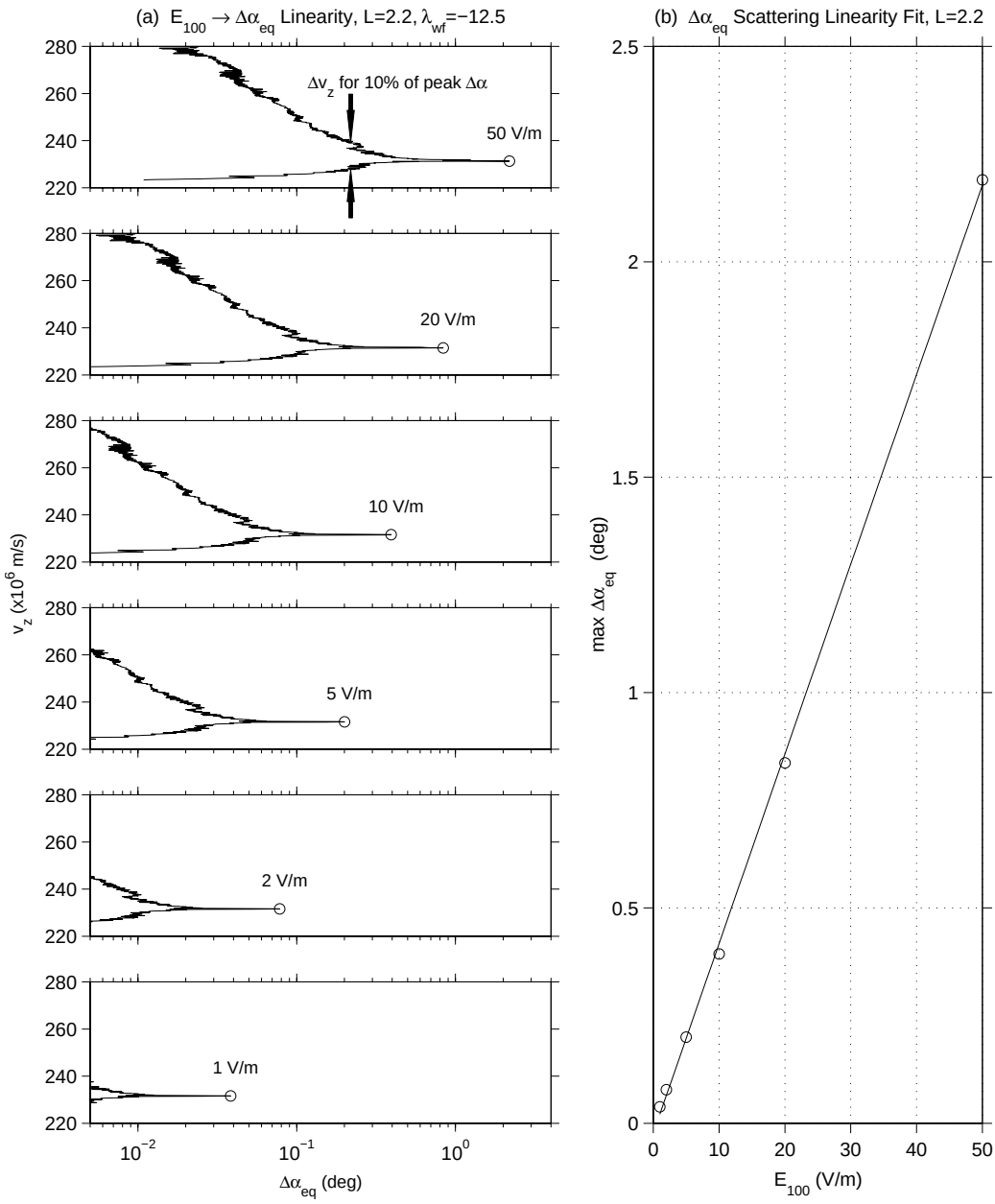

Figure 3.4: Scattering linearity with E_{100}.

3.2.4 Representative Signature Features

Fig. 3.5 shows representative precipitation signatures for two different lightning source strengths $E_{100} = 10$ V/m and $E_{100} = 20$ V/m (left and right columns, respectively) while all other parameters are identical for both cases. This figure serves both to illustrate certain detailed features in the scattering and precipitation E-t signatures, and to verify the linearity of the overall precipitation flux $\Phi(E,t)$ and $Q(t)$, which follows from the linearity in the scattered angles discussed previously.

This particular lightning source location $\lambda_s = 30°$ and field line $L = 2.2$ of interaction are selected as a combination for which the whistler wave field is projected most strongly to the region just south of the magnetic equator where the interaction lengths are longest, thereby giving the most favorable conditions for maximal scattering. In a forthcoming section the precise signatures for any given L-shell will be seen to depend on the specific cut made by that particular field line through the region of projected maximum whistler field intensities; nonetheless the basic spectral forms and features to large degree remain similar to this representative case. Here each panel in Fig. 3.5 will first be briefly described, and then important features will be discussed as they interrelate amongst the panels. For convenience when forthcoming comments apply equally to respective panels in the left and right columns, the particular figure row will be referred to collectively by its letter while omitting the column number (i.e. Fig. 3.5a refers to panels Fig. 3.5(a.1) and Fig. 3.5(a.2) together).

Fig. 3.5a (top) shows the primary resonance latitude $\lambda_{\rm res}$ where $\epsilon \to 0$ (for those particles which encounter multiple resonance regions along a trajectory, Fig. 3.5a indicates the average of such $\lambda_{\rm res}$ values), while Fig. 3.5b (second from top) shows the primary resonant frequency f seen by the particle, also where $\epsilon \to 0$. Fig. 3.5c (middle) shows the resulting peak scattering $\max|\Delta\alpha_{\rm eq}(E,t)|$ (peak over η_o, as previously indicated, e.g. Fig. 3.3e) now mapped over energy and time (similar to the manner in which $\Phi(E,t)$ is constructed, see Section 3.1); hereafter this quantity will be referred to simply as $\Delta\alpha_{\rm eq}(E,t)$, where the peak absolute operation is understood. For reference, in Figs. 3.5(a.1,b.1), contours corresponding to values at 10% of peak $\Delta\alpha_{\rm eq}$ taken from (c.1) are overlaid on the $\lambda_{\rm res}$ and f plots to indicate the locations and frequencies for which the largest scattering occurs. In other words, points within these contours are scattered to values which are in upper 90% range of all deflections. Here it is seen that these particles have experienced resonance near and beyond the magnetic equator. Fig. 3.5d (second from bottom) shows the resulting precipitation flux $\Phi(E,t)$ for the assumed phase-space density f_v as discussed in Section 3.1, while Fig. 3.5e (bottom) shows the integral energy flux $Q(t)$ (equation [3.2], with $E_{\rm th} = 0$). Comparing panels (e.1) and (e.2) the total precipitated flux $Q(t)$ is indeed seen to be linear in E_{100}, where the peak energy fluxes are $Q_{\rm pk} = \max Q(t) = 1.2$ and 2.4 milli-ergs/cm^2/s for $E_{100} = 10$ and 20 V/m respectively.

Signature feature details. Particular features in the energy-time signatures are discussed here in detail. Shown in Fig. 3.5(a.1) are dashed lines which indicate the manner in which the the concave down and concave up segments of the resonance curves of Fig. 3.2 map to lines in the E-t plane (note that at very high resolution, the concave down line is indeed straight as shown, while the concave up "line" is actually an arc which follows the lower boundary). These same lines are shown below in Figs. 3.5(c.1,c.2), where they are labeled as fast and slow E-t slopes (relative to each other), and where they are seen to correspond to the two branches of the slanted "Y"-shaped $\Delta\alpha_{\rm eq}(E,t)$ feature in the $\Delta\alpha_{\rm eq}(E,t)$ signature, most evident in (c.2). Note that the point at the crux of the "Y" indicated in Fig. 3.5(c.1) is also the location of the global peak $\Delta\alpha_{\rm eq}$ scattering for ($v^*_{||,eq}$, $\lambda^*_{\rm wf}$) shown previously in Fig. 3.3e. For reference, from (a.1) the responsible frequency for this peak $\Delta\alpha_{\rm eq}$ is midband near $f \sim 5$ kHz (also evident in Fig 3.3a).

The typically unequal emphasis of the two branches of the "Y" effectively create a breakpoint in the overall slope, shown most clearly in (c.2) (by virtue of the saturated color scale), such that for early times, the signature follows the faster slope, while for later times, the signature follows the slower slope (or arc). Since the fast slope is due to the concave down segments of the resonance curve leading edges, previously noted to be due to the non-zero wave normal angles, the presence of these two distinct slopes (whether on either side of the breakpoint or manifest as the two simultaneous upper branches of the "Y"), if measured by a particle detector, would confirm that the scattering in such case is due to obliquely propagating waves as opposed to strictly parallel propagating waves.

An important result is seen from comparison of the distinctly different spectral features in the pitch angle peak deviation $\Delta\alpha_{\rm eq}(E,t)$ (Fig. 3.5c) and the overall precipitation flux $\Phi(E,t)$ (Fig. 3.5d); specifically, the energy at which the peak pitch angle deflection occurs in (c.1) is different from the energy at which the maximum flux is seen in (d.1). This difference is due primarily to the assumed $1/v^6$ particle velocity dependence of the phase-space density f_v, which greatly emphasizes the lower energies in $\Phi(E,t)$, as greater fluxes from the vast majority of small pitch-angle deflections exceed the lesser fluxes from the minority of large pitch-angle deflections. While such fluxes can be substantial (the arrow in (d.1)), since they are associated with much smaller deflections they may in practice be difficult to detect as transient events above the background flux for a more realistic soft pitch angle distribution at the edge of the loss-cone (unless they themselves constitute such background flux!). Conversely, since the particles having largest deflections have the best chance to emerge from the background, if one were to introduce a pitch angle deflection threshold $\Delta\alpha^{\rm th}_{\rm eq}$ such that particle deflections beyond $\Delta\alpha^{\rm th}_{\rm eq}$ were considered while smaller deflections were screened out (e.g. by detector angular resolution or latitude of observation), then as $\Delta\alpha^{\rm th}_{\rm eq}$ is increased above zero the corresponding $\Phi(E,t)$ so calculated or measured would transition from the more softly defined signature of (d.2) to the more sharply defined "Y"-shaped feature of $\Delta\alpha_{\rm eq}(E,t)$ of (c.2).

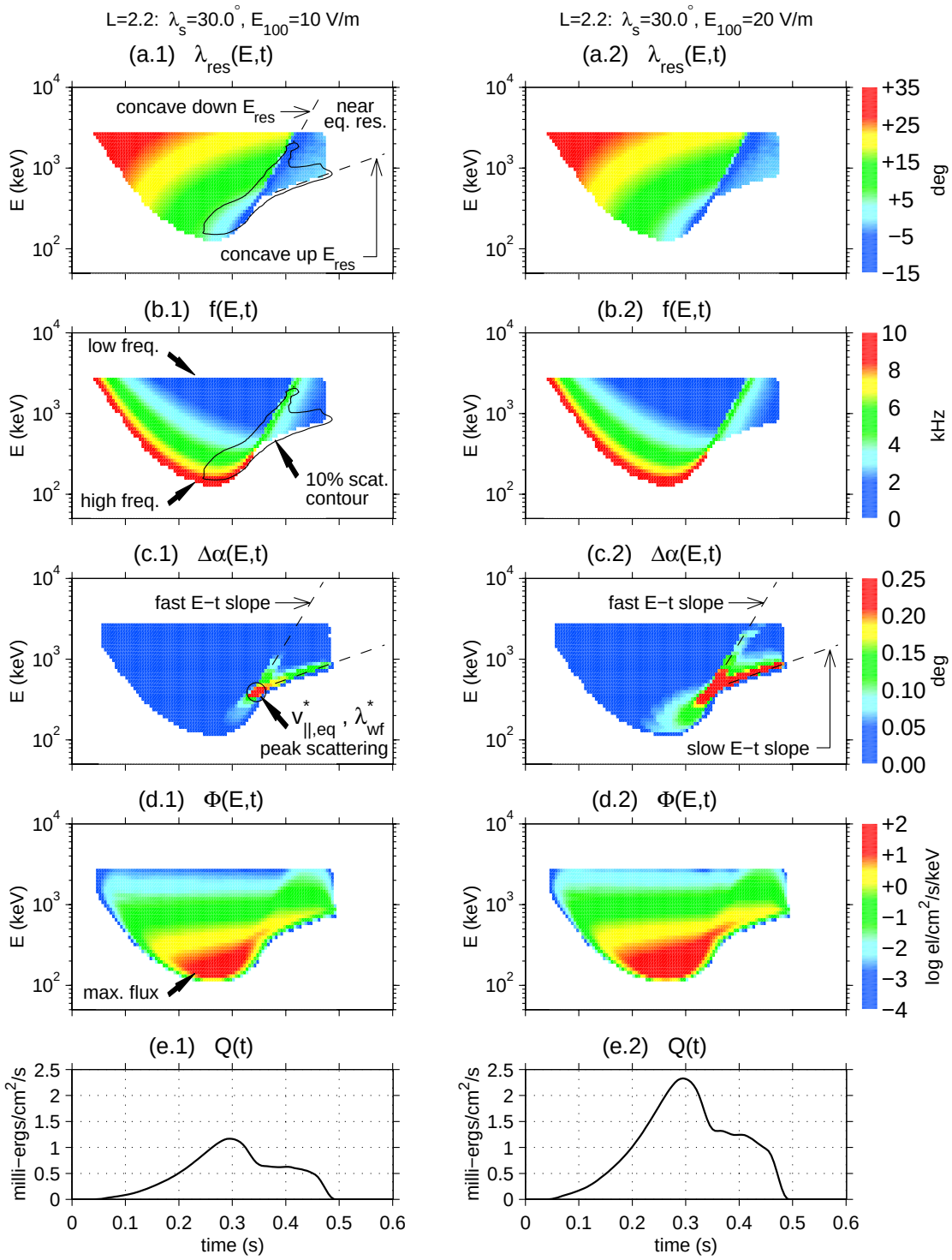

Figure 3.5: Detailed precipitation signatures and features for $\lambda_s = 30°$. Left and right columns are for lightning $E_{100} = 10$ and $E_{100} = 20$ V/m respectively. Individual panels are discussed in the text.

3.3 Precipitation Signature Case Studies

In general the scattering calculations are carried out for selected L-shells at spacing $\Delta L = 0.2$ over the range $L = 1.8$ to $L = 4.0$, for each lightning source considered in Chapter 2; here those deemed most interesting are presented. With the basic signature spectral forms and features now identified in the previous section, it is of interest to explore the manner in which these signatures vary depending on the particular "cut" which a field-line makes through the spatially-varying whistler wave fields.

What follows are a series of figures each of which shows, for a given lightning latitude λ_s, the $\Delta\alpha_{\rm eq}(E,t)$ and $\Phi(E,t)$ signatures and corresponding electron number flux $N(t)$ and precipitation energy flux $Q(t)$ at the foot of four adjacent L-shells which sample the region of maximum wave intensities. The detailed precipitation energy-time signatures at the foot of particular L-shells are seen to manifest specific E-t slopes which vary in a systematic way depending on whether the maximum wave intensities are encountered relatively early or relatively late along the particle trajectories.

3.3.1 Lightning Source at $\lambda_s = 30°$.

Fig. 3.6 shows the case for lightning source with $E_{100} = 10$ V/m at magnetic latitude $\lambda_s = 30°$. The top row shows $\Delta\alpha_{\rm eq}(E,t)$, second row, $\Phi(E,t)$, third row, $N(t)$ and lower row $Q(t)$, while for reference, the single bottom panel shows the projected magnetosphere illumination pattern for this lighting source latitude and the trace of each field line through the whistler wave fields.

Note that the scattering signatures detailed in the previous section (Fig. 3.5) for $L = 2.0$ also appear here in the second column from the left. Then over the range of L-values shown, the variation in signature E-t slope is plainly evident. Specifically, with reference to the L-shell of maximum equatorial wave intensity ($L^* \sim 2.1$ for this representative frequency $f = 5$ kHz), at higher relative L-shells the strong wave intensities south of the magnetic equator combine with the longer interaction lengths along these higher field lines to give the upward sloping $\Delta\alpha_{\rm eq}(E,t)$ and $\Phi(E,t)$ signatures detailed previously, while at lower relative L-shells the particles encounter increasingly stronger wave intensities as they approach the lightning source, compensating somewhat for the generally shorter interaction lengths to give more *downward* sloping E-t signatures (e.g. at $L = 1.8$).

Note here that of the four selected L-values, the maximum *energy* flux $Q(t)$ occurs for $L = 2.0$, even though the maximum electron *number* flux $N(t)$ occurs for $L = 2.4$. This result stresses the importance of the assumption regarding spectral hardness $f_v \sim 1/v^6$ in computing N and Q.

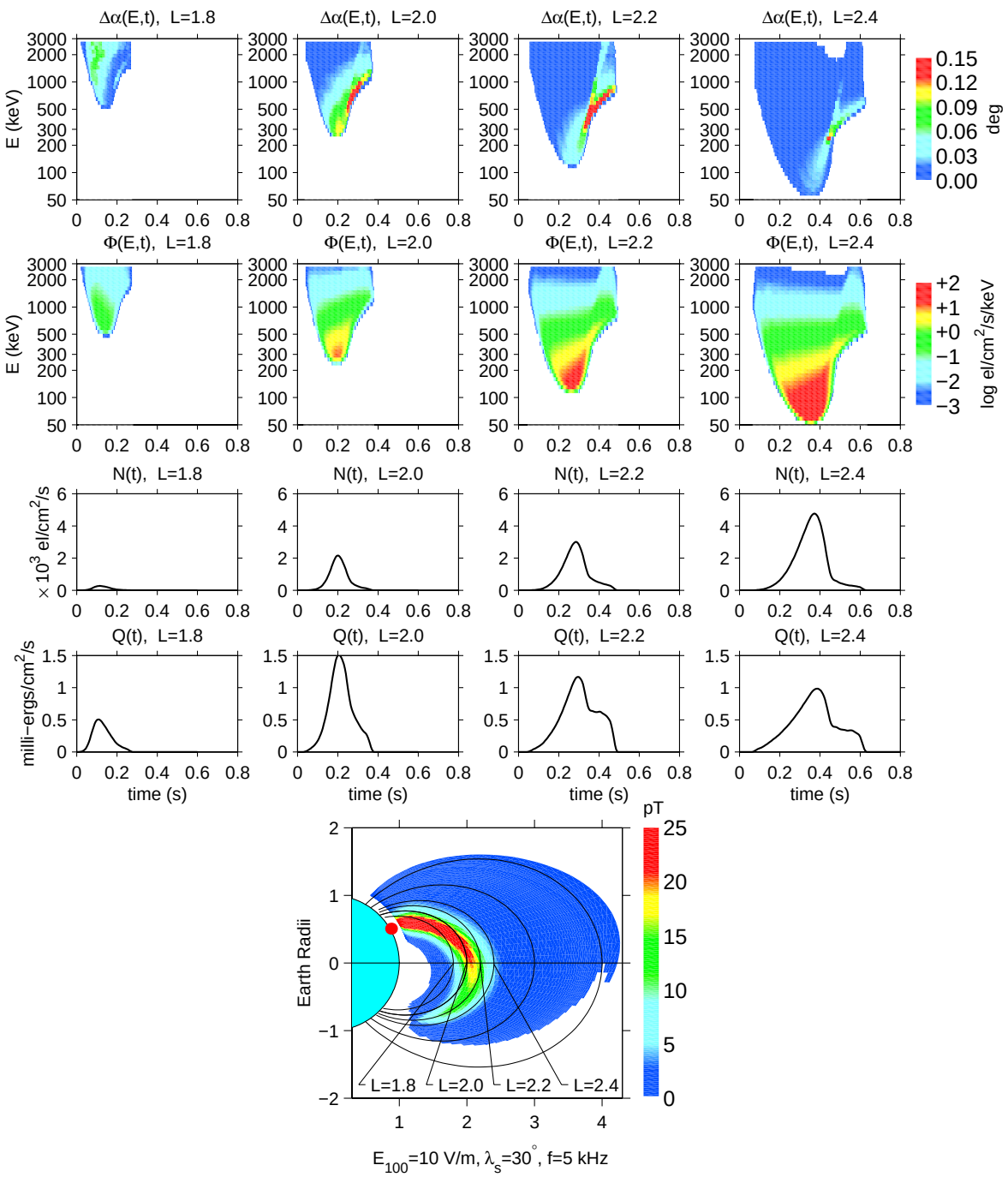

Figure 3.6: Precipitation signatures at the foot of four L-shells sampling the region of maximum wave intensity for lightning source at $\lambda_s = 30°$. Top to bottom: scattering $\Delta\alpha_{\mathrm{eq}}(E,t)$, flux $\Phi(E,t)$, electron flux $N(t)$ and energy flux $Q(t)$.

3.3.2 Lightning Source at $\lambda_s = 40°$.

Figure 3.7 shows the case for $\lambda_s = 40°$. Here the variation of the E-t slope with L is even more pronounced, with the case for $L = 2.8$ showing an approximate balance between upward and downward slopes. Note also the clear breakpoint between fast and slow E-t slope for $L = 3.0$. Here even at the lowest of these four L-shells, the peak $\Delta\alpha_{\mathrm{eq}}(E, t)$ exceeds 0.2°. Note that by the linearity property indicated in Section 3.2.3, for E_{100} ten times more intense at 100 V/m, a good fraction of particles would be scattered by as much as 2°, arriving at the upper atmosphere as early as 300 ms after the lightning discharge. for $L \leq 2.6$.

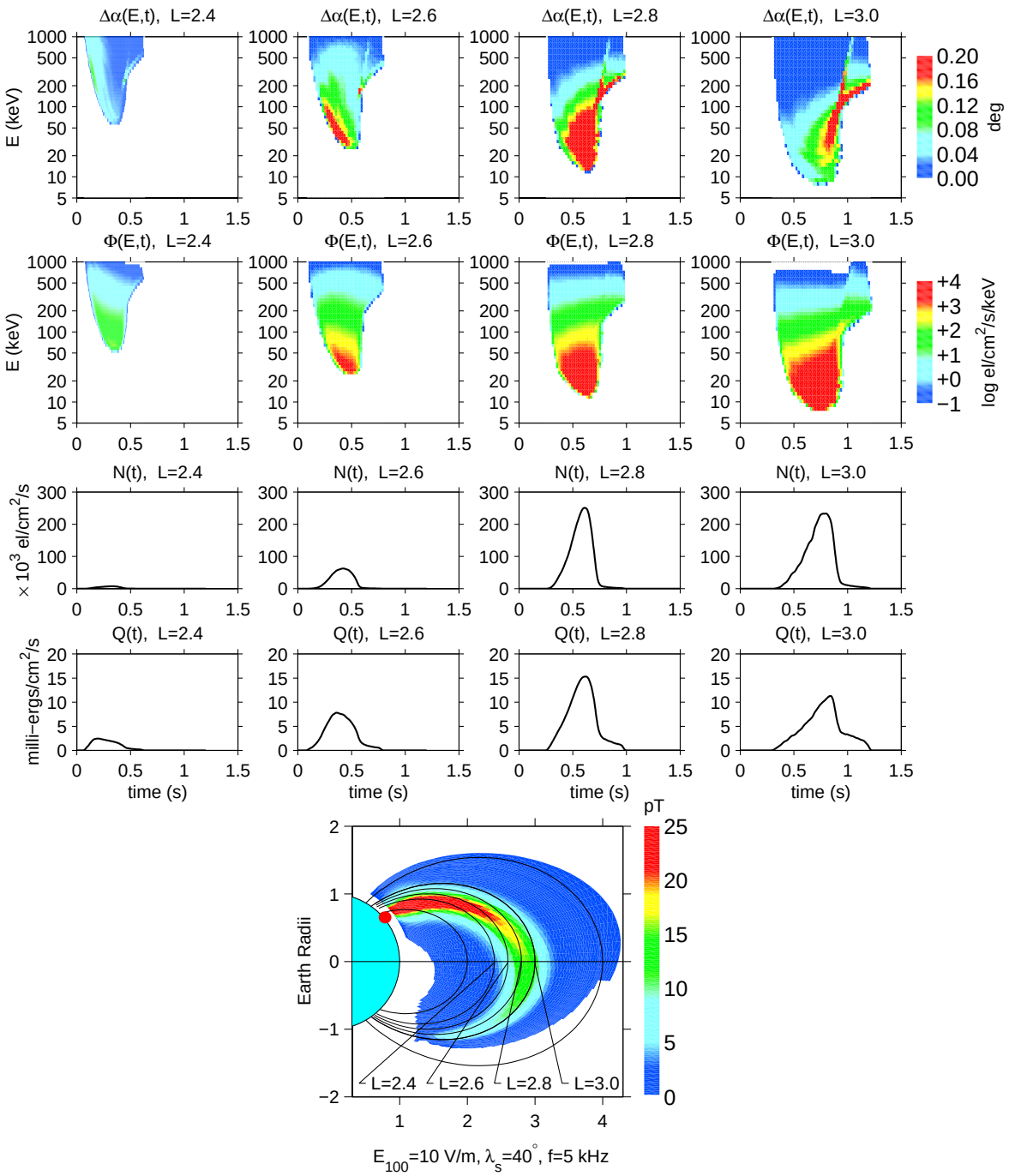

Figure 3.7: Precipitation signatures at the foot of four L-shells sampling the region of maximum wave intensity for lightning source at $\lambda_s = 40°$. Format same as for previous figure.

3.3.3 Lightning Source at $\lambda_s = 50°$.

Fig. 3.8 shows the case for $\lambda_s = 50°$. Note the tremendous total flux which is precipitated in response to this high-latitude lightning discharge, exceeding 10^5 el/cm^2/cm/s over (at least) $3.4 \leq L \leq 4.0$. Note that the peak energy fluxes are on the order of several tens of milli-ergs/cm^2/s, comparable to weak auroral fluxes, albeit persisting for only a short time after the discharge. Note also that this case shows the overall greatest particle deflections $\Delta\alpha_{\mathrm{eq}}$ for any source location λ_s. Since the projected maximum whistler wave intensities are approximately equivalent to those which occur (along different L-shells) for other lightning source latitudes, this effect is primarily due to the very long interaction lengths (i.e. in km) and generally lower resonant particle momenta at these high L-shells. This result suggests that of all factors considered, the variation of interaction length with L-value may in fact be the most dominant factor in determining which L-shells are most affected on average for a realistic distribution of lightning source latitudes.

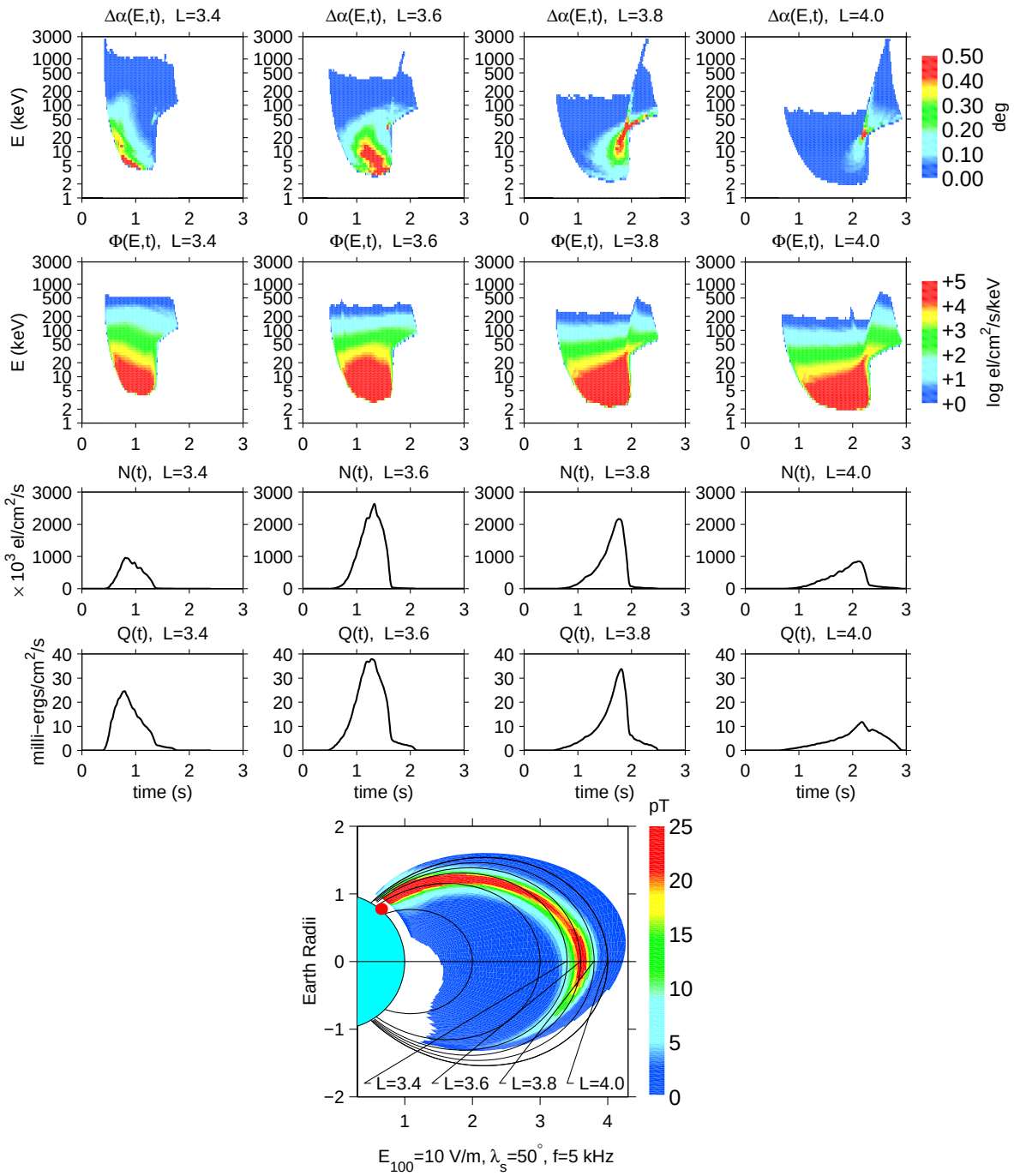

Figure 3.8: Precipitation signatures at the foot of four L-shells sampling the region of maximum wave intensity for lightning source at λ_s=50°. Format same as for previous figure.

3.3.4 Summary over L and λ_s

Fig. 3.9 presents $\Phi(E,t)$ and $Q(t)$ signatures over $L=2$, 3 and 4 for lightning locations $\lambda_s = 20°$, 30°, 40° and 50° on common axes scales for ready comparison. Note the sensitivity of the L-shell of maximum energy flux to lightning source latitude λ_s; specifically, the energy flux Q at $L = 2$ peaks for $\lambda_s = 30°$, the flux at $L = 3$ peaks for $\lambda_s = 40°$ and the flux at $L = 4$ peaks for $\lambda_s = 50°$.

Note also the large variation in precipitation onset delay time with L-value. In particular, the arrival of the precipitation pulse (here at ionospheric altitude $h_p = 100$ km) for lower L-shells always precedes those for higher L-shells and higher latitudes. This earlier arrival at low L-shells is due to both the shorter propagation paths for the wave and the faster velocities of the generally higher resonant energy particles. Conversely, the later arrival at high L-shells is due to the longer wave paths and slower velocities of the generally lower resonant energy particles. Note that since the wave propagation time is governed by the thermal plasma density supporting the whistler-mode waves, and that in addition this density also affects the resonance condition (equation [1.8]), the flux pulse arrival time at a given L-shell and especially the relative timing over a range of L-shells reflects the state of the magnetosphere, while the relative flux intensity emphasis vs. L-shell (or equivalently, precipitation latitude) reflects the particular lightning source latitude for a given event.

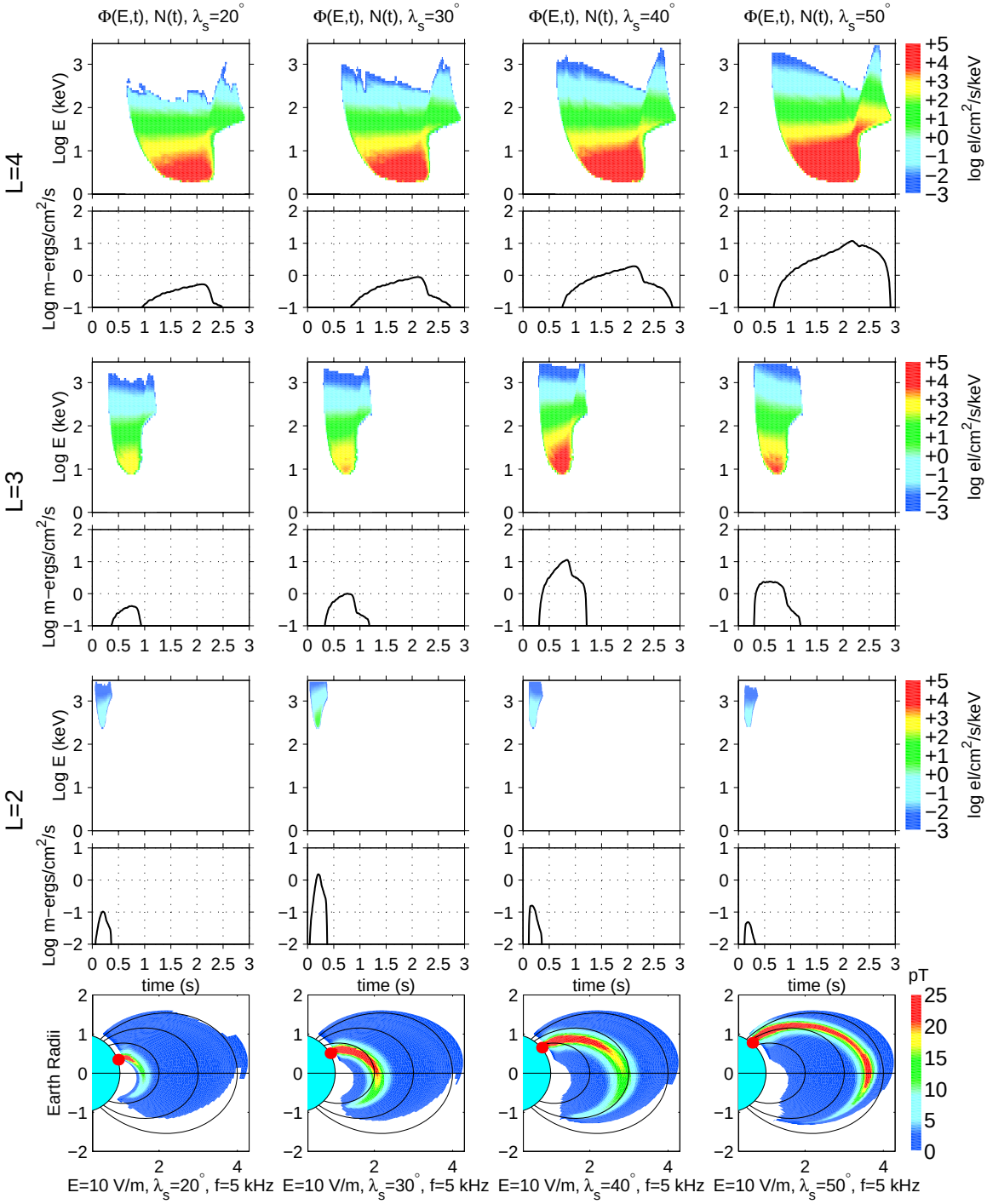

Figure 3.9: Precipitation E-t summary mosaic.

This page intentionally left blank.

Chapter 4

Precipitation Hotspots

"...see if I will not throw open the floodgates of heaven... [Mal. 3:10]"

This chapter builds upon the results of Chapter 3 to determine the spatial extent at the ionosphere of the precipitation energy flux footprints, or "hotspots," induced by a given lightning discharge. Results are presented for two representative lightning source locations over several integral energy ranges $E > E_{\rm th}$ in calculating the energy flux Q (see equation [3.2]), to show the general variability of the spatial and temporal characteristics with particle energy. Fixed-time summary plots are then presented for all lightning locations $\lambda_s = 20°$, $30°$, $40°$ and $50°$, showing 1) hotspot instantaneous spatial peak flux; 2) time-integrated spatial energy flux (fluence); and 3) precipitated spatial electron number density. These results are further summarized in the form of longitude-integrated profiles giving precipitation energy flux vs. latitude and precipitated electron number flux vs. L-shell, which together show that the greatest electron fluxes precipitated by lightning occur at higher latitudes and L-shells. Altogether these results suggest that lightning-generated oblique whistler induced precipitation is an important energetic electron loss mechanism over the L-shell range $1.8 \leq L \leq 4.0$.

4.1 Precipitation Hotspot Construction

In Chapter 3 the precipitation energy-time signatures $\Phi(E,t)$ and associated energy and number flux-time profiles $Q(t)$ and $N(t)$ were calculated for selected L-shells over the range $L=1.8$ to $L=4.0$ at spacing $\Delta L=0.2$, contained in the reference meridian $\delta_o = 0.9°$. In this Chapter these quantities are denoted $\Phi_L^{\delta_o}$, $Q_L^{\delta_o}$ and $N_L^{\delta_o}$ respectively, where the superscript/subscript notation for L and δ_o is used to indicate calculation at these explicit points, and where the E and t dependence is understood. In order to determine the flux-time profiles over an entire ionospheric footprint region it is necessary to specify the general set Φ_L^{δ}, Q_L^{δ} and N_L^{δ} for meridional planes at $|\delta| < 0.9°$ and $|\delta| > 0.9°$. In principle such profiles for $|\delta| <> 0.9°$ may be determined by explicit calculation as in Chapter 3 for properly adjusted lightning radiated VLF wave input power along each new meridian (see Fig. 2.2), however it turns out that it is both possible and expedient to instead use an extrapolation technique which scales each $\Phi_L^{\delta_o}$ already calculated for $\delta_o = 0.9°$ in an appropriate manner to provide Φ_L^{δ} for any given $\delta \neq 0.9$, from which Q_L^{δ} and N_L^{δ} are subsequently calculated, as detailed next.

4.1.1 Longitude Extrapolation

In Chapter 3 the precipitation flux signatures were shown to be linear in lightning intensity E_{100}, and equivalently, the corresponding whistler wave intensity B_y^w (Fig. 3.4). This property also implies that in general the precipitation flux levels vary in linear proportion to the change in whistler wave intensity which occurs as the meridional cut δ through the input wave illumination pattern (see Fig. 2.9) is changed. However since for the oblique waves considered herein a given field line is illuminated by an *ensemble* of frequency-dependent ray paths originating over a range of injection latitudes λ_i (see Fig. 2.4), as the longitude δ is varied and the input intensity for each ray varies by a different amount depending on its associated λ_i, the projected intensity profile over the field line varies in a non-simple way. Thus the precipitation flux for any two field lines sharing the same L-value but different longitudes δ are *not* related by a single scalar value, but instead depend upon the projected illumination pattern which varies with both frequency f and injection latitude λ_i.

It turns out the best procedure is to scale *each energy-time cell* comprising $\Phi_L^{\delta_o}(E,t)$ by the relative wave intensity indicated by the change in dipole illumination pattern as δ is varied at the specific ray injection latitude λ_i, for that oblique ray path, for that frequency f known to be primarily responsible for resonance scattering for that cell.[1] This scaling technique is illustrated in Fig. 4.1 for a representative case at $\delta = 0°$, 1.8°, 3.6°, 9.0° scaled from $\delta_o = 0.9°$, for L=2.2. Here Fig. 4.1f (lower-left) shows the lightning illumination pattern for λ_s =30° taken from Chapter 2 (shown over a larger region). The reference flux $\Phi_L^{\delta_o}(E,t)$ and the corresponding $Q_L^{\delta_o}(t)$ for $\delta_o = 0.9°$ calculated in Chapter 3 are shown above in Fig. 4.1b. The remaining $\Phi_L^{\delta}(E,t)$ are then scaled from this reference in the manner indicated above, with the corresponding $Q_L^{\delta}(t)$ found via equation [3.2]. Note that the choice of non-zero $\delta_o = 0.9°$ as the reference longitude precludes those wave intensity values which become zero within the dipole pattern null (along central meridian, i.e. $\delta = 0°$) from ever entering the intensity ratio denominator. To verify the accuracy of this procedure, the "+" symbols shown along each scaled $Q_L^{\delta}(t)$ curve indicate values for the exact (non-scaled) scattering calculation for these δ values. The agreement is excellent, validating the extrapolation technique.

4.1.2 L-shell to Latitude Projection

It is recalled from Section 3.1 that for a given precipitation altitude h_p, a given L-value maps to the precipitation latitude $L \rightarrow \lambda_p$ through the relation $\cos^2(\lambda_p) = (1/L)\,(R_e + h_p)/R_e$, which in turn implies the projection $Q_L^{\delta} \rightarrow Q_{\lambda_p}^{\delta}$. More generally, in the sections to follow this mapping is applied for Q_L^{δ} over all L and δ and further interpolated onto a finely-spaced latitude $\times$ longitude grid to obtain $Q(\lambda_p, \delta, t)$, where this notation denotes evaluation over essentially continuous values for latitude, longitude and time. Also by this same $L \rightarrow \lambda_p$ mapping, for convenience in the discussion to follow the resulting energy flux is referred to interchangeably as $Q(L, \delta, t)$ or $Q(\lambda_p, \delta, t)$.

[1] Note that this scaling technique also would allow for an alternate flux spectral index $f_v \sim 1/v^n$ to be applied.

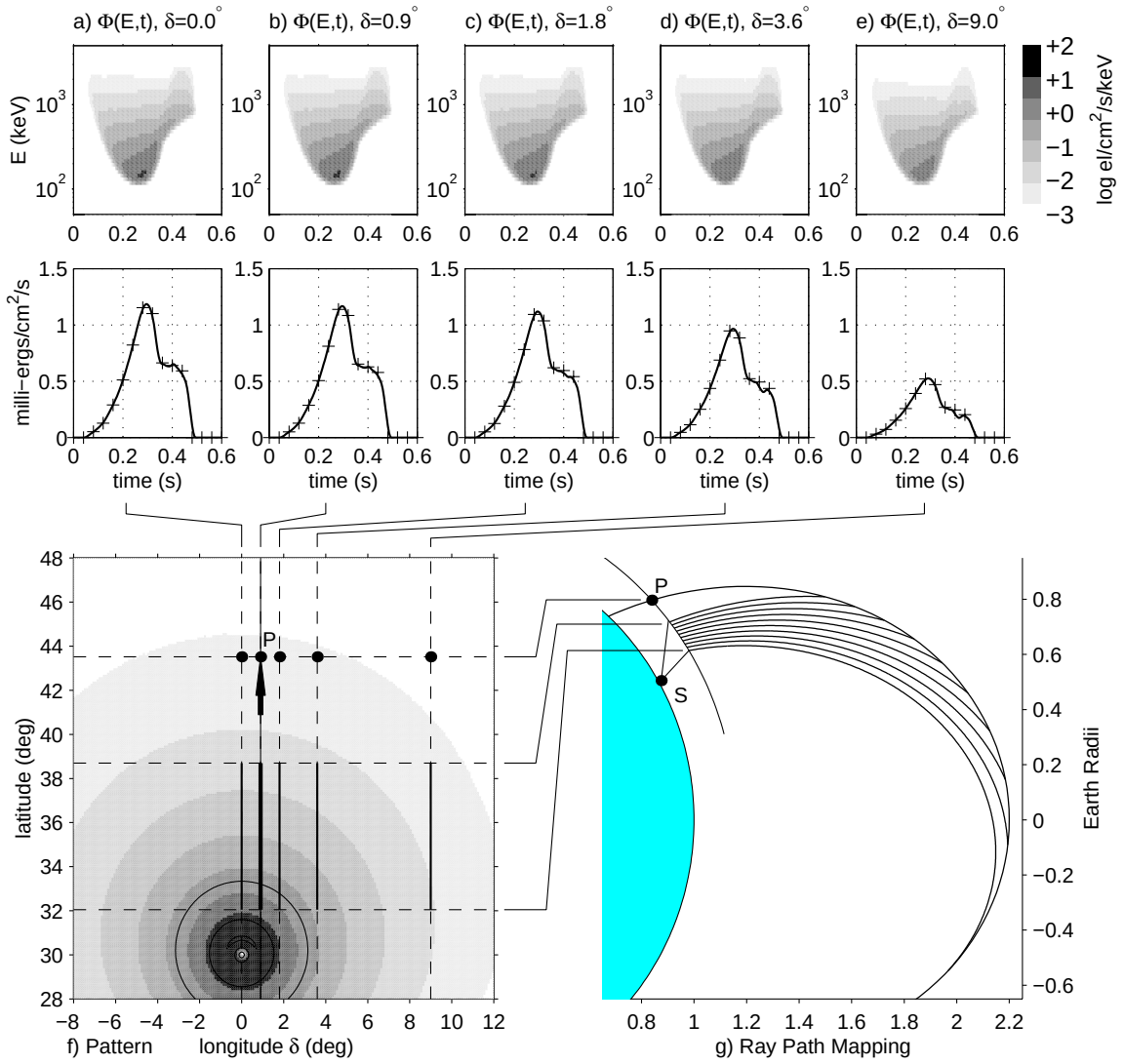

Figure 4.1: Longitudinal extrapolation technique. Flux $\Phi_L^{\delta_o}(E,t)$ shown in (b) arriving at point P at the foot of $L=2$ for $\delta_o=0.9°$is calculated exactly and subsequently scaled for $\delta = 0°$, $1.8°$, $3.6°$, $9.0°$ according to the wave intensity ratio over longitude at the injection latitude λ_i of that ray which best matches the resonance condition for each E-t cell in $\Phi_L^{\delta_o}(E,t)$ to produce each respective $\Phi_L^{\delta}(E,t)$ shown in (a) and (c) thru (e) and the corresponding $Q_L^{\delta}(t)$ (solid line profiles) shown below. Plus "+" symbols on the $Q_L^{\delta}(t)$ profiles indicate exact calculations (for these test cases) which validate the extrapolation technique.

4.2 Precipitation Hotspot Time Sequences

This section presents time sequences of the precipitation hotspots over a wide geographic region for lightning source locations $\lambda_s = 30°$ and $\lambda_s = 40°$, each over energy ranges $E > 0$,[2] $E > 100$ keV and $E > 1$ MeV. These sequences show the development of the precipitation hotspot over space and time and in particular its substantial displacement poleward relative to the location of the causative lightning flash. The reason for including several cases for non-zero minimum energy threshold $E > E_{\rm th}$ are two-fold. First, most any measurement to which these calculations might be compared will be for some non-zero value of minimum detectable energy, and second, since significant transient perturbations to the lower ionosphere (especially at altitudes < 90 km accessible to measurement using VLF remote sensing techniques [*Inan et al.*, 1990]) are thought to be caused primarily by electrons in the range 100 keV $\leq E \leq$ 1 MeV, it is of special interest to isolate the spatial location of the peak fluxes for these higher energies in a manner which is not obscured by the otherwise tremendous flux of lower energy precipitating electrons.

4.2.1 Lightning Source at $\lambda_s = 30°$

A common format is used for all hotspot time sequence figures, explained in detail here for this first case. Fig. 4.2a (top-left) shows, for reference, the magnetospheric whistler wave intensity (for the midband frequency $f = 5$ kHz) for the assumed lightning source at a magnetic latitude $\lambda_s = 30°$. Fig. 4.2b (top-middle) shows an overlay of the individual precipitation energy flux profiles $Q_L^\delta(t)$ in the central meridian $\delta = 0$ for the complete set of L-shells over the range $1.8 \leq L \leq 4.0$ at spacing $\Delta L = 0.2$. Here the highest peak flux occurs at $L = 2.0$ due to the particularly intense wave fields along this L-shell in combination with the general trend towards higher resonant energies for lower L-shells. Note however that for $L > 2.0$ this particular case exhibits the quite remarkable property that nearly all $Q_L^0(t)$ flux profiles have the same peak value of 1 milli-erg/cm^2/s; specifically this result indicates that at higher L-shells the greater flux of predominantly lower energy electrons deposits the same peak energy flux as does the lesser flux of predominantly higher energy electrons at lower L-shells (c.f. Chapter 3), exclusive of $L = 2.0$. This result is also quite astonishing considering the much reduced magnetospheric whistler intensities ($B_y^w < 5$ pT) over, for example, $L = 3$ to 4 as compared with, for example, $L = 2.2$ ($B_y^w \sim 10$ pT), emphasizing once again the importance of the much longer interaction lengths at higher L-shells.

Fig. 4.2c (top-right) shows (on a logarithmic color scale) the energy flux profiles given in the previous panel now interpolated over L-shell, with L-value becoming the y-axis. Essentially this panel shows $Q(L, \delta = 0, t)$ or equivalently, $Q(\lambda_p, \delta = 0, t)$ by the now implicit $L \to \lambda_p$ mapping. Note that because of the fairly substantial change in Q_L^δ onset delay and temporal profile which

[2] Note that from Fig. 3.8 the lowest resonant particle energy is always greater than 1 keV; thus $E > 0$ and e.g. $E > 1$ keV would yield the same result in all cases.

occurs with each $\Delta L = 0.2$ increment (as seen in Fig. 4.2b), a sophisticated interpolation technique is required to smoothly blend between successive Q_L^δ profiles at intermediate L-shell values.

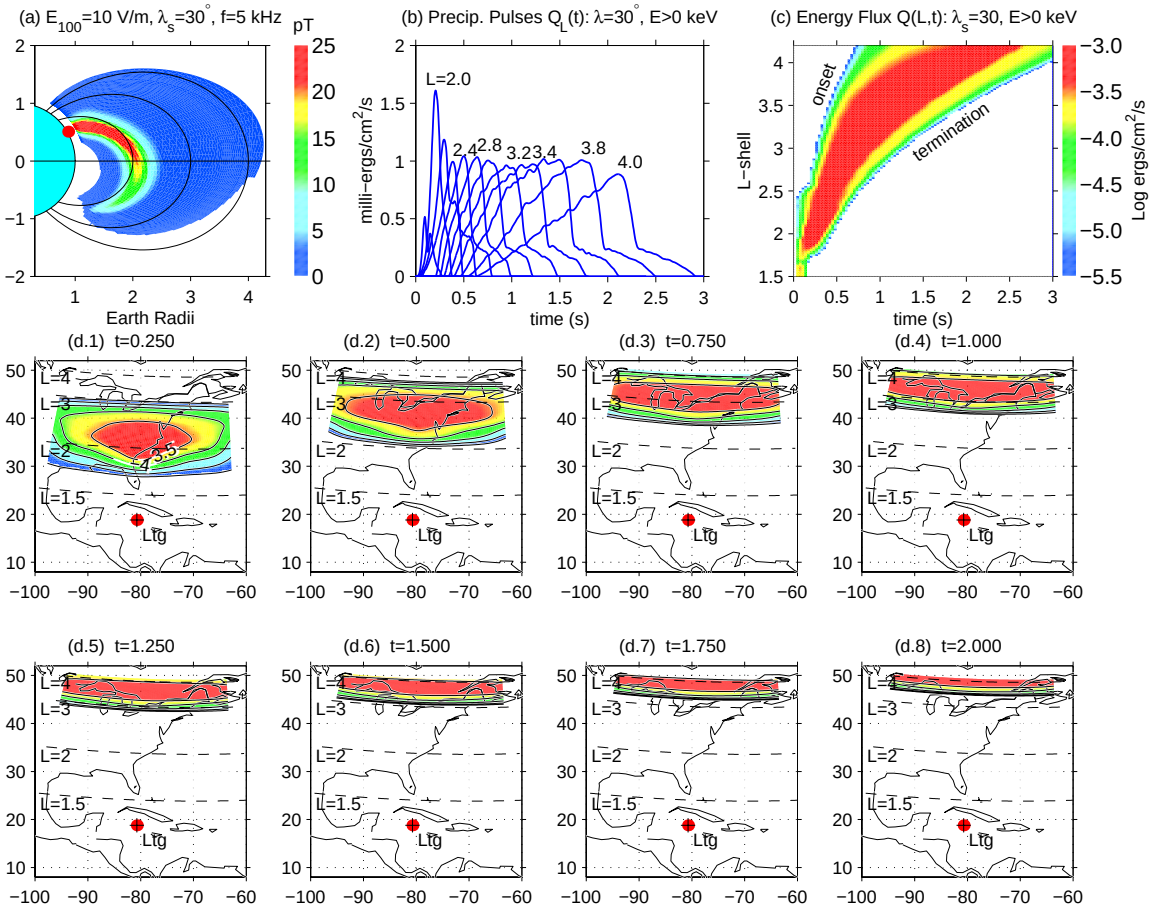

Figure 4.2: Precipitation hotspot time sequence for λ_s=30°, all $E > 0$. Explanation of plot panels is given in the text.

In Fig. 4.2c the L vs. time profile of the flux onset, flux peak and flux termination edge are immediately evident from the upward sloping form with time. Note that the blending technique mentioned previously produces very smooth L-shell vs. time (L-t) behavior for the flux onset edge, peak flux "ridge" and flux termination edge, even though there is significant incremental delay between individual $Q_L(t)$ profiles (i.e. $L = 3.8$ and $L = 4.0$ in the middle panel). Here the red-colored flux "ridge" defined by $Q > 10^{-3.5} \simeq 0.32$ milli-erg/cm^2/s (a somewhat arbitrary value) begins at $L \sim 1.8$ and $t \sim 0.1$ s for duration ~ 0.25 s, and subsequently exhibits an initially linear L-t onset edge up to about $L \sim 3.3$ at $t \sim 0.5$ s, then breaking to a gentler arch, reaching $L = 4$ at $t \sim 1.2$ s, where it persists at this level for duration ~ 1.2 s. Note that the very earliest onset and the very latest termination times are several tenths of a second prior and subsequent to this peak ridge (respectively), while the flux values at these extreme times are up to several orders of magnitude less the peak, and hence, may not be detectable above background.

Note that this flux-time plot $Q(L, \delta = 0, t)$ succinctly captures all the essential characteristics which define a precipitation hotspot. From the monotonic increase in precipitation onset time with increasing L-shell and thus with increasing latitude λ_p, if these precipitation flux-time profiles were to be viewed simultaneously at all latitudes λ_p at ionospheric altitude (for example with a satellite-imager or with an all-sky camera) the resulting precipitation burst will appear to move rapidly poleward with time. This realization suggests a robust and readily testable criteria to assess oblique-mode precipitation which (in this one regard) should not be sensitive to lightning location or strength nor specific energetic particle flux distribution – namely, the precipitation arrival time vs. latitude, which may be denoted $t_p(\lambda_i)$. Note however that while the *timing* of the flux-latitude profile $t_p(\lambda_i)$ is indeed determined solely by the combination of wave propagation and resonant particle transit time (as indicated in Section 3.3.4), the necessary variation of precipitation flux *intensity* with lightning source strength E_{100} and latitude λ_s may lead to *apparent* variations in onset timing given any specific detectability threshold.

Figs. 4.2(d.1) thru (d.8) (lower two rows) show the temporal development at time steps $\Delta t = 1/4$ s of the spatial precipitation footprint or "hotspot" projected onto geographic latitude and longitude coordinates over the Eastern United States, for the indicated lightning source latitude of $\lambda_s = 30°$ with source longitude chosen to be near the geographic longitude of the tip of Florida. As a practical matter the hotspots are first developed in magnetic dipole coordinates (δ, λ_p) and then projected to geographic latitude $\times$ longitude coordinates (which are not assigned any particular variable names). Here the color scale in (d.1-8) is the same as for the L vs. time profile in panel (c) (top-right). Note that for this longitude the mapping from magnetic dipole coordinates to geographic coordinates has the effect of subtracting $\sim 12°$ (the approximate dipole axis tilt) from the lightning magnetic latitude for the chosen longitude, so that this source at $\lambda_s = 30°$ appears at a geographic latitude of $\sim 18°$.

The first time frame (d.1) at t=0.250 s is representative of the earliest arrival of significant energy flux (~ 1 milli-erg/cm^2/s); here at its widest points the hotspot already extends $\sim 20°$ in longitude

and $\sim 8°$ in latitude, and is centered at $L \sim 2.2$ or $\sim 36°$ geographic latitude (at $h = 100$ km altitude), or some 18° *poleward* of the causative lightning discharge. This poleward displacement arises from the significant cross-L-shell propagation of the oblique whistler waves (see Fig. 2.4 in Chapter 2), from injection latitude to the magnetic equator, where the most significant scattering takes place (Chapter 3). By the next frame (d.2) at t=0.500 s the hotspot center has moved further poleward to $\sim 41°$, and has increased in longitudinal width to nearly 30°. The remaining frames (d.3-8) show that significant levels of flux continue to precipitate for up to 3 s, finally forming a thin band near 50° geographic latitude (from the L-shell convergence), having width at least as wide as the extrapolation limit of 36°.

Precipitation at energies $E = 100$ keV. Fig. 4.3 shows hotspot time slices for this same lightning source at $\lambda_s = 30°$ but for energies $E > 100$ keV. Note that for this lightning location the peak flux is centered generally about L=2.2, consistent with the centroid of the maximum projected whistler intensities near the magnetic equator. The lower two rows show the sequence of frames for $0 \leq t < 1$ s at $\Delta t = 1/8$ s increments. Here at t=1/8 s the most intense region of the spot first appears below L=2.0, or some ∼33°geographic latitude, moving poleward and beyond, passing L=2.2 at t=1/4 s and reaching L=2.5 before settling to lower values for $t > 1/2$ s.

Precipitation at energies $E > 1$ MeV. Fig. 4.4 shows the hotspot time sequence for the same lighting source as the previous cases but for $E > 1$ MeV and with Δt=50 ms. Here the maximal flux for these higher energies is centered at slightly lower $L \sim 2$, covers a smaller range of L, and diminishes by $t \sim 1/2$ s, compared with ~ 1 s for $E > 100$ keV seen previously. In the time slice frames the overall size of the hotspot peak is generally smaller, especially in longitudinal width; the generally more circular aspect-ratio for $t < 0.2$ s reflects the dipole pattern symmetry more closely, as these early particles experienced resonance northward of the magnetic equator and "see" a tighter dipole pattern (c.f whistler spatial intensity projection, top right). Finally, note that for higher L-shells there is much less effect at later times as compared with the previous cases which include the lower energies.

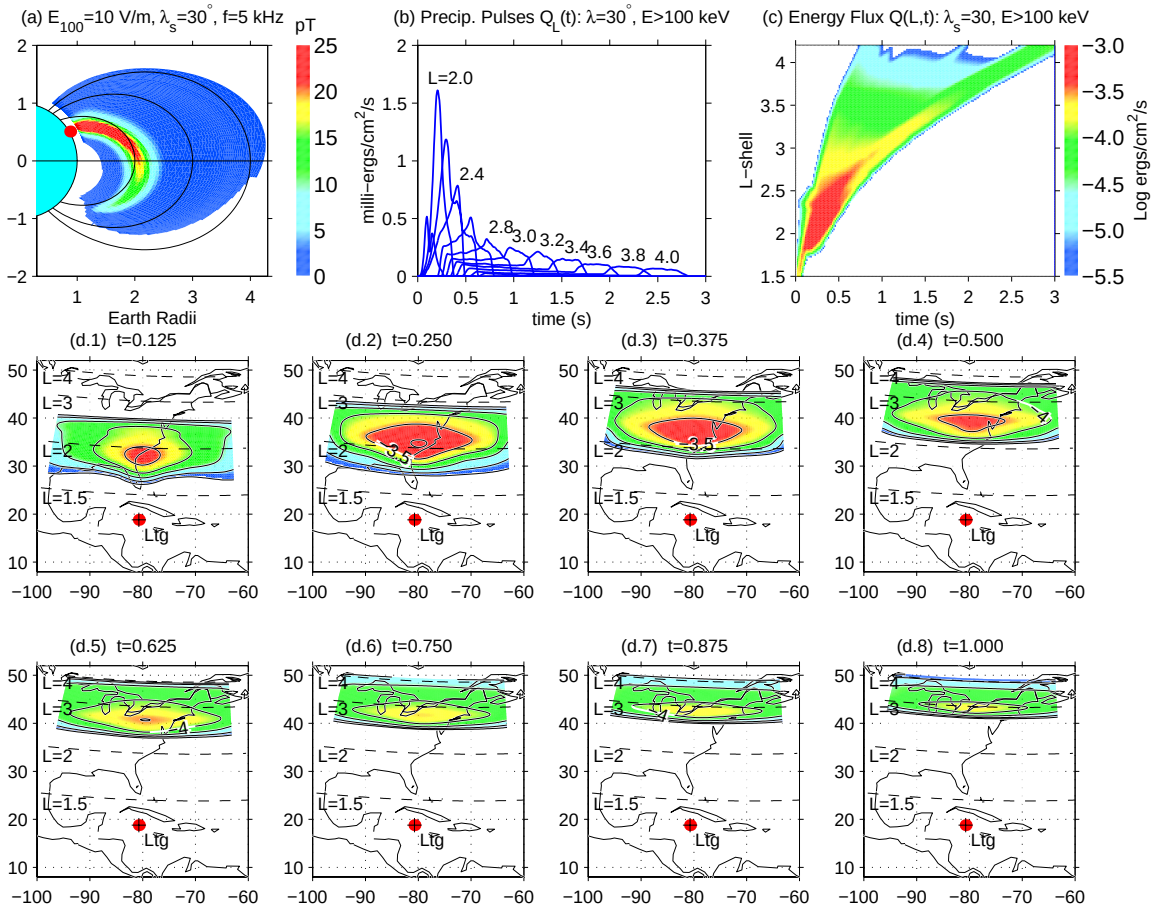

Figure 4.3: Precipitation hotspot time sequence for $\lambda_s = 30°$, $E > 100$ keV.

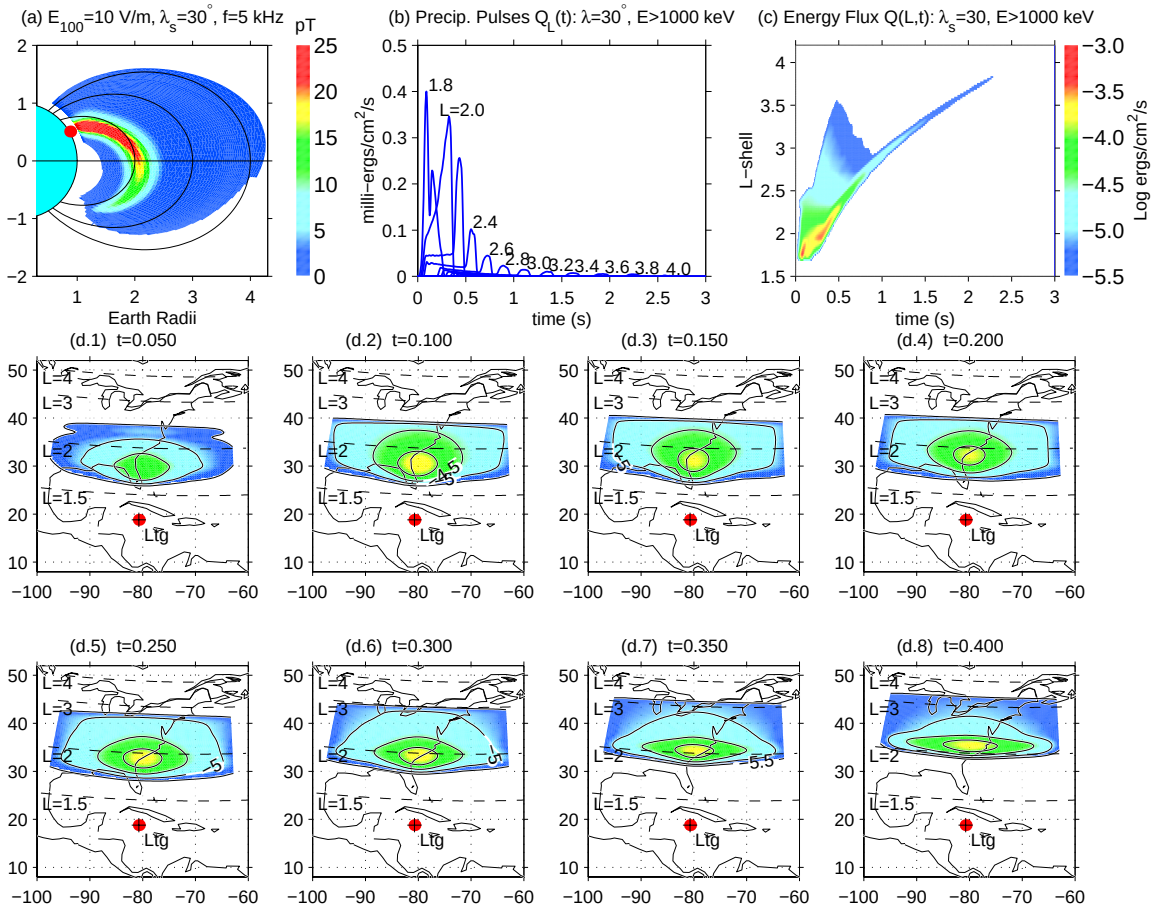

Figure 4.4: Precipitation hotspot time sequence for $\lambda_s = 30°$, $E > 1$ MeV.

4.2.2 Lightning Source at $\lambda_s = 40°$

Figs. 4.5, 4.6 and 4.7 shows hotspot time slices in the same manner as previously for energy ranges $E > 0$, $E > 100$ keV and $E > 1$ MeV now for a lightning source at $\lambda_s = 40°$. Here the greater spatially-projected magnetospheric wave intensities at higher L-shells combine with the generally longer interaction lengths along these field lines to markedly increase the precipitation flux intensity, spatial extent and duration as compared with the previous case for $\lambda_s = 30°$ (note that the flux color scale used here covers a slightly higher range). In this case the majority of the precipitated flux is deposited at $L > 2$, as would be expected for this higher latitude lightning source.

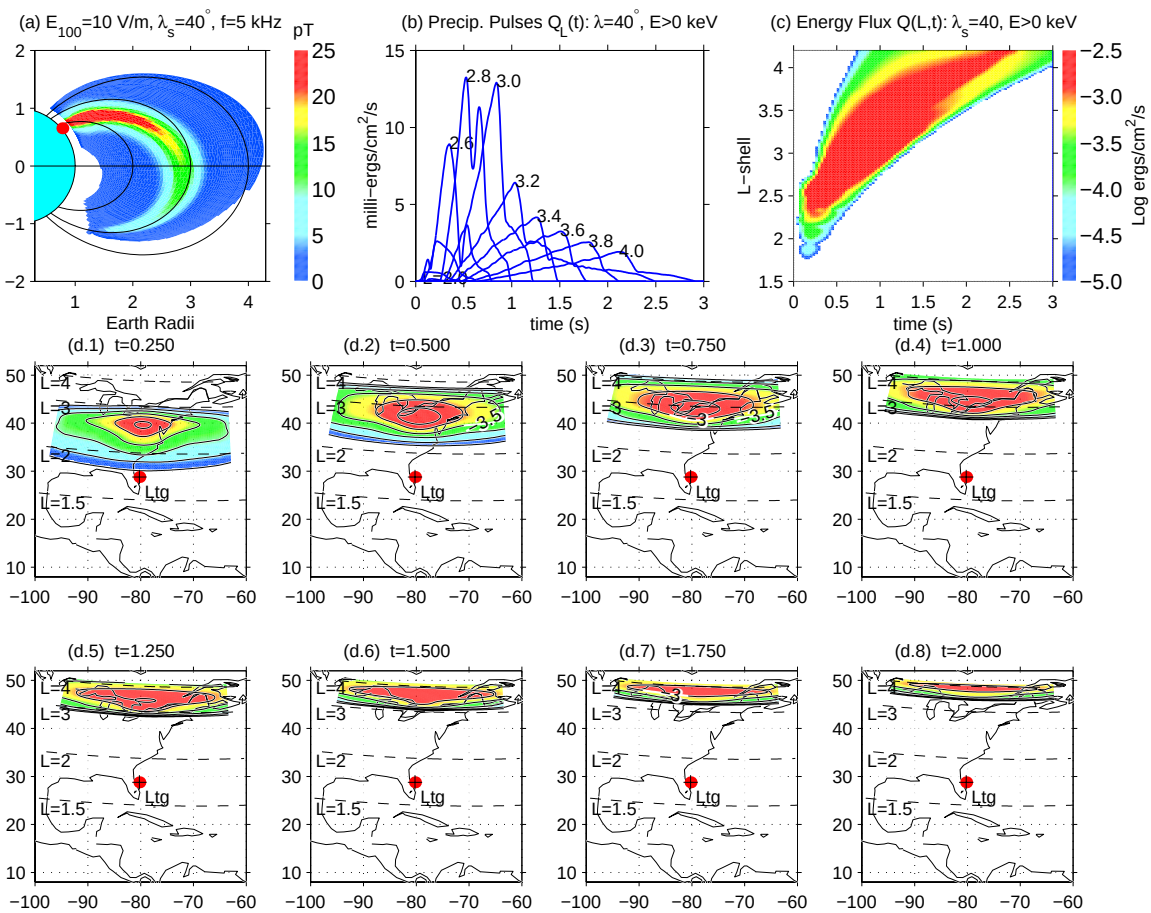

Figure 4.5: Precipitation hotspot time sequence for $\lambda_s = 40°$, $E > 0$.

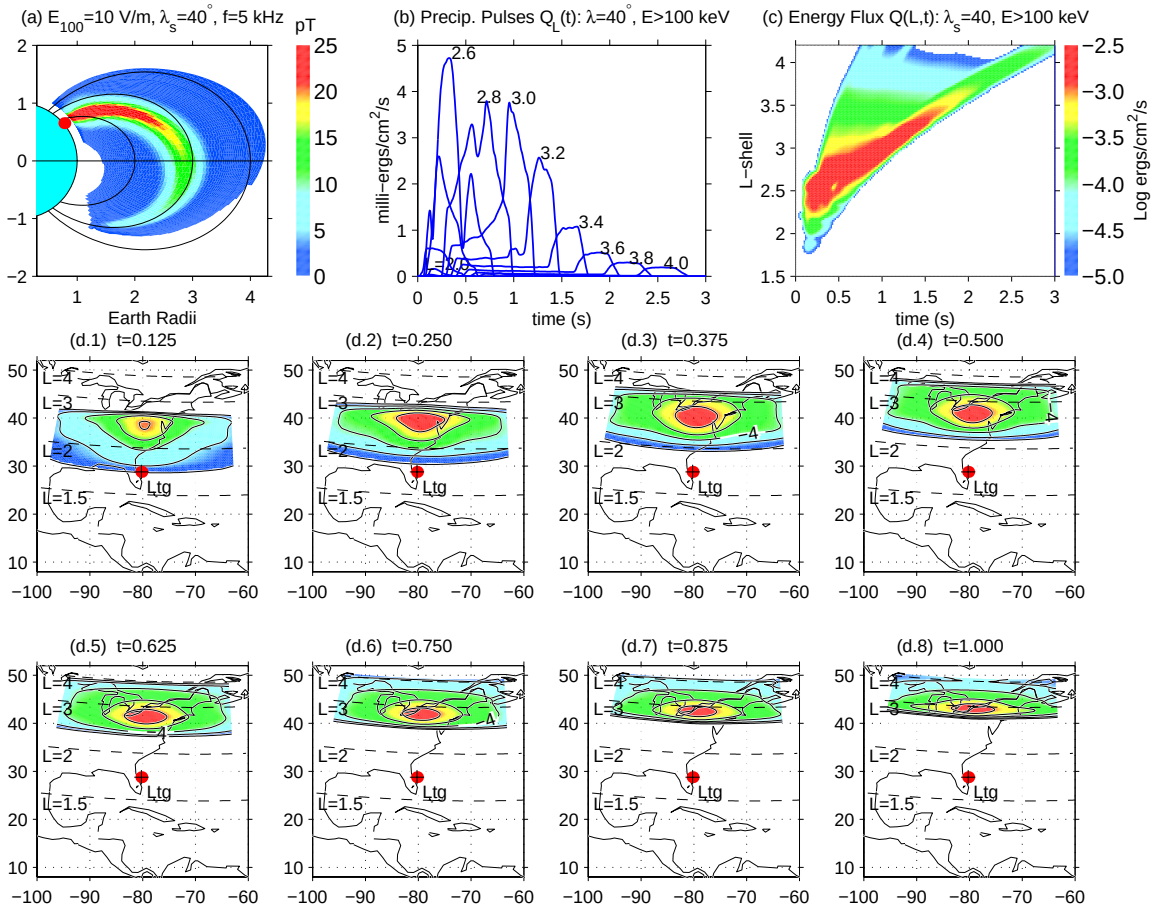

Figure 4.6: Precipitation hotspot time sequence for $\lambda_s = 40°$, $E > 100$ keV.

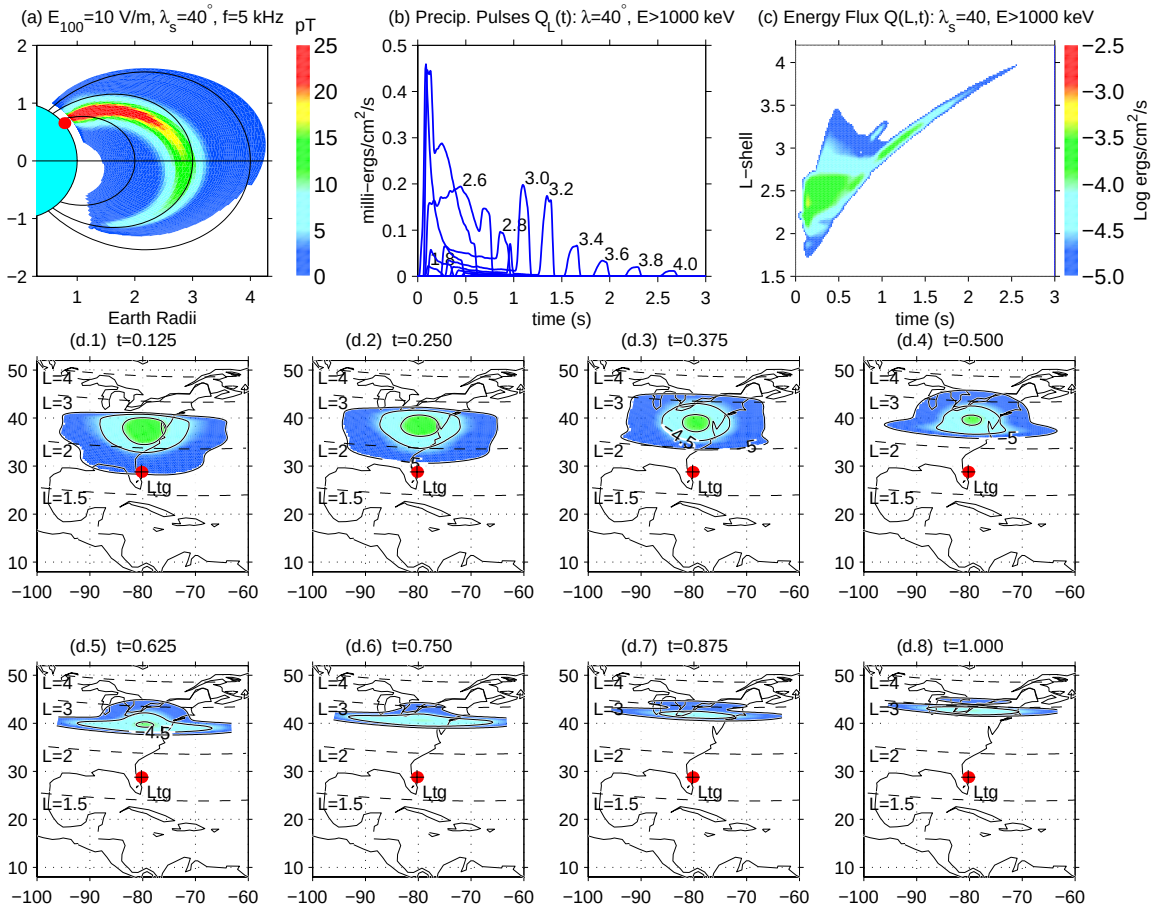

Figure 4.7: Precipitation hotspot time sequence for $\lambda_s = 40°$, $E > 1$ MeV.

4.3 Precipitation Hotspot Summary Plots

To readily compare the effect of different lightning source locations and energy thresholds, several types of fixed-time hotspot summary plots, taken from the previous as well as additional cases, are presented in a side-by-side mosaic format. These types include: 1) hotspot instantaneous peak, 2) total fluence (time-integrated precipitation energy flux), and 3) total electron number flux. Each of the figures to follow (beginning on the next page) shows subplots arranged as three rows of four columns each, where the the lightning source latitude increases over the columns from left to right, and the energy threshold $E > E_{\mathrm{th}}$ increases going from bottom to top.

4.3.1 Hotspot Instantaneous Peak

This first type of summary plot shows that frame $Q(\lambda_p, \delta, t_{\rm pk})$ at time $t = t_{\rm pk}$ (particular to each lightning source latitude and minimum energy threshold) for which the precipitation reaches its peak at some location along the central meridian. Fig. 4.8 shows hotspot peak frames for $\lambda_s = 20°$, $30°$, $40°$ and $50°$ for those energy thresholds discussed previously. Somewhat surprisingly, the central latitude of the hotspot peaks for $E > 0$, $E > 100$ keV (two lower rows) do not track the respective lightning latitudes λ_s (which increases over the columns from left-to-right); however the frames for $E > 1$ MeV (top row) do track λ_s in a more monotonic fashion.

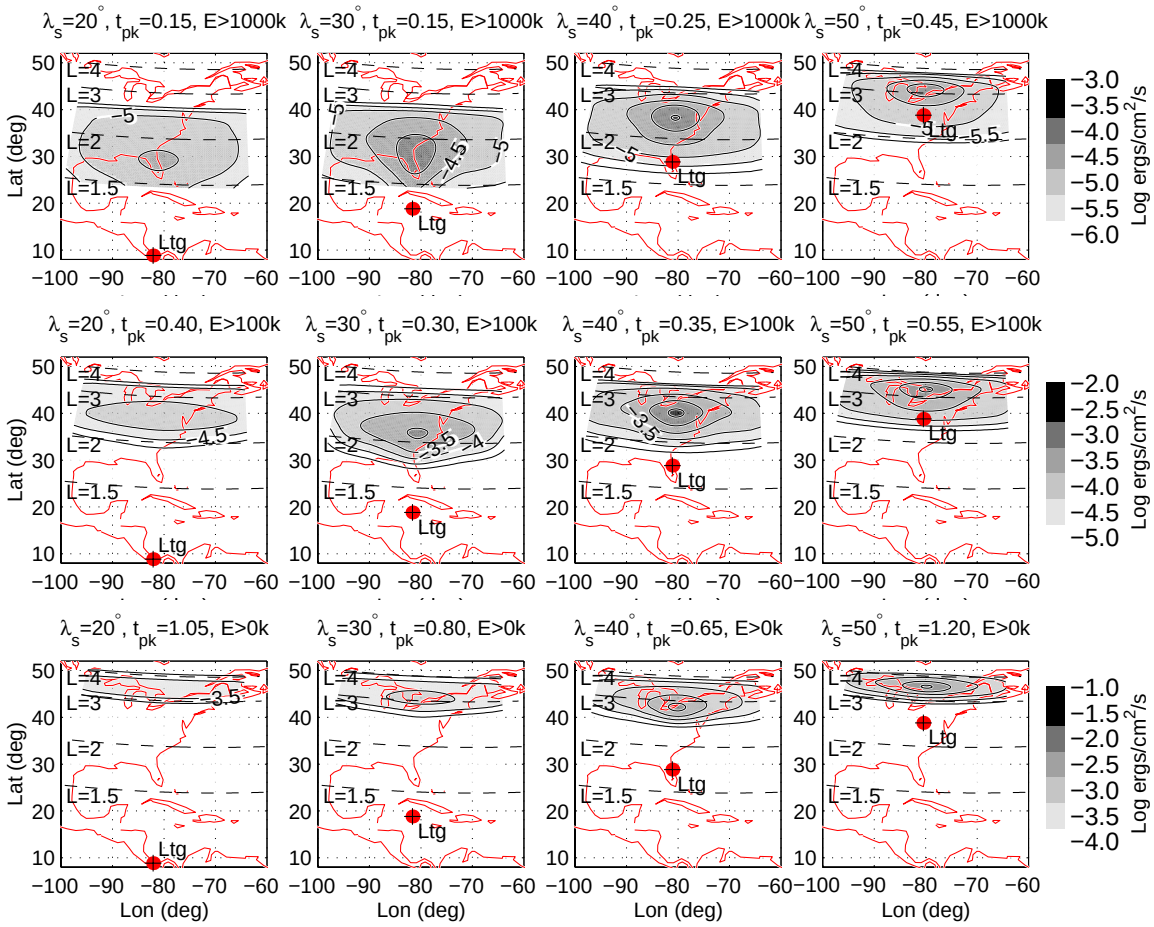

Figure 4.8: Hotspot instantaneous peak for (top to bottom) $E > 1$ MeV, $E > 100$ keV and all $E > 0$, for lightning located at (left to right) $\lambda_s = 20, 30, 40, 50°$.

4.3.2 Hotspot Fluence and Total Energy

Next, Fig. 4.9 shows the time-integrated energy flux, or fluence for each lightning source location. Above each plot panel the total precipitated energy integrated over the entire affected spatial region is indicated in kiloJoules. The result for this lightning intensity $E_{100} = 10$ V/m ranges from $E_{tot} = 956$ kJ for $\lambda_s = 20°$ to $E_{tot} > 7.5$ MJ for $\lambda_s = 40°$, for all $E > 0$. Similar to the case for the instantaneous peak frames, the behavior of the location of maximum fluence tracks the lightning source best for energies $E > 1$ MeV. *These results suggests that the net effect of all the competing factors of lightning source location, resonance interaction length, energy spectral hardness etc. combine in such a way as to cause maximal precipitation for the highest energies to be confined roughly to the range* $2 \leq L \leq 3.2$.

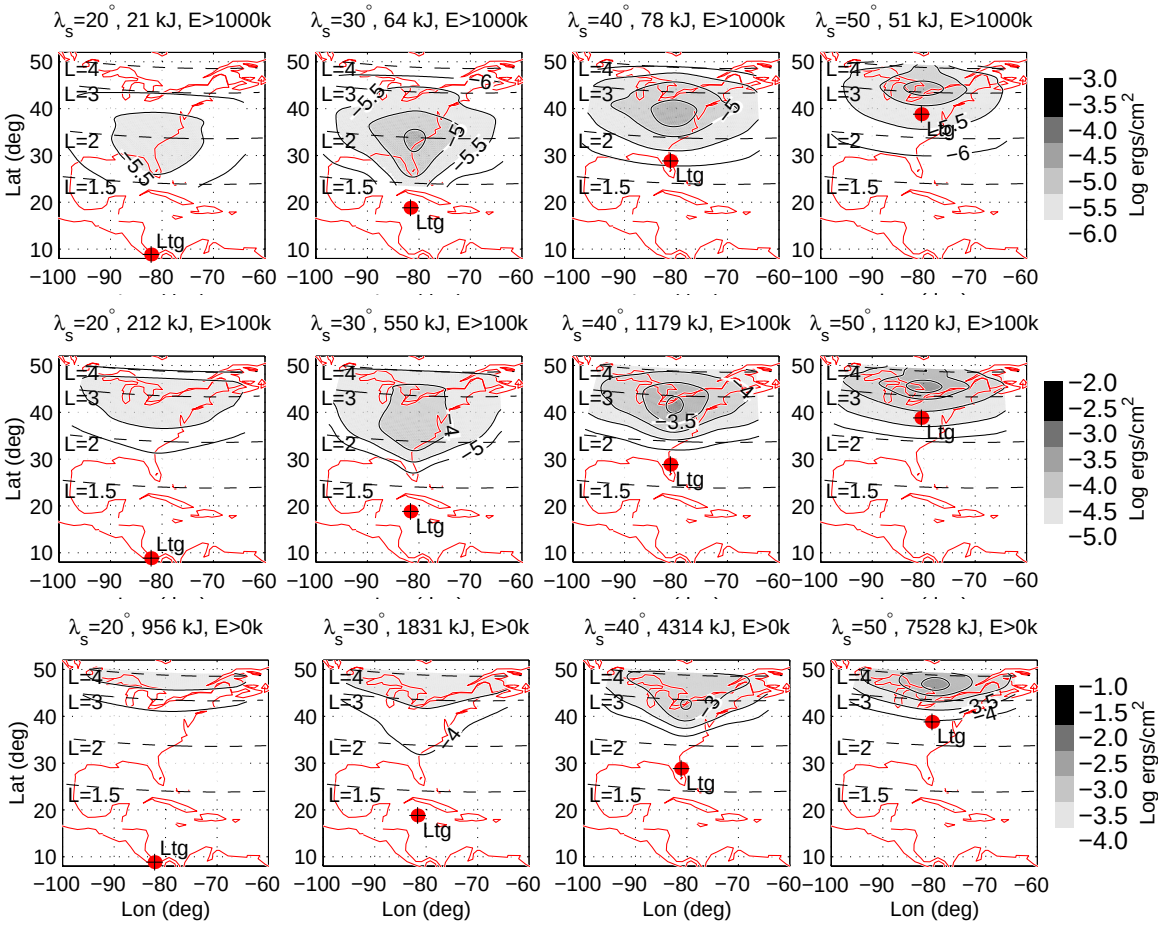

Figure 4.9: Hotspot fluence for (top to bottom) $E > 1$ MeV, $E > 100$ keV and all $E > 0$, for lightning located at (left to right) $\lambda_s = 20°$, $30°$, $40°$ and $50°$.

4.3.3 Hotspot Precipitated Electron Count

Finally, Fig. 4.10 shows the time-integrated electron count spatial density for each lightning source location. Above each plot panel is given the *sum total* precipitated electron count integrated over over the entire affected spatial region. The result for this lightning intensity E_{100}=10 V/m ranges from $N_{tot} = 4.2 \times 10^{20}$ for $\lambda_s = 20°$ to $N_{tot} > 3.7 \times 10^{21}$ for λ_s=50°, for all energies $E > 0$.

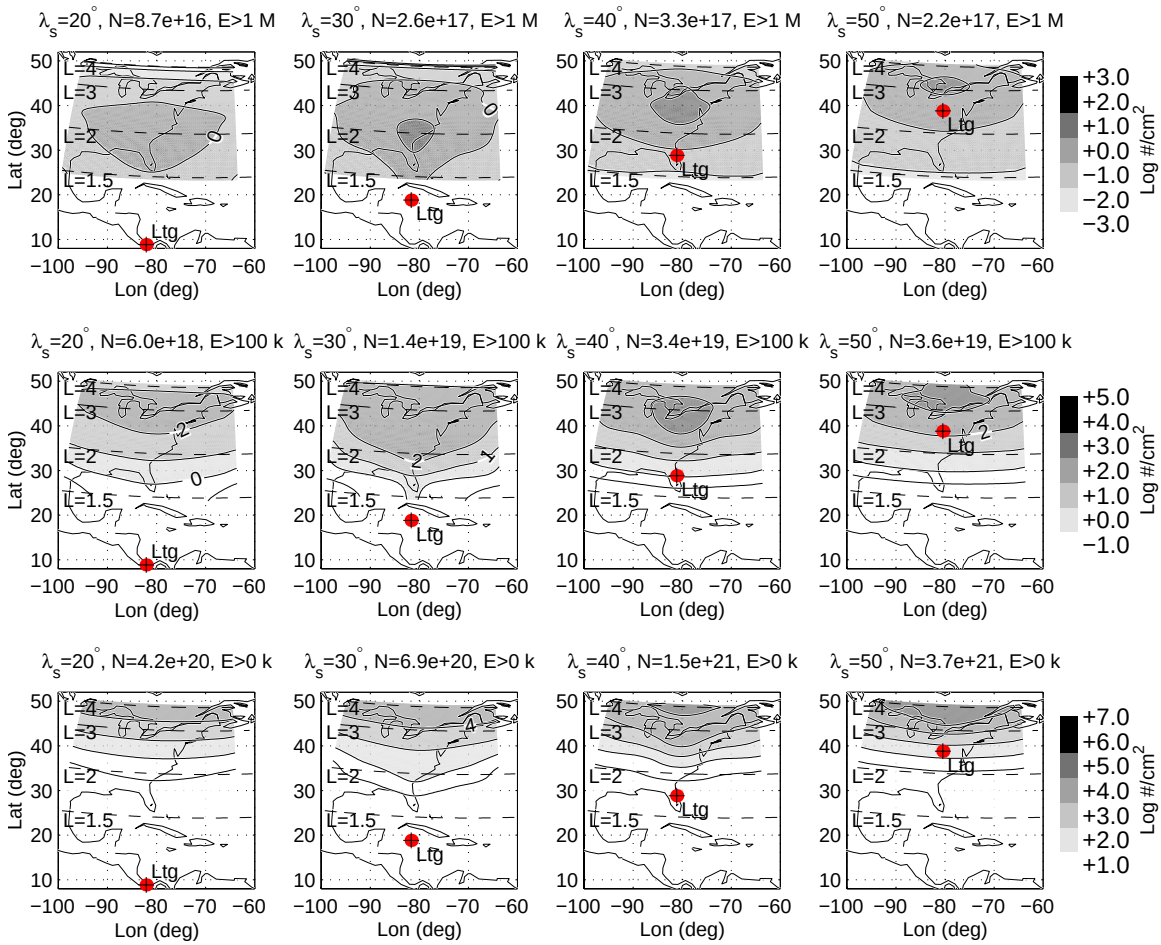

Figure 4.10: Total precipitated electron count for (top to bottom) $E > 1$ MeV, $E > 100$ keV and all $E > 0$, for lightning located at (left to right) $\lambda_s = 20°$, 30°, 40° and 50°.

The spatially-integrated total energy and electron count results listed in each of the summary plot panel titles of Figs. 4.9 and 4.10 are tabulated for convenience in Tables 4.3.3 and 4.3.3 respectively.

Table 4.1: Total precipitated energy flux for $E_{100} = 10$ V/m.

Q_{tot}	$\lambda_s = 20°$	$\lambda_s = 30°$	$\lambda_s = 40°$	$\lambda_s = 50°$
$E > 1$ MeV	21 kJ	64 kJ	78 kJ	51 kJ
$E > 100$ keV	212 kJ	550 kJ	1.2 MJ	1.1 MJ
$E > 0$	956 kJ	1.8 MJ	4.3 MJ	7.5 MJ

Table 4.2: Total precipitated electron count for $E_{100} = 10$ V/m.

N_{tot}	$\lambda_s = 20°$	$\lambda_s = 30°$	$\lambda_s = 40°$	$\lambda_s = 50°$
$E > 1$ MeV	8.7×10^{16}	2.6×10^{17}	3.3×10^{17}	2.2×10^{17}
$E > 100$ keV	6.0×10^{18}	1.4×10^{19}	3.4×10^{19}	3.6×10^{19}
$E > 0$	4.2×10^{20}	6.9×10^{20}	1.5×10^{21}	3.7×10^{21}

4.4 Precipitation Profiles over Latitude and L-shell

The dynamic hotspot and fixed-time summary plots presented in the previous sections all show a marked tendency for both the precipitation energy and electron flux to exhibit especially intense values at higher L-shell values and corresponding mapped precipitation latitudes. It is of interest to summarize this latitude bias by integrating $Q(\lambda_p, \delta, t)$ and $N(L, \delta, t)$ over longitude δ and time t to obtain the distribution over latitude λ and L-shell, denoted $\tilde{Q}(\lambda_p)$ and $\tilde{N}(L)$ respectively, for each lightning source location and for each energy threshold. Note that each profile integrated over latitude would reproduce the respective totals presented in Tables 4.3.3 and 4.3.3.

Energy flux vs. latitude. Fig. 4.11 gives the resulting $\tilde{Q}(\lambda)$ profiles vs. latitude for lightning at $\lambda_s = 20°$, $30°$, $40°$ and $50°$ for $E>0$, $E>100$ keV and $E>1$ MeV, expressed in units Joules/degree of latitude. The curves for $E > 0$ (Fig. 4.11a) are particularly striking as they reveal that roughly three orders of magnitude greater energy is delivered to $\sim 50°$ as compared with $\sim 25°$ geographic latitude (for the Eastern United States mapping) *nearly independent of lightning source latitude.* As the minimum energy threshold is increased these curves flatten in Figs. 4.11a,b in keeping with the trend towards generally lower resonant energies at higher L-shells. In other words, most of the energy delivered to the upper atmosphere at high latitudes is carried by the large fluxes of generally lower energy electrons.

Electron count vs. L-shell. Likewise, Fig. 4.12 gives the resulting $\tilde{N}(L)$ latitude distribution profiles also for lightning at $\lambda_s = 20°$, $30°$, $40°$ and $50°$ for $E > 0$, $E > 100$ keV and $E > 1$ MeV, expressed in units Log el/L (Log electron number count per incremental L-shell). These curves show very similar behavior to the $\tilde{Q}$ curves. In particular the curves for $E > 100$ keV (middle panel) are fairly flat over $L = 2.2 - 3.5$, indicating that lightning wave energy is particularly effective at removing these energetic particles over these L-shells. This result strongly motivates further in-depth study of the total impact of all global lightning activity on the Earth's radiation belts, including contribution to the formation of the slot region.

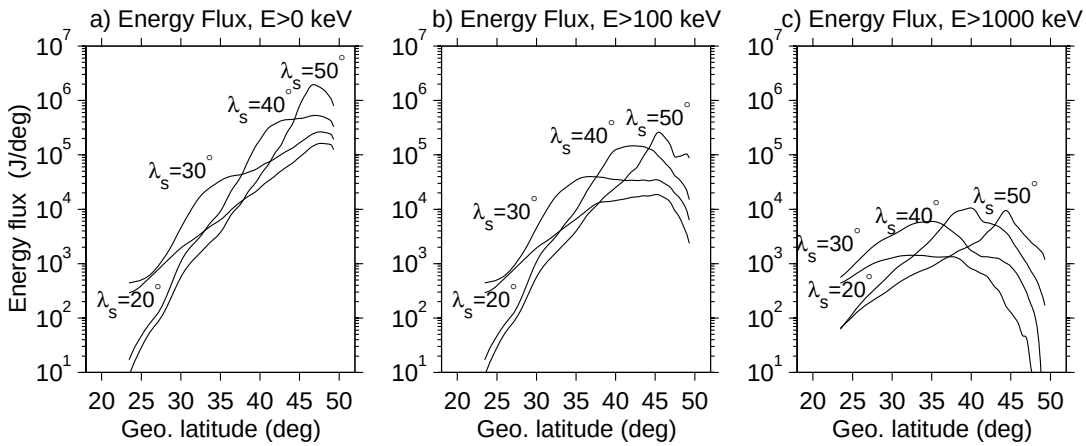

Figure 4.11: Longitude-integrated precipitation energy flux profiles vs. Latitude. Each panel shows results for all lightning source locations. $E_{\rm th}$ increases over the panels from left to right.

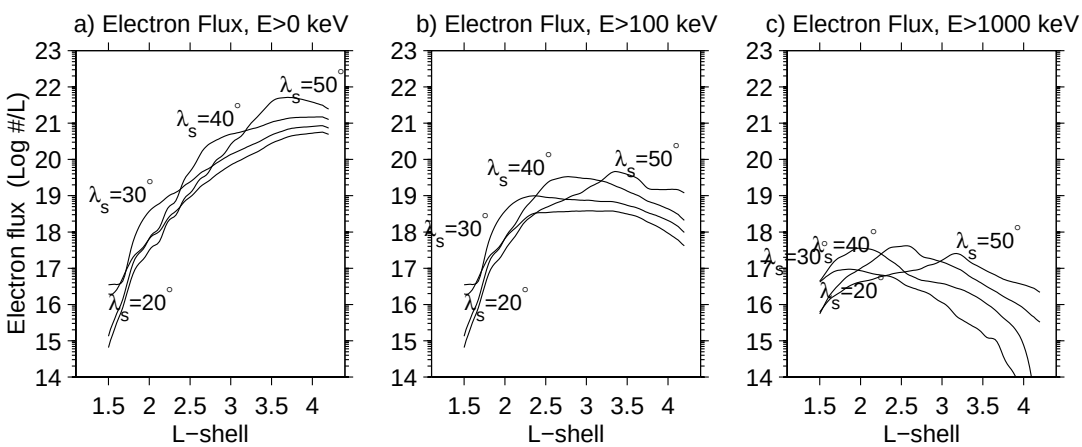

Figure 4.12: Longitude-integrated electron precipitation flux profiles vs. L-shell. Format similar to previous figure except for different abscissa.

Chapter 5

Conclusion

"It is done! [Rev 21:6]"

This chapter concludes the dissertation with a summary of results, discussion in light of related research, application to experimental measurement and suggestions for future work.

5.1 Summary

Chapter 1 introduced the topic of the precipitation of energetic radiation-belt electrons induced by obliquely-propagating lightning-generated whistler waves, reviewing related antecedent computer models and noting the advances required to extend the formulation to the general case. Chapter 2 detailed the procedure by which the oblique whistler wave fields were constructed throughout the magnetosphere, with the general result that a typical strong lightning flash sufficient to achieve free-space peak electric field $E_{100} = 10$ V/m (at the standard reference distance $R = 100$ km) can lead to spatially-variable whistler wave intensities of up to ~ 10 to 20 pT at the magnetic equator (a not uncommon value borne out by measurements presented herein) along the ray paths launched directly over the flash. Chapter 3 presented the detailed energy-time signatures for both peak pitch-angle scattering $\Delta\alpha_{\rm eq}(E,t)$ and electron precipitation flux $\Phi(E,t)$, with corresponding precipitation number $N(t)$ and energy flux $Q(t)$ profiles under the simplifying assumption that such flux is completely deposited upon the first encounter with the atmosphere. Chapter 4 combined the precipitation energy flux profiles at individual L-shells to determine the dynamic energy flux $Q(\lambda_p, \delta, t)$ precipitation footprint or "hot-spot" over extensive geographic regions using a sophisticated extrapolation/interpolation technique. Chapter 4 further calculated the total deposited energy integrated over time and space and showed that, depending on flash location, the total energy can approach 8 MJ (much larger the ~ 53 kJ of VLF electromagnetic wave energy released by the assumed lightning discharge, see Section 2.3.2). In this connection, the extraction from the radiation belts of a total energy in excess of the energy released by the causative lightning discharge is generally consistent with the high degree of "energy leverage" inherent in the cyclotron resonance interaction [*Inan et al.*, 1978]. This leverage arises from the general fact that since the whistler-mode wave is a "slow" electromagnetic wave propagating at speeds substantially less than the speed of light, the role

of the wave magnetic field in the wave/particle interaction is enhanced compared to that of the wave electric field; specifically, the wave can alter the *direction* of the particle momentum vector (i.e. pitch angle) via the $\mathbf{v} \times \mathbf{B^w}$ force without necessarily imparting significant change to the total particle energy. Thus the (up to) ~8 MJ of precipitation energy calculated herein is essentially the energy which was already carried by the initially trapped energetic particles which is then deposited to the atmosphere as a result of relatively slight changes to the particle momentum vectors. Chapter 4 concluded with precipitation energy and number flux profiles vs. latitude and L-shell, revealing the significant bias towards higher latitudes, nearly independent of specific lightning latitude.

5.2 Discussion

5.2.1 Related Theoretical Models

***Chang and Inan* [1985].** The most immediate and direct comparisons may be made with the work of *Chang and Inan* [1985] (hereafter referred to as *Chang*) which presents precipitation energy flux pulses similar to those in Chapter 3 for parallel-propagating (i.e. ducted) whistlers over $L=2$ to 4.5. In making the following comparisons it should be kept in mind that for parallel-propagating waves ($\theta_k = 0$) the resonant electron energies are somewhat lower than those for oblique waves (see Fig. 1.3), and that in general the whistler intensities given by *Chang* assume a different (but roughly equivalent) input wave power spectrum. Nonetheless, for the ducted case at $L = 3.5$, *Chang* Fig. 7 shows (after rescaling for $\Phi_o = 1 \rightarrow 1 \times 10^8$ el/cm^2/s/sr/keV to compare results for identical phase-space distributions f_v) a peak energy flux of 9 milli-ergs/cm^2/s occurring at $t \sim 1.2$ s for a wave magnetic field intensity at $f = 5.1$ kHz of ~8 pT, while from Fig. 3.8 of Chapter 3, interpolating $Q(t)$ profiles between $L = 3.4$ and $L = 3.6$ gives ~3 milli-ergs/cm^2/s at slightly earlier $t \sim 1$ s, which must be adjusted downward for comparison at equal wave intensities (by a factor of 5, giving $B^w_{y,eq} = 40 \rightarrow 8$ pT, from Fig. 2.10), resulting in a comparative peak precipitation energy flux of ~6.6 milli-ergs/cm^2/s, roughly 25% less than that for the ducted case. For $L = 2$ *Chang* shows a peak flux (also after Φ_o scaling) of ~0.8 milli-ergs/cm^2/s at $t = 0.25$ s, for wave intensity 2 pT at $f = 1$ kHz (from Fig. 5 of this reference), while Fig. 3.6 of Chapter 3 gives a peak flux of 1.5 milli-ergs/cm^2/s also slightly earlier than the ducted case at $t = 0.2$ s, which after scaling again downwards ($B^w_{y,eq} = 7 \rightarrow 2$ pT) gives a comparative energy flux of again just over half the ducted case value at 0.43 milli-ergs/cm^2/s. Finally, at $L=4$, *Chang* shows peak flux (after Φ_o scaling) just exceeding 10 milli-ergs/cm^2/s at $t=1.9$ s for wave intensity ~0.5 pT at $f=1$ kHz, while Fig. 3.8 ($\lambda_s = 50°$) shows 14 milli-ergs/cm^2/s at $t=2.1$ s, which after scaling for equivalent wave intensity (from $B^w_{y,eq}=1.65$ pT) becomes 4.2 milli-ergs/cm^2/s, just less than half that for the ducted case. In this last case the slightly *later* arrival time for the peak flux occurs because the oblique-mode ray paths first venture beyond $L=4.0$ before refracting inward back to $L \leq 4$ at latitudes south of the magnetic equator (Fig. 2.4).

These comparisons show that the precipitation energy fluxes calculated herein for oblique whistlers are remarkably similar to those previously calculated for ducted whistlers of equivalent wave intensity. This result is completely in keeping with the moderate decrease in scattering efficiency for a given wave intensity as the wave normal angle becomes non-zero. Considering this result in a broader context, and noting that the volume of the magnetosphere filled by the oblique waves will always be substantially greater than that for ducted waves (assumed limited to a typical duct cross-sectional size of ~0.02 to 0.05 L), the *total* electron precipitation induced by oblique whistler waves will indeed be substantial.

***Inan et al.* [1989].** *Inan et al.* [1989] presents the detailed precipitation signature specific to an event observed on L=2.24 by the *SEEP* satellite (Fig. 14 of that reference), calculated using the formulation of *Chang and Inan* [1985]. In principle this signature may be compared to $\Phi(E,t)$ for $L = 2.2$ in Fig. 3.6 of this present work. Comparing the two signatures, the respective $\Phi(E,t)$ spectral forms and electron count profiles vs. time are similar (after accounting for the fact that the resonant energies for the oblique-mode waves slightly higher than for the ducted-mode considered therein), however the arrival time of the peak flux (and peak counting rate) reported in that study is much delayed to t=0.44 s (to match the observed timing relationship between whistler sferic and precipitation pulse) vs. the t=0.25 s for the oblique case. The reason for this difference in precipitation pulse delay is undoubtedly due to the differing assumptions regarding whistler wave propagation delay and dispersion through the ionosphere and a the assumed magnetospheric cold plasma density model, both of which affect wave arrival time to any $\lambda_{\rm wf}$, underscoring the importance of further comparison with experimental results.

***Jasna et al.* [1993].** A somewhat less direct comparison can be made with *Jasna et al.* [1993] (and later [*Jasna et al.*, 1998]) which considers whistler-mode waves which after injection experience many internal reflections within the inner magnetosphere and ultimately settle to certain L-shells where they reflect back and forth across the magnetic equator (hence termed "MR waves") with wave normal angles approaching the resonance cone (much larger than those angle considered in the present work). In the following comparison it is more appropriate to consider that the ordered *sequence* of events is such that the lightning discharge first gives rise to the oblique electromagnetic whistler waves considered herein which subsequently transition into such MR waves [*Draganov et al.*, 1992]. Nonetheless it is of interest to compare peak scattering and precipitation rates, with the understanding that the MR waves are taken to be monochromatic and essentially electrostatic. With this in mind, Fig. 5.17 of [*Jasna et al.*, 1993] shows electron precipitation flux vs. energy at L=2, 3, 4 for f=2.6, 0.78, 0.33 kHz respectively, all waves having Poynting flux $S^w_{MR} = 113$ pW/m^2/Hz. In particular at L=2 *Jasna et al.* [1993] quotes $\Phi(E = 1.11MeV) = 5.2 \times 10^{-4}$ el/cm^2/s/keV, while Fig. 3.6 of the present work shows electron flux $\Phi(E \sim 1$ MeV) exceeding 10^{-1} el/cm^2/s/keV, some three orders of magnitude higher, but for a duration of only $\sim$ 0.2 s (from the inherently limited

duration of the discrete whistler wave packet) and for a wave power density some ∼20 times higher at $S^w = 2.54$ nW/m^2/Hz (giving $B_y^w \sim 16$ pT at $f = 2.6$ kHz) at the magnetic equator, so that the actual comparable flux is only about ∼40 times higher for equivalent wave intensities.

***Abel and Thorne* [1998a].** An important related modeling development is the extension of the bounce-trajectory/wave-path integrated pitch-angle diffusion/precipitation formulation [*Kennel and Petschek*, 1966; *Lyons and Thorne*, 1973] to include treatment of obliquely-propagating lightning-generated whistlers as given by *Abel and Thorne* [1998a, 1988b] (hereafter referred to collectively as *Abel*). There are three important points to consider when making comparisons between the present results and those of such path-integrated formulations, in particular regarding the manner in which the lightning-generated whistlers are modeled: 1) *Abel* treats these essentially discrete wave packets in the same manner as sustained plasmaspheric hiss, where to account for their transient nature a special "frequency of occurrence" or duty cycle factor (representing both an effective flash rate and implicit global distribution of lightning activity) is applied to the input wave distribution; 2) the obliquely-propagating lightning-generated whistler waves are assigned a single fixed wave normal angle of 45° at all locations; 3) each form of whistler-mode wave energy is assigned a disjoint frequency range, i.e. VLF transmitters occupy $f = 16-22$ kHz, lightning-generated whistlers occupy $f = 4.5 \pm 2$ kHz and ELF hiss occupies $f = 1 \pm 0.5$ kHz, despite the fact that in reality these various forms often overlap in frequency content. On this last point, this frequency-assignment guarantees that ELF hiss will emerge as the dominant contributor to energetic particle loss controlling formation of the slot region, since it is assigned to that frequency range which happens to be most effective in scattering slot region electrons. The fact that whistlers and ELF hiss both have significant wave energy at these lower frequencies (see B_y^w in Fig. 2.2 (bottom row)), at the very least raises the question as to the relative preponderance of these two forms of whistler-mode waves.

Nonetheless, *Abel* does show that at least for some regions, lightning-generated whistlers are indeed more important than ELF/VLF hiss, VLF transmitters or atmospheric coulomb scattering. In particular for energies E=100 keV at L=3, whistler wave energy indeed emerges as the most effective scatterer for pitch-angles at and near the loss-cone, a result not inconsistent with the present calculations. In particular this case may be compared with Fig. 3.7 for L=3, where $\Delta\alpha$(100keV) exceeds 0.2° at $t = 0.9$ s (top-right panel), indicating especially strong scattering induced by this lightning source at λ_s=40°.

5.2.2 Comparison with Experiment

***Voss et al.* [1984].** As mentioned in the introduction, [*Voss et al.*, 1984] presented the first direct one-to-one association between transient energetic electron precipitation events at $L \sim 2.2$ with individual whistlers known to have propagated in the ducted mode. These same data are also presented in *Inan et al.* [1989] which indicates a peak energetic electron count rate approaching 10^4 el/s, nearly $100\times$ the background rate of $\sim 10^2$ el/s for these events, which are reported as being within the strongest 10% of those generally observed. In comparison, Fig. 3.6 of Chapter 3 for $L = 2.2$ shows a peak count rate 3×10^3 for an idealized particle detector optimized to observe just the loss-cone, which is nonetheless above this background rate. While detailed evaluation would require an accurate model for particle detector characteristics (beyond the scope of this work), these results suggests that *oblique whistler-induced electron precipitation may well be detectable* using present-day instruments, at least for strong lightning and optimum detector location with respect to the maximally affected L-shells.

***Burgess and Inan* [1993].** Lightning-induced electron precipitation (LEP) events from ducted whistlers are now known to be regularly detectable be means of their effects on subionospheric VLF signals. Amplitude and phase of these VLF signals are sensitive indicators of secondary ionization produced by precipitating bursts of energetic electrons observed in direct and detailed association with ducted whistlers [*Burgess and Inan*, 1993, and references therein]. Analysis indicates [*Lev-Tov et al.*, 1996] that secondary ionization enhancements which perturb the VLF signals are those that would be expected from LEP bursts of the type observed on satellites [*Voss et al.*, 1984]. Since the expected flux levels, energy spectra and temporal signatures of oblique-whistler induced precipitation are similar to those induced by ducted whistlers (based on the comparisons made in Section 5.2.1), the ionospheric effects of such precipitation should also be readily measurable with subionospheric techniques. The detailed spatial, temporal and energy spectral distributions of precipitation hotspots as determined in this thesis should provide guidance in searching for such signatures in VLF data.

***Yip et al.* [1991].** Regarding the poleward displacement of the precipitation hotspots, the experimental work of *Yip et al.* [1991] reports on the spatial relationship between individual lightning discharges of known strength and location and "Trimpi" perturbations observed in man-made subionospheric VLF transmitter signals. Indeed these results tend to show that, for example, lightning at $L=2$ can affect signal paths on the order of ten degrees poleward, while *not* affecting a signal path very close to the lightning flashes themselves (this does not preclude so-called "early/fast" events above these flashes, which are *not* due to LEP). While no whistler data were presented therein, the correspondence between the results of *Yip et al.* [1991] and the present calculations may already provide support to confirm the present results.

5.2.3 General Remarks

The relative role played by ducted (i.e $\theta_k = 0$) vs. oblique (also termed "non-ducted") whistlers regarding the loss of radiation belt particles remains to be completely determined [*Walt et al.*, 1996]. Historically, the potentially important role of ducted whistlers has been given first consideration primarily by virtue of the readily-available measurement of such whistlers provided by established networks of ground-based VLF receivers which led to the early discovery that these whistlers were in fact associated with strong LEP events [*Voss et al.*, 1984] (note that the SEEP satellite was not instrumented with a wave receiver and was thus not able to determine the specific type of whistler). Indeed, subsequent work by *Burgess and Inan* [1993] (see earlier paragraph) indicates that the effect of ducted whistlers may well be comparable to other loss processes controlling radiation belt equilibrium, subject to certain assumptions regarding the volume of the magnetosphere which may be populated by ducts at any given time.

In the present context, while the subject of the structure and spatial occupancy of ducts within a generally smooth magnetosphere is beyond the scope of this work, it should nonetheless be recognized that whenever a ducted whistler occurs, there will of necessity be coupling into the oblique wave mode for regions immediately surrounding the foot of the duct, and likely for vast regions inside and beyond the L-shell of the duct, with both wave modes leading to associated precipitation. In a related scenario, the occasional presence of an abrupt primary (or secondary) plasmapause (that sharp density dropoff for $L > L_k$ beyond some L_k-shell referred to as the "knee", c.f. Fig. 2.3) occurring at low values of L_k (e.g. $L_k < 4$) and able to guide whistlers in the same manner as a duct [*Inan and Bell*, 1977] may well "capture" the initially obliquely-propagating whistler wave energy, concentrating the ray paths and thereby greatly increasing the wave intensity along this L_k-shell, such that the strongest LEP-pulse may likely occur at the foot of this L_k-shell (for which one would also expect the whistler to exit the magnetosphere so as to be observable by ground receivers) even as oblique-mode LEP also occurs everywhere for $L < L_k$ in accordance with the calculations herein. Yet even in such cases where a whistler is so guided and perhaps intensified along some particular L-shell (whether by duct or plasmapause), the results and comparisons presented herein nonetheless indicate that while the most intense LEP may indeed occur at the foot of that particular L-shell, the oblique-mode LEP occurring simultaneously over the vast majority of L-shells will ultimately lead to the far greater overall total precipitation.

5.3 Suggestions for Future Work

Future work can be classified into both experimental tests regarding the validity of certain model assumptions and the accuracy of the predictions, and theoretical enhancements to improve the fidelity of the calculations and to extend the formulation to cover other resonance regimes.

Lightning Model. First, the model presented in Chapter 2 which connects an individual lightning discharge of given characteristics to the resulting oblique whistler wave field intensities in the magnetosphere would benefit from comparison with measured data. While the respective lightning strengths assumed and the resulting whistler intensities calculated are indeed both commonly observed, the task of associating these intensities experimentally remains to be done. In this regard, whistler data (intensity and wave normal angles) already collected by the POLAR satellite could be compared against National Lightning Detection Network (NLDN) data (for regions over the continental United States).

Second, intra-cloud lightning discharges having significant horizontal current structure and which thus illuminate the magnetosphere with a broadside radiation pattern, are known to out-number cloud-to-ground discharges by $\sim$3:1, and by this favorable pattern it may well be that the strongest LEP events are associated with such orientations. At the same time, typical cloud-to-cloud discharges are generally weaker than typical cloud-to-ground discharges, which would tend to counteract the favorable radiation pattern regarding overall precipitation fluxes. Accordingly, the lightning model should be generalized for such cases and the relative LEP intensities and overall contributions should be compared for selected orientations. Such extension would be necessary in order to provide the most complete estimates for the total contribution of lightning to radiation belt losses.

Testable Predictions. Clearly there is a need to test the predicted signatures of Chapter 3 and the effect at the ionosphere (as discussed above) and on the radiation belt loss rates as indicated in Chapter 4. For the precipitation signatures the best comparison would be for simultaneous six-component wave and particle data to both be measured *in-situ* within the magnetosphere, whether by a single satellite near the magnetic equator, or by two satellite in conjunction along a field line (one at the interaction region, the other at the foot of the L-shell where the precipitation pulse should be easier to measure). In addition, existing LEP event records could be checked against ground lightning and whistler data, continuing the work of *Walt et al.* [1996]. In this context, it may be appropriate to utilized a threshold for minimum scattered angle $\Delta\alpha_{\mathrm{eq_{th}}}$ as discussed in Section 3.2.4 so that only those fluxes for $\Delta\alpha_{\mathrm{eq}} > \Delta\alpha_{\mathrm{eq_{th}}}$ are computed in order to to better compare against measurements where the scattered particles emerge well beyond the background fluxes associated with a more-realistic soft edge to the loss-cone flux distribution.

For ionospheric effects, the network of VLF remote sensing receivers know as HAIL (Holographic Array for Ionospheric Lightning research) [*Johnson et al.*, 1998] now in operation is ideally suited for an immediate check of the predicted energy flux onset and peak latitude-time profiles as shown in e.g. Fig. 4.3 (upper-right), for events detected along multiple signal paths. Furthermore the specific effects observed along each signal path, when matched to a lightning discharge of known location and intensity, would serve as a check on the strength of the interaction over L-shells within the monitored region (subject to assumptions regarding the specific subionospheric VLF wave scattering effects and ionization enhancements with altitude associated with specific precipitation $\Phi(E,t)$ signatures).

Radiation Belt Losses. The extension of the present results to calculate the total impact of all lightning induced electron precipitation is an obvious next step. Such calculations would involve assumptions of total energetic electron tube content over energy range and L-shell, scattering at the edge of the loss-cone as predicted herein for an assumed distribution of lightning sources, and further assumptions regarding mechanism(s) by which the vast majority of particles not initially at the loss-cone otherwise diffuse to replenish loss-cone fluxes as they are precipitated (e.g. [*Jasna et al.*, 1993]). From the precipitated electron count profiles vs. L-shell given at the end of Chapter 4, one can expect pronounced effects within the slot region; it merely remains to establish the *rate* at which all global lightning activity, whether considered alone or in concert with plasmaspheric hiss, can be expected to give rise to this region of depleted energetic electron densities, known to form within days of being replenished by solar wind injections.

Extension to Others Regimes. Finally, there are a number of possible minor and major uses and enhancements for this very general formulation. First, the precipitation signatures presented herein are for only one assumed model for the cold plasma density which supports the whistler waves. Since the wave velocity and resonance condition are both controlled by this assumed density, it would be very useful to explore the sensitivity of the precipitation signatures (timing, energy range and flux levels) to different cold plasma density profiles, possibly even including a sharp, low L-shell plasmapause to provide for concentration of the wave energy at the knee.

Second, the specification of wave properties through wave normal angle θ_k, wave power density S^w and group time dispersion t_g is completely general, allowing for nearly arbitrary forms (so long as the f-t behavior is single valued). This generality permits not only direct comparison of ducted and oblique waves for identical assumed density models using the same resonance integration kernel, but also the treatment of pulses, frequency-time ramps, chorus and even triggered emissions. In addition this generality permits treatment of (a-priori specified) growth in wave intensity within the interaction region which can occur from wave/particle feedback (e.g. [*Helliwell and Inan*, 1982], whether for simple a-priori specified wave growth profiles, or possibly for the self-consistent superposition of re-radiated wave fields with the initial source whistlers.

Finally, the general formulation presented here could be readily adapted to other resonance regimes, including 1) Landau resonance, for which particles having $v_{\|}$ matched to the wave velocity (in the same direction) experience strong interaction with the significant wave electric field parallel to the magnetic field lines (much more so than for the ducted landau resonance considered by *Tkalcevic et al.*. [1984]), and 2) higher cyclotron resonance harmonics (i.e. beyond the first-order resonance for counter-streaming particles considered herein) could be explored, which would extend the treatment of transient oblique whistler wave interactions to the full set of resonance modes to ensure that the most effective regimes have indeed been identified and properly quantified.

Bibliography

[*Abel and Thorne*, 1998a] Abel, B. and R.M. Thorne, Electron scattering loss in Earth's inner magnetosphere. 1. Dominant physical processes, *J. Geophys. Res.*, *103*, no. A2, 2385–96, Feb 1998.

[*Abel and Thorne*, 1998b] Abel, B. and R.M. Thorne, Electron scattering loss in Earth's inner magnetosphere. 2. Sensitivity to model parameters, *J. Geophys. Res.*, *103*, no. A2, 2397–407, Feb 1998.

[*Baker et al.*, 1997] Baker, D.N., Li X. Turner N. Allen J.H. Bargatze L.F. Blake J.B. Sheldon R.B. Spence H.E. Belian R.D. Reeves G.D. Kanekal S.G. Klecker B. Lepping R.P. Ogilvie K. Mewaldt R.A. Onsager T. Singer H.J. and G. Rostoker, Recurrent geomagnetic storms and relativistic electron enhancements in the outer magnetosphere: ISTP coordinated measurements, *J. Geophys. Res.*, *102*, no. A7, 14141–8, Jul 1997.

[*Bell*, 1984] Bell, T.F., The nonlinear gyroresonance interaction between energetic electrons and coherent VLF waves propagating at an arbitrary angle with respect to the Earth's magnetic field, *J. Geophys. Res.*, *89*, no. A2, 905–18, Feb 1984.

[*Bell*, 1986] Bell, T.F., The wave magnetic field amplitude threshold for nonlinear trapping of energetic gyroresonant and Landau resonant electrons by nonducted VLF waves in the magnetosphere, *J. Geophys. Res.*, *91*, no. A4, 4365–79, Apr 1986.

[*Brice*, 1964] Brice, N., Fundamentals of VLF emission generation mechanisms, *J. Geophys. Res.*, *69*, 4515, 1964.

[*Burgess and Inan*, 1993] Burgess, W.C. and U.S. Inan, The role of ducted whistlers in the precipitation loss and equilibrium flux of radiation belt electrons, *J. Geophys. Res.*, *98*, no. A9, 15643–65, Sep 1993.

[*Burtis*, 1974] Burtis, W.J., *User's Guide to the Stanford VLF Raytracing Program*, Stanford University, 1974.

[*Carlson et al.*, 1990] Carlson, C.R., Helliwell R.A. and U.S. Inan, Space-time evolution of whistler mode wave growth in the magnetosphere, *J. Geophys. Res.*, *95*, no. A9, 15073–89, Sep 1990.

[*Carpenter et al.*, 1971] Carpenter, D.L., Park C.G. Arens J.F. and D.J. Williams, Position of the plasmapause during a stormtime increase in trapped energetic (E¿280 keV) electrons, *J. Geophys. Res.*, *76*, no. 19, 4669–73, Jul 1971.

[*Carpenter et al.*, 1984] Carpenter, D.L., Inan U.S. Trimpi M.L. Helliwell R.A. and J.P. Katsufrakis, Perturbations of subionospheric LF and MF signals due to whistler-induced electron precipitation bursts, *J. Geophys. Res.*, *89*, no. A11, 9857–62, Nov 1984.

[*Carpenter and Inan*, 1987] Carpenter, D.L. and U.S. Inan, Seasonal, latitudinal and diurnal distributions of whistler-induced electron precipitation events, *J. Geophys. Res.*, *92*, no. A4, 3429–35, Apr 1987.

[*Carpenter and Anderson*, 1992] Carpenter, D.L. and R.R. Anderson, An ISEE/whistler model of equatorial electron density in the magnetosphere, *J. Geophys. Res.*, *97*, no. A2, 1097–108, Feb 1992.

[*Chang*, 1983] Chang, C.H., Cyclotron Resonant Scattering of Energetic Electrons by Electromagnetic Waves in the Magnetosphere, *Tech. Rep. E414-1*, STARLAB, Stanford Electron. Labs., Stanford Univ., Stanford, CA, 1983.

[*Chang et al.*, 1983] Chang, H.C., Inan U.S. and T.F. Bell, Energetic electron precipitation due to gyroresonant interactions in the magnetosphere involving coherent VLF waves with slowly varying frequency, *J. Geophys. Res.*, *88*, no. A9, 7037–50, Sep 1983.

[*Chang and Inan*, 1985] Chang, H.C. and U.S. Inan, Lightning-induced electron precipitation from the magnetosphere, *J. Geophys. Res.*, *90*, no. A2, 1531–41, Feb 1985.

[*Chang and Inan*, 1985] Chang, H.C. and U.S. Inan, Test particle modeling of wave-induced energetic electron precipitation, *J. Geophys. Res.*, *90*, no. A7, 6409–18, Jul 1985.

[*Cornwall*, 1964] Cornwall, J. M., Scattering of Energetic Trapped Electrons by Very-Low-Frequency Waves, *J. Geophys. Res.*, *69*, 1251, 1964.

[*Crary*, 1961] Crary, J.H., The effect of the earth-ionosphere waveguide on whistlers, *Tech. Rep. 9*, Radiosci. Lab., Stanford Electron. Labs., Stanford Univ., Stanford, CA, 1961.

[*Cummer and Inan*, 1997] Cummer, S.A. and U.S. Inan, Measurement of charge transfer in sprite-producing lightning using ELF radio atmospherics, *Geophys. Res. Lett.*, *24*, no. 14, 1731–4, Jul 1997.

[*Dungey*, 1963] Dungey, J. W., Loss of Van Allen Electrons due to Whistlers, *Planet. Space Sci.*, *11*, 591, 1963.

[*Draganov et al.*, 1992] Draganov, A.B., Inan U.S. Sonwalkar V.S. and T.F. Bell, Magnetospherically reflected whistlers as a source of plasmaspheric hiss, *Geophys. Res. Letters*, *19*, no. 3, 233–6, Feb 1992.

[*Dysthe*, 1971] Dysthe, K. B., Some studies of triggered whistler emissions, *J. Geophys. Res.*, *76*, 6915, 1971.

[*Edgar*, 1976] Edgar, B.C., The upper and lower frequency cutoffs of magnetospherically reflected whistlers, *J. Geophys. Res.*, *81*, 205, 1976.

[*Gurnett et al.*, 1995] Gurnett, D. A., A. M. Persoon, R. F. Randall, D. L. Odem, S. L. Remington., T. F. Averkamp, M. M. DeBower, G. B. Hospodarsky, R. L. Huff, D. L. Kirchner, M. A. Mitchell, B. T. Pham, J. R. Phillips, W. J. Schintler, P Sheyko and D. R. Tomash, The POLAR plasma wave instrument, *Space Sci. Rev., 71*, 1995.

[*Helliwell*, 1965] Helliwell, R.A., *Whistlers and Related Ionospheric Phenomena*, Stanford Univ. Press, Stanford, CA, 1965.

[*Helliwell and Inan*, 1982] Helliwell, R.A. and U.S. Inan, VLF wave growth and discrete emission triggering in the magnetosphere: a feedback model, *J. Geophys. Res.*, *87*, no. A5, 3537–50, May 1982.

[*Helliwell et al.*, 1990] Helliwell, R.A., Mielke T. and U.S. Inan, Rapid whistler-mode wave growth resulting from frequency-time curvature, *Geophys. Res. Lett.*, *17*, no. 5, 599–602, Apr 1990.

[*Imhof and Reagan*, 1973] Imhof, W.L., Gaines E.E. and J.B. Reagan, Dynamic variations in intensity and energy spectra of electrons in the inner radiation belt, *J. Geophys. Res.*, *78*, no. 22, 4568–77, Aug 1973.

[*Imhof et al.*, 1983] Imhof, W.L., Reagen J.B. Voss H.D. Gaines E.E. Datlowe D.W. Mobilia J. Helliwell R.A. Inan U.S. Katsufrakis J. and R.G. Joiner, The modulated precipitation of radiation belt electrons by controlled signals from VLF transmitters, *Geophys. Res. Letters*, *10*, no. 8, 615–18, 1983.

[*Imhof et al.*, 1986] Imhof, W.L., Voss H.D. Walt M. Gaines E.E. Mobilia J. Datlowe D.W. and J.B. Reagen, Slot region electron precipitation by lightning, VLF chorus and plasmaspheric hiss, *J. Geophys. Res.*, *91*, no. A8, 8883–94, Aug 1986.

[*Imhof et al.*, 1989] Imhof, W.L., Voss H.D. Mobilia J. Walt M. Inan U.S. and D.L. Carpenter, Characteristics of short-duration electron precipitation bursts and their relationship with VLF wave activity, *J. Geophys. Res.*, *94*, no. A8, 10079–93, Aug 1989.

[*Imhof et al.*, 1997] Imhof, W.L., Mobilia J. Voss H.D. Collin H.L. Walt M. Anderson R.R. and J.R. Wygant, Association of waves with narrow particle dropouts in the outer radiation belt, *J. Geophys. Res.*, *102*, no. A6, 11429–41, Jun 1997.

[*Inan*, 1977] Inan, U.S., Non-Linear Gyroresonant Interactions of Energetic Particles and Coherent VLF Waves in the Magnetosphere, *Tech. Rep. 3414-3*, Radiosci. Lab., Stanford Electron. Labs., Stanford Univ., Stanford, CA, 1977.

[*Inan and Bell*, 1977] Inan, U.S. and T.F. Bell, The plasmapause as a VLF wave guide, *J. Geophys. Res.*, *82*, no. 19, 2819–27, Jul 1977.

[*Inan et al.*, 1978] Inan, U.S., Bell T.F. and R.A. Helliwell, Nonlinear pitch angle scattering of energetic electrons by coherent VLF waves in the magnetosphere, *J. Geophys. Res.*, *83*, no. A7, 3235–53, Jul 1978.

[*Inan et al.*, 1982] Inan, U.S., Bell T.F. and H.C. Chang, Particle precipitation induced by short-duration VLF waves in the magnetosphere, *J. Geophys. Res.*, *87*, no. A8, 6243–64, Aug 1982.

[*Inan and Helliwell*, 1982] Inan, U.S. and R.A. Helliwell, DE-1 observations of VLF transmitter signals and wave-particle interactions in the magnetosphere, *Geophys. Res. Lett.*, *9*, no. 9, 917–20, Sep 1982.

[*Inan et al.*, 1984] Inan, U.S., Chang H.C. and R.A. Helliwell, Electron precipitation zones around major ground-based VLF signal sources, *J. Geophys. Res.*, *89*, no. A5, 2891–906, May 1984.

[*Inan et al.*, 1985] Inan, U.S., Chang H.C. Helliwell R.A. Imhof W.L. Reagan J.B. and M. Walt, Precipitation of radiation belt electrons by man-made waves: a comparison between theory and measurement, *J. Geophys. Res.*, *90*, no. A1, 359–69, Jan 1985.

[*Inan et al.*, 1985] Inan, U.S., Carpenter D.L. Helliwell R.A. and J.P. Katsufrakis, Subionosphere VLF/LF phase perturbations produced by lightning-whistler induced particle precipitation, *J. Geophys. Res.*, *90*, no. A8, 7457–69, Aug 1985.

[*Inan and Carpenter*, 1986] Inan, U.S. and D.L. Carpenter, On the correlation of whistlers and associated subionospheric VLF/LF perturbations, *J. Geophys. Res.*, *91*, no. A3, 3106–16, Mar 1986.

[*Inan*, 1987] Inan, U.S., Gyroresonant pitch angle scattering by coherent and incoherent whistler mode waves in the magnetosphere, *J. Geophys. Res.*, *92*, no. A1, 127–42, Jan 1987.

[*Inan et al.*, 1988] Inan, U.S., Burgess W.C. Wolf T.G. Shafer D.C. and R.E. Orville, Lightning-associated precipitation of MeV electrons from the inner radiation belt, *Geophys. Res. Lett.*, *15*, no. 2, 172–5, Feb 1988.

[*Inan et al.*, 1989] Inan, U.S., Walt M. Voss H.D. and W.L. Imhof, Energy spectra and pitch angle distributions of lightning-induced electron precipitation: analysis of an event observed on the S81-1 (SEEP) satellite, *J. Geophys. Res.*, *94*, no. A2, 1379–401, Feb 1989.

[*Inan et al.*, 1990] Inan, U.S., Knifsend F.A. and J. Oh, Subionospheric VLF 'imaging' of lightening-induced electron precipitation from the magnetosphere, *J. Geophys. Res.*, *95*, no. A10, 17217–31, Oct 1990.

[*Jasna et al.*, 1992] Jasna, D., Inan U.S. and T.F. Bell, Precipitation of suprathermal (100 eV) electrons by oblique whistler waves, *Geophys. Res. Lett.*, *19*, no. 16, 1639–42, Aug 1992.

[*Jasna et al.*, 1993] Jasna, D., Inan U.S. and T.F. Bell, Resonant interactions between radiation belt electrons and whistler mode waves in the magnetosphere, *Publications of the Faculty of Electrical Engineering, Series: Engineering Physics*, 49–66, 1993.

[*Jasna et al.*, 1998] Jasna, D., Inan U.S. and T.F. Bell, Precipitation of radiation belt electrons by magnetospherically reflected whistlers, *J. Geophys. Res.*, *37*, no. A5, 9249–60, May 1998.

[*Johnson et al.*, 1998] Johnson, M.P., U.S. Inan and S.J. Lev-tov, VLF signatures of lightning-induced ionospheric disturbances measured at multiple sites, *to be submitted to J. Geophys. Res.*, Nov 1998.

[*Kennel and Petschek*, 1966] Kennel, C. F and H. E. Petschek, Limits on stable trapped particle fluxes, *J. Geophys. Res.*, *71*, 1, 1966.

[*Kurth and Gurnett*, 1991] Kurth, W.S. and D.A. Gurnett, Plasma waves in planetary magnetospheres, *J. Geophys. Res.*, *96*, 18977–91, Oct 1991.

[*Lev-Tov et al.*, 1996] Lev-Tov, S.J., Inan U.S. Smith A.J. and M.A. Clilverd, Characteristics of localized ionospheric disturbances inferred from VLF measurements at two closely spaced receivers, *J. Geophys. Res.*, *101*, no. A7, 15737–47, Jul 1996.

[*Li et al.*, 1997] Xinlin Li, Baker, D.N. Temerin M. Cayton T.E. Reeves E.G.D. Christensen R.A. Blake J.B. Looper M.D. Nakamura R. and S.G. Kanekal, Multisatellite observations of the outer zone electron variation during the November 3-4, 1993, magnetic storm, *J. Geophys. Res.*, *102*, no. A7, 14123–40, Jul 1997.

[*Lyons and Kennel*, 1972] Lyons, L.R. and C.F. Kennel, Formation of the slot between the inner and outer electron radiation belts, *Trans. Am. Geophys. Union*, *53*, no. 4, 485, Apr 1972.

[*Lyons and Thorne*, 1973] Lyons, L.R. and R.M. Thorne, Equilibrium structure of radiation belt electrons, *J. Geophys. Res.*, *78*, no. 13, 2142–9, May 1973.

[*Lyons and Williams*, 1975a] Lyons, L.R. and D.J. Williams, The quiet time structure of energetic (35-560 keV) radiation belt electrons, *J. Geophys. Res.*, *80*, no. 7, 943–50, Mar 1975.

[*Lyons and Williams*, 1975b] Lyons, L.R. and D.J. Williams, The storm and poststorm evolution of energetic (35-560 keV) radiation belt electron distributions, *J. Geophys. Res.*, *80*, no. 28, 3985–94, Oct 1975.

[*McIlwain*, 1997] McIlwain, C.E, Processes acting upon outer zone electrons, *Radiation Belts Models and Standards*, 15–26, 1997.

[*Means*, 1972] Means, J. D., Use of the three-dimensional covariance matrix in analyzing the propagation properties of plane waves, *J. Geophys. Res.*, *92*, 7538, 1972.

[*Poulsen et al.*, 1993] Poulsen, W.L., Inan U.S. and T.F. Bell, A multiple-mode three-dimensional model of VLF propagation in the Earth-ionosphere waveguide in the presence of localized D region disturbances, *J. Geophys. Res.*, *98*, no. A2, 170

[*Sazhin*, 1991] Sazhin, S.S., Landau damping of low frequency whistler-mode waves, *Annales Geophysicae. Atmospheres, Hydrospheres and Space Sciences*, *9*, no. 10, 690–5, Oct 1991.

[*Schield and Frank*, 1970] Schield, M.A., and L. A. Frank, Electron Observations Between the Inner Edge of the Plasma Sheet and the Plasmasphere, *J. Geophys. Res.*, *75*, 5401, 1970.

[*Spjeldvik*, 1976] Spjeldvik, W.N., The equilibrium radiation belt electron pitch angle distribution and its dependence on the radial diffusive source, *J. of Geophys. Res.*, *81*, no. 16, 2931–4, Jun 1976.

[*Stix*, 1962] Stix, T. H., *The Theory of Plasma Waves*, McGraw-Hill, New York, 1962.

[*Thorne*, 1968] Thorne, R.M., Unducted whistler evidence for a secondary peak in the electron energy spectrum near 10 keV, *J. Geophys. Res.*, *73*, no. 15, 4895–904, Aug 1968.

[*Tkalcevic et al.*, 1984] Tkalcevic, S., Inan U.S. and R.A. Helliwell, Nonlinear pitch angle scattering and trapping of energetic particles during Landau resonance interactions with whistler mode waves, *J. Geophys. Res.*, *89*, no. A12, 10813–26, Dec 1984.

[*Uman*, 1984] Uman, M.A., *Lightning*, Dover Publications, Inc., New York, 1984.

[*Van Allen*, 1959] Van Allen, J.A., C.E. McIlwain and G.H. Ludwig, Radiation observations with Satellite 1958e, *J. Geophys. Res.*, *64*, 271, 1959.

[*Voss et al.*, 1984] Voss, H.D., Imhof W.L. Walt M. Mobilia J. Gaines E.E. Reagan J.B. Inan U.S. Helliwell R.A. Carpenter D.L. Katsufrakis J.P. and H.C. Chang, Lightning-induced electron precipitation, *Nature*, *312*, no. 5996, 740–2, Dec 1984.

[*Walt*, 1994] Walt, M., *Introduction to Geomagnetically Trapped Radiation*, Cambridge University Press, New York, 1994.

[*Walt et al.*, 1996] Walt, M., Inan U.S. and H.D. Voss, Trapped electron losses by interactions with coherent VLF waves, *AIP Conf. Proc.*, 65–70, 1996.

[*Walt*, 1997] Walt, M., Source and Loss Processes for Radiation Belt Particles, *Radiation Belts Models and Standards*, 1–13, 1997.

[*Yip et al.*, 1991] Yip, W.-Y., Inan U.S. and R.E. Orville, On the spatial relationship between lightning discharges and propagation paths of perturbed subionospheric VLF/LF signals, *J. Geophys. Res.*, *96*, no. A1, 249–58, Jan 1991.